

ETHANOL STEAM REFORMING WITH ZIRCONIA BASED CATALYSTS

A THESIS SUBMITTED TO
THE GRADUATE SCHOOL OF NATURAL AND APPLIED SCIENCES
OF
MIDDLE EAST TECHNICAL UNIVERSITY

BY

ARZU ARSLAN

IN PARTIAL FULFILLMENT OF THE REQUIREMENTS
FOR
THE DEGREE OF MASTER OF SCIENCE
IN
CHEMICAL ENGINEERING

AUGUST 2014

Approval of the thesis:

ETHANOL STEAM REFORMING WITH ZIRCONIA BASED CATALYSTS

submitted by **ARZU ARSLAN** in partial fulfillment of the requirements for the degree of **Master of Science in Chemical Engineering Department, Middle East Technical University** by,

Prof. Dr. Canan Özgen
Dean, Graduate School of **Natural and Applied Sciences**

Prof. Dr. Halil Kalıpçılar
Head of Department, **Chemical Engineering**

Prof. Dr. Timur Doğu
Supervisor, **Chemical Engineering Dept., METU**

Examining Committee Members:

Prof. Dr. Hayrettin Yücel
Chemical Engineering Dept., METU

Prof. Dr. Timur Doğu
Chemical Engineering Dept., METU

Prof. Dr. Tunçer H. Özdamar
Chemical Engineering Dept., Ankara University

Assoc. Prof. Dr. Meltem Doğan
Chemical Engineering Dept., Gazi University

Assoc. Prof. Dr. Nuray Oktar
Chemical Engineering Dept., Gazi University

Date: 27.08.2014

I hereby declare that all information in this document has been obtained and presented in accordance with academic rules and ethical conduct. I also declare that, as required by these rules and conduct, I have fully cited and referenced all material and results that are not original to this work.

Name, Last name: ARZU ARSLAN

Signature:

ABSTRACT

ETHANOL STEAM REFORMING WITH ZIRCONIA BASED CATALYSTS

Arslan, Arzu

M.S., Department of Chemical Engineering

Supervisor: Prof. Dr. Timur Doğu

August 2014, 144 pages

Production of hydrogen, which has been considered as an environmentally clean ideal energy carrier, from abundant energy resources cleanly and renewably is essential to support sustainable energy development. Hydrogen production from bio-ethanol by steam reforming process is a promising approach, since bio-ethanol is the most available bio-fuel in the world and steam reforming of ethanol yields formation of 6 moles of hydrogen per mole of ethanol. Support material used for nickel based catalysts plays a crucial role for determining the activity and the stability of the catalyst, in ethanol steam reforming reaction. The main objective of this study was to achieve high purity hydrogen production with minimum coke deposition by using zirconia-silicate and ceria-zirconia supported nickel catalysts.

Mesoporous zirconia and zirconia-silicate structured materials, such as Zr-SBA-15, Ce-Zr-SBA-15, Mg-Zr-SBA-15 and Zr-MCM-41, were synthesized following surfactant assisted synthesis routes and nickel was impregnated (6 wt.%) on these catalyst supports. Despite its highly acidic nature, Ni@ZrO₂ catalyst resulted in reasonably high hydrogen production and medium-level graphitic carbon deposition. Zirconia-silicate supported catalysts showed much higher ethanol steam reforming activity and carbon deposition due to their higher surface area (>300 m²/g). Ni@Zr-SBA-15 catalyst resulted in very high catalytic activity, with hydrogen yield values

approaching to 90% of the maximum possible yield of 6 and stability at 600 °C and 650 °C. Ce⁴⁺ or Mg²⁺ incorporated Zr-SBA-15 supported nickel catalyst suffered from high carbon deposition rates, especially at 600 °C, compared to Ni@Zr-SBA-15. Reduction of water adsorption-dissociation capability caused by magnesia and ceria limited the carbon gasification capability of zirconia in Zr-SBA-15 type material. In order to obtain maximum hydrogen yield with minimum coking, both acidity and ability of catalyst for dissociation of water to gasify the deposited carbon should be adjusted in ethanol steam reforming catalysts.

In order to achieve high purity hydrogen production with long term stability, reaction temperature of ethanol steam reforming process and catalyst properties requires optimization. Properties of mesoporous CeO₂-ZrO₂ catalysts such as calcination and reduction temperatures and CeO₂/ZrO₂ ratio of the catalyst were adjusted according to activity test results. Calcination, reduction and reaction temperatures were investigated in the range of 450-650 °C and ZrO₂/CeO₂ ratio was changed from 0 to 1/6. With CeO₂-ZrO₂ supported nickel catalyst having CeO₂/ZrO₂ ratio of 6, 450 °C was found to be the optimum for calcination, reduction and operating temperatures. Calcination at higher temperatures resulted in collapse of the mesoporous structure of the materials due to sintering. Activity tests at 450 °C revealed the importance of crystal size in ethanol steam reforming reaction. CeO₂-ZrO₂ supported nickel catalyst having CeO₂/ZrO₂ ratio of 6 calcined and reduced at 650 °C caused 34% graphitic carbon deposition with very low hydrogen production and only 2% coke deposition was occurred with the material calcined and reduced at 450 °C with a 5.15 hydrogen formation per mole of ethanol which corresponds to 86% of the maximum possible value of 6. Investigation of optimum CeO₂/ZrO₂ ratio lead to the selection of 4 due to its best catalytic activity with over 90% hydrogen production per mole of ethanol, despite the formation of 30% graphitic carbon.

Keywords: Ethanol steam reforming, zirconia-silicate structured catalysts, ceria-zirconia supported catalysts, coke minimization

ÖZ

ETANOLÜN ZİRKONYUM BAZLI KATALİZÖRLERLE BUHARLI REFORMLANMASI

Arslan, Arzu

Yüksek Lisans, Kimya Mühendisliği Bölümü

Tez Yöneticisi: Prof. Dr. Timur Doğu

Ağustos 2014, 144 sayfa

Çevresel olarak temiz ve ideal bir enerji taşıyıcısı olarak görülen hidrojen, yaygın olarak bulunan enerji kaynaklarından temiz ve yenilenebilir bir şekilde üretilmektedir. Ayrıca, sürdürülebilir enerji kalkınmasını desteklemesi açısından da bir gerekliliktir. Biyo-etanol, dünyada en yaygın olarak bulunan biyo-yakıtlardan bir tanesidir. Bu nedenle, hidrojenin biyo-etanolden buharlı reformlanma yoluyla üretilmesi umut vaat eden bir prosestir. Etanolün buharlı reformlanması bir mol etanolden altı mol hidrojen eldesine imkân verir. Nikel katalizörlerinde kullanılan destek malzemesi, etanolün buharlı reformlanmasında kullanılan katalizörün aktivitesi ve stabilitesini belirlemede çok önemli bir rol oynar. Bu çalışmanın ana amacı, zirkonyum-silika ve seryum-zirkonyum destekli nikel katalizörlerini kullanarak yüksek saflıkta hidrojen ve minimum kok oluşumu elde etmektir.

Mezogözenekli zirkonyum ve zirkonyum-silika malzemeleri; Zr-SBA-15, Ce-Zr-SBA-15, Mg-Zr-SBA-15 ve Zr-MCM-41, yüzey aktif maddeler yardımıyla sentezlenmiştir. Sentezlenen katalizör destek malzemelerinin üzerine ağırlıkça yaklaşık olarak %6 oranında nikel emdirilmiştir. Yüksek asitliğine rağmen, Ni@ZrO₂ katalizörü orta seviyede hidrojen üretimi ve grafit karbon oluşumu göstermiştir. Zirkonyum-silika yapısındaki katalizörler ise oldukça yüksek olan yüzey alanları (>300 m²/g) sayesinde etanolün buharlı reformlanma reaksiyonunda ve kok oluşumunda çok daha aktif oldukları gözlenmiştir. Ni@Zr-SBA-15 katalizörü oldukça

yüksek katalitik aktivite ve stabilite göstermiş, 600 °C ve 650 °C’lerde elde edilen hidrojen verimi, maksimum ulaşılabilecek değer olan 6’nın %90’ına ulaşmıştır. Zr-SBA-15 destek malzemesine Ce⁴⁺ veya Mg²⁺ eklendiğinde ise özellikle 600 °C’de kok oluşumu artmıştır. Magnezyum ve seryumun eklenmesi, Zr-SBA-15’in yapısındaki zirkonyumun suyu adsorblaması ve ayrıştırması prosesini azaltarak, zirkonyumun karbon gazlaştırma kabiliyetini sınırlandırmışlardır. Etanolün buharlı reformlanma reaksiyonunda minimum koklaşma ile maksimum hidrojen verimi elde edebilmek için katalizörün asitliğinin yanı sıra biriken kokun gazlaşabilmesi için suyu ayrıştırma kabiliyetinin de ayarlanması gerekmektedir.

Etanolün buharlı reformlanma reaksiyonunda yüksek saflıkta hidrojen üretimi ve uzun süreli stabilite elde edebilmek için, reaksiyonun sıcaklığı ve katalizörlerin özellikleri optimizasyon gerektirmektedir. Mezogözenekli CeO₂-ZrO₂ katalizörlerinin kalsinasyon ve indirgeme sıcaklıkları ve CeO₂/ZrO₂ oranları aktivite test sonuçlarına göre optimize edilmiştir. Kalsinasyon, indirgeme ve reaksiyon sıcaklıkları 450 °C ve 650 °C arasında değiştirilmiş, ZrO₂/CeO₂ oranı ise 0 ve 1/6 arasında olacak şekilde ayarlanmıştır. CeO₂/ZrO₂ oranı altı olan katalizör için 450 °C kalsinasyon, indirgeme ve reaksiyon sıcaklığı için ideal bulunmuştur. Yüksek sıcaklıklarda kalsine edilen malzemelerin sinterleşme nedeni ile yapısının bozulduğu gözlenmiştir. 450°C’de gerçekleştirilen aktivite testleri katalizördeki kristal boyutunun önemini ön plana çıkarmıştır. Kalsinasyonu ve indirgenmesi 650°C’de gerçekleştirilen ve CeO₂/ZrO₂ oranı 6 olan nikel katalizörü, 450 °C’de gerçekleştirilen aktivite testinde %34 oranında grafit karbon oluşumu ve oldukça düşük hidrojen verimi göstermiştir. Kalsinasyonu ve indirgenmesi 450 °C’de gerçekleştirilen katalizör ile aynı sıcaklıktaki test yalnızca %2 oranında amorf karbon oluşumuna neden olmuştur. Bunun yanı sıra, bu testte bir mol etanolden 5.15 mol hidrojen elde edilmiştir. Bu değer elde edilebilecek maksimum değer olan 6’nın %90’ına eşdeğerdir. Kalsinasyon, indirgeme ve reaksiyon sıcaklıkları 450°C’de sabit tutularak gerçekleştirilen katalizörlerin CeO₂/ZrO₂ oranı optimizasyonu deneyleri ise, bu oran 4 olduğunda, %30 oranında grafit karbon oluşumuna rağmen, %90’ın üzerinde verimle hidrojen üretilebileceğini göstermiştir.

Anahtar Kelimeler: Etanolün buharlı reformlanması, zirkonyum-silika yapıları katalizörler, seryum-zirkonyum yapıları katalizörler, kok minimizasyonu

To my family

ACKNOWLEDGEMENTS

First of all, I would like to express my deep gratitude to my supervisor Prof. Dr. Timur Dođu for his patient guidance, endless support and very useful critiques throughout this research work. Beginning from my undergraduate years, he inspired me with his extensive knowledge and constructive suggestions not only in every aspect of chemical engineering discipline, but also life. Without his influence and guidance, I could not find myself the way I discovered now.

I would like to offer my special thanks to my friend and lab-mate Seval Gündüz for her endless support. Working with her side by side every day and her valuable friendship taught me many valuable things. This study could not be completed without her help and motivation and I will always be always grateful to her.

I wish to thanks to my lab-mates and friends Burçin İkizer, Birce Pekmezci, Ayşegül Bayat and Gökhan Çelik for their friendship, suggestions and support. Without their friendship, these two years would not be so pleasant.

I would also like to extend my thanks to the technicians of the chemical engineering department Mihrican Açıkgöz and İsa Çağlar for their help and METU Central Laboratories for characterization studies.

I would like to present my sincere thanks to Barış Koray Bozdağ for his great support, endless patience, friendship and love. His encouragement and motivation helped me to finish this work.

I would like to thank specially to my family. I know that their limitless faith in me will always be with me. I wish to thank my mother Pakize Arslan for her endless support, patience and love. I wish to thank my father Mustafa Arslan and my brother Serdar Arslan for their continuous support and invaluable suggestions which will help me throughout my life.

Turkish Scientific and Technological Research Council (TUBITAK) grant (111M338), Middle East Technical University Research Fund (BAP-03-04-2014-003 and BAP-03-04-2013-001) and TUBA support are gratefully acknowledged.

TABLE OF CONTENTS

ABSTRACT	v
ÖZ	vii
ACKNOWLEDGEMENTS	x
TABLE OF CONTENTS	xi
LIST OF FIGURES	xv
LIST OF TABLES	xxii
NOMENCLATURE	xxiv
CHAPTERS	1
1. INTRODUCTION	1
1.1 DEPLETION OF ENERGY RESOURCES AND RELATED PROBLEMS	1
1.2 HYDROGEN ENERGY STRATEGIES.....	2
2. BIO-ETHANOL AS A FEEDSTOCK FOR HYDROGEN PRODUCTION.	9
2.1 PRODUCTION OF BIO-ETHANOL	9
2.2 HYDROGEN PRODUCTION ROUTES FROM BIO-ETHANOL.....	10
2.2.1 Steam Reforming of Ethanol.....	11
2.2.2 Partial Oxidation of Ethanol.....	11
2.2.3 Auto-thermal Reforming of Ethanol	12
3. STEAM REFORMING ETHANOL.....	13
3.1 STEAM REFORMING OF ETHANOL AND SIDE REACTIONS	13
3.2 THERMODYNAMICS OF STEAM REFORMING OF ETHANOL..	15
3.3 CATALYSTS USED IN STEAM REFORMING OF ETHANOL	22

3.3.1 Noble Metal Catalysts.....	23
3.3.2 Non-noble Metal Catalyst.....	24
3.4 COKE FORMATION ROUTES IN STEAM REFORMING OF ETHANOL	26
4. IDEAL CATALYSTS FOR STEAM REFORMING OF ETHANOL	29
4.1 MESOPOROUS MATERIALS	29
4.2 ZIRCONIA INCORPORATED MESOPOROUS MATERIALS	30
4.3 CeO ₂ /ZrO ₂ MATERIALS AS CATALYST SUPPORTS	33
4.4 OBJECTIVES	35
5. EXPERIMENTAL METHODS	37
5.1 CATALYST SYNTHESIS METHODS	37
5.1.1 Synthesis of ZrO ₂ catalyst support.....	37
5.1.2 Synthesis of Zr-SBA-15, Ce-Ze-SBA-15 and Mg-Zr-SBA-15 catalyst supports.....	38
5.1.3 Synthesis of Zr-MCM-41 catalyst support	39
5.1.4 Synthesis of CeO ₂ -ZrO ₂ Support Materials	40
5.1.5 Nickel Impregnation to the synthesized catalyst supports.....	42
5.2 CATALYST CHARACTERIZATION METHODS	44
5.2.1 X-Ray Diffraction Analysis	44
5.2.2 N ₂ Adsorption-Desorption Analysis	45
5.2.3 X-Ray Photoelectron Spectroscopy Analysis	46
5.2.4 Energy-Dispersive Spectroscopy Analysis	46
5.2.5 Diffuse Reflectance FTIR Spectroscopy of Pyridine Adsorption (DRIFTS) Analysis	46
5.2.6 Scanning Electron Microscopy (SEM) Analysis	47
5.2.7 Transmission Electron Microscopy (TEM) Analysis	47

5.2.8 Thermal Analysis (TGA).....	48
5.3 EXPERIMENTAL SET-UP OF THE ETHANOL STEAM REFORMING PROCESS.....	48
6. RESULTS AND DISCUSSION	51
6.1 CHARACTERIZATION RESULTS OF ZIRCONIA INCORPORATED MESOPOROUS CATALYSTS.....	51
6.2 CHARACTERIZATION RESULTS OF CeO ₂ /ZrO ₂ SUPPORTED CATALYSTS	60
6.3 ACTIVITY RESULTS OF ZIRCONIA INCORPORATED MESOPOROUS CATALYSTS IN ETHANOL STEAM REFORMING PROCESS	69
6.4. ACTIVITY RESULTS OF CeO ₂ /ZrO ₂ SUPPORTED CATALYSTS IN ETHANOL STEAM REFORMING PROCESS	79
6.5 CHARACTERIZATION RESULTS OF ZIRCONIA INCORPORATED MESOPOROUS CATALYSTS USED IN ACTIVITY TESTS	86
6.6 CHARACTERIZATION RESULTS OF CeO ₂ -ZrO ₂ SUPPORTED CATALYSTS USED IN ACTIVITY TESTS	96
6.7 SUMMARY OF ZIRCONIA INCORPORATED MESOPOROUS CATALYSTS	102
6.8 SUMMARY OF CeO ₂ -ZrO ₂ SUPPORTED CATALYSTS	104
7. CONCLUSION	109
REFERENCES	111
APPENDICES	119
A. SAMPLE PARTICLE SIZE CALCULATION.....	119
B. XRD DATA OF THE CATALYSTS	121
C. CALIBRATION OF GAS CHROMATOGRAPHY	127

D. SAMPLE CALCULATION FOR ETHANOL STEAM REFORMING	
ACTIVITY DATA	129
E. ACTIVITY TEST RESULTS	131

LIST OF FIGURES

FIGURES

Figure 1: Natural Hydrogen Sources	3
Figure 2: Hydrogen Utilization	6
Figure 3: Equilibrium H ₂ % in product stream calculated with Gaseq between 400°C and 750 °C with steam to ethanol ratio changing between 1 and 5.....	17
Figure 4: Equilibrium H ₂ yield calculated with Gaseq between 400°C and 750 °C with steam to ethanol ratio changing between 1 and 5.	17
Figure 5: Equilibrium carbon% in product stream calculated with Gaseq between 400°C and 750 °C with steam to ethanol ratio changing between 1 and 5.	18
Figure 6: Equilibrium product distributions calculated with Gaseq considering possible side product formation between 400°C and 750 °C with steam to ethanol ratio of 1.	19
Figure 7: Equilibrium product distributions calculated with Gaseq considering possible side product formation between 400°C and 750 °C with steam to ethanol ratio of 3.2.	19
Figure 8: Equilibrium product distributions calculated with Gaseq considering possible side product formation between 400°C and 750 °C with steam to ethanol ratio of 5.	20
Figure 9: Equilibrium product distributions calculated with Gaseq considering only ethanol steam reforming reaction products between 400°C and 750 °C with steam to ethanol ratio of 3.2.	21
Figure 10: Equilibrium H ₂ yield calculated with Gaseq considering only ethanol steam reforming reaction products between 400°C and 750 °C with steam to ethanol ratio of 3.2.....	22
Figure 11: Synthesis procedure of ZrO ₂ catalyst support.	38

Figure 12: Synthesis procedure of Zr-SBA-15, Ce-Zr-SBA-15 and Mg-Zr-SBA-15 catalyst support.....	39
Figure 13: Synthesis procedure of Zr-MCM-41 catalyst support.	40
Figure 14: Synthesis procedure of CeO ₂ -ZrO ₂ catalyst support.....	41
Figure 15: Schematical representation of experimental set-up	49
Figure 16: N ₂ adsorption/desorption isotherms of the zirconia incorporated catalyst supports.	53
Figure 17: Pore size distribution of the zirconia incorporated catalyst supports.	53
Figure 18: N ₂ adsorption/desorption isotherms of Ni impregnated zirconia based catalysts.	54
Figure 19: Pore size distribution of Ni impregnated zirconia based catalysts.	54
Figure 20: Low angle XRD pattern of ZrO ₂ and Ni@ZrO ₂	56
Figure 21: Wide angle XRD pattern of ZrO ₂ and Ni@ZrO ₂ (t represents tetragonal and m represents monoclinic zirconia phase)	56
Figure 22: Low angle XRD patterns of Ni@Zr-SBA-15, Ni@Mg-Zr-SBA-15, Ni@Ce-Zr-SBA-15 and Ni@Zr-MCM-41.....	58
Figure 23: Wide angle XRD patterns of Ni@Zr-SBA-15, Ni@Mg-Zr-SBA-15, Ni@Ce-Zr-SBA-15 and Ni@Zr-MCM-41.....	58
Figure 24: Pyridine adsorbed DRIFT spectra of Ni impregnated zirconia based catalysts.	59
Figure 25: N ₂ adsorption/desorption isotherms of Ni@CeO ₂ -ZrO ₂ (6:1) calcined and reduced at different temperatures.	62
Figure 26: Pore size distributions of Ni@CeO ₂ -ZrO ₂ (6:1) calcined and reduced at different temperatures.....	62
Figure 27: N ₂ adsorption/desorption isotherms of Ni@CeO ₂ -ZrO ₂ catalysts containing different CeO ₂ /ZrO ₂ ratios calcined and reduced at 450°C	63
Figure 28: N ₂ adsorption/desorption isotherms of Ni@CeO ₂ -ZrO ₂ catalysts containing different CeO ₂ /ZrO ₂ ratios calcined and reduced at 450°C.....	64
Figure 29: X-ray diffraction patterns of Ni@CeO ₂ -ZrO ₂ (6:1) calcined and reduced at different temperatures.....	65

Figure 30: X-ray diffraction patterns of Ni@CeO ₂ -ZrO ₂ catalysts containing different CeO ₂ /ZrO ₂ ratios calcined and reduced at 450°C.....	66
Figure 31: Ce (3d) XPS spectra for of Ni@CeO ₂ -ZrO ₂ (6:1) catalyst calcined and reduced at 450°C	67
Figure 32: Ni (2d) XPS spectra for of Ni@CeO ₂ -ZrO ₂ (6:1) catalyst calcined and reduced at 450°C	68
Figure 33: Zr (3d) XPS spectra for of Ni@CeO ₂ -ZrO ₂ (6:1) catalyst calcined and reduced at 450°C	69
Figure 34: Hydrogen yield observed at 550°C, 600°C and 650°C on Ni@Zr-SBA-15.	71
Figure 35: Product distribution of Ni@Zr-SBA-15 catalyst at 550°C.	72
Figure 36: Product distribution of Ni@Zr-SBA-15 catalyst at 600°C.	72
Figure 37: Product distribution of Ni@Zr-SBA-15 catalyst at 650°C.	73
Figure 38: Hydrogen yields of Ni@Zr-SBA-15, Ni@Ce-Zr-SBA-15, Ni@Mg-Zr-SBA-15, Ni@Zr-MCM-41 and Ni@ZrO ₂ catalysts at 600°C.	75
Figure 39: Product distribution of Ni@Ce-Zr-SBA-15 catalyst at 600°C.....	75
Figure 40: Product distribution of Ni@Mg-Zr-SBA-15 catalyst at 600°C.....	76
Figure 41: Product distribution of Ni@Zr-MCM-41 catalyst at 600°C.	76
Figure 42: Product distribution of Ni@ZrO ₂ catalyst at 600°C.....	77
Figure 43: Hydrogen yields of Ni@Zr-SBA-15 at 600°C.....	78
Figure 44: Hydrogen yields of Ni@Mg-Zr-SBA-15 at 600°C with.....	78
Figure 45: Comparison of hydrogen formation per mole of ethanol with Ni@CeO ₂ -ZrO ₂ (6:1) calcined and reduced at 650°C at different reaction temperatures for SRE.	81
Figure 46: Comparison of hydrogen formation per mole of ethanol with Ni@CeO ₂ -ZrO ₂ (6:1) calcined and reduced at 450°C and 650°C at a reaction temperature of 450°C for SRE.....	82
Figure 47: Product distribution at a reaction temperature of 450°C for SRE with Ni@CeO ₂ -ZrO ₂ (6:1) calcined and reduced at 450°C	83
Figure 48: Product distribution at a reaction temperature of 450°C for SRE with Ni@CeO ₂ -ZrO ₂ (6:1) calcined and reduced at 650°C	83

Figure 49: Comparison of hydrogen formation per mole of ethanol with Ni@CeO ₂ -ZrO ₂ catalyst containing different CeO ₂ /ZrO ₂ ratios calcined and reduced at 450°C at a reaction temperature of 450°C for SRE	85
Figure 50: Product distribution at a reaction temperature of 450°C for SRE with Ni@CeO ₂ -ZrO ₂ (4:1) catalyst calcined and reduced at 450°C.	85
Figure 51: Weight loss (%) of Ni@Zr-SBA-15 used at reaction temperatures of 550°C, 600°C, 650°C.....	87
Figure 52: Weight loss (%) of Ni@Zr-SBA-15, Ni@Ce-Zr-SBA-15, Ni@Mg-Zr-SBA-15, Ni@Zr-MCM-41 and Ni@ZrO ₂ catalysts used at a reaction temperature of 550°C.	88
Figure 53: Weight loss (%) of Ni@Zr-SBA-15, Ni@Ce-Zr-SBA-15, Ni@Mg-Zr-SBA-15, Ni@Zr-MCM-41 and Ni@ZrO ₂ catalysts used at a reaction temperature of 600°C.	88
Figure 54: Weight loss (%) of Ni@Zr-SBA-15 used at 600°C with H ₂ O/EtOH of 3.2, 4 and 5	89
Figure 55: Weight loss (%) of Ni@Mg-Zr-SBA-15 used at 600°C with H ₂ O/EtOH of 3.2, 4 and 5	89
Figure 56: Derivative TGA of Ni@Zr-SBA-15, Ni@Ce-Zr-SBA-15, Ni@Mg-Zr-SBA-15, Ni@Zr-MCM-41 and Ni@ZrO ₂ catalysts at 550°C.....	91
Figure 57: Derivative TGA of Ni@Zr-SBA-15, Ni@Ce-Zr-SBA-15, Ni@Mg-Zr-SBA-15, Ni@Zr-MCM-41 and Ni@ZrO ₂ catalysts at 600°C.....	91
Figure 58: TEM images of Ni@Zr-SBA-15 catalyst after reaction at 600°C with H ₂ O/EtOH=3.2 for 5 h.....	92
Figure 59: EDX metal mapping images of Ni@Zr-SBA-15 catalyst after reaction at 600°C with H ₂ O/EtOH=3.2 for 5 h.....	93
Figure 60: SEM images and carbon distributions of Ni@Zr-SBA-15 after reaction at 600°C with H ₂ O/EtOH=3.2 for 5 h (red points correspond to carbon on the surface).....	94
Figure 61: SEM images and carbon distributions of Ni@Mg-Zr-SBA-15 after reaction at 600°C with H ₂ O/EtOH=3.2 for 5 h (red points correspond to carbon on the surface)	95

Figure 62: Weight loss (%) of Ni@CeO ₂ -ZrO ₂ (6:1) catalyst calcined, reduced and exposed to reaction at 400°C, 450°C, 500°C, 550°C, 600°C and 650°C.	97
Figure 63: Differential weight loss of Ni@CeO ₂ -ZrO ₂ (6:1) catalyst calcined, reduced and exposed to reaction at 400°C, 450°C, 500°C, 550°C, 600°C and 650°C.....	98
Figure 64: Weight loss (%) after SRE at 450°C, 550°C, 600°C and 650°C of Ni@CeO ₂ -ZrO ₂ (6:1) catalyst calcined and reduced at 650°C.....	98
Figure 65: Differential weight loss after SRE at 450°C, 550°C, 600°C and 650°C of Ni@CeO ₂ -ZrO ₂ (6:1) catalyst calcined and reduced at 650°C.....	99
Figure 66. Weight loss (%) after SRE at 450°C of Ni@CeO ₂ -ZrO ₂ catalyst with different CeO ₂ /ZrO ₂ ratios.	100
Figure 67. Differential weight loss after SRE at 450°C of Ni@CeO ₂ -ZrO ₂ catalyst with different CeO ₂ /ZrO ₂ ratios.	101
Figure 68. X-ray diffraction patterns of used Ni@CeO ₂ -ZrO ₂ (4:1) calcined, reduced and used at 450°C, Ni@CeO ₂ -ZrO ₂ (6:1) calcined, reduced and used at 450°C, Ni@CeO ₂ -ZrO ₂ (6:1) calcined, reduced and used at 650°C.....	102
Figure 69: Product distribution of Ni@ZrO ₂ catalyst at 550°C.	131
Figure 70: Product distribution of Ni@Ce-Zr-SBA-15 catalyst at 550°C.	132
Figure 71: Product distribution of Ni@Mg-Zr-SBA-15 catalyst at 550°C with a H ₂ O/EtOH of 3.2.....	132
Figure 72: Product distribution of Ni@Mg-Zr-SBA-15 catalyst at 600°C with a H ₂ O/EtOH of 4.....	133
Figure 73: Product distribution of Ni@Mg-Zr-SBA-15 catalyst at 600°C with a H ₂ O/EtOH of 5.....	133
Figure 74: Product distribution of Ni@Zr-MCM-41 catalyst at 550°C.....	134
Figure 75: Product distribution of Ni@Zr-SBA-15 catalyst at 600°C with a H ₂ O/EtOH of 4.	134
Figure 76: Product distribution of Ni@Zr-SBA-15 catalyst at 600°C with a H ₂ O/EtOH of 5.	135
Figure 77: Product distribution at a reaction temperature of 650°C for SRE with Ni@CeO ₂ -ZrO ₂ (6:1) calcined and reduced at 650°C	135

Figure 78: Product distribution at a reaction temperature of 650°C for SRE with Ni@CeO ₂ -ZrO ₂ (6:1) calcined and reduced at 600°C.....	136
Figure 79: Ethanol conversion at a reaction temperature of 550°C for SRE with Ni@CeO ₂ -ZrO ₂ (6:1) calcined and reduced at 650°C.....	136
Figure 80: Product distribution at a reaction temperature of 550°C for SRE with Ni@CeO ₂ -ZrO ₂ (6:1) calcined and reduced at 650°C.....	137
Figure 81: Ethanol conversion at a reaction temperature of 450°C for SRE with Ni@CeO ₂ -ZrO ₂ (6:1) calcined and reduced at 650°C.....	137
Figure 82: Ethanol conversion at a reaction temperature of 400°C for SRE with Ni@CeO ₂ -ZrO ₂ (6:1) calcined and reduced at 400°C.....	138
Figure 83: Product distribution at a reaction temperature of 400°C for SRE with Ni@CeO ₂ -ZrO ₂ (6:1) calcined and reduced at 400°C.....	138
Figure 84: Ethanol conversion at a reaction temperature of 450°C for SRE with Ni@CeO ₂ -ZrO ₂ (6:1) calcined and reduced at 450°C.....	139
Figure 85: Ethanol conversion at a reaction temperature of 500°C for SRE with Ni@CeO ₂ -ZrO ₂ (6:1) calcined and reduced at 500°C.....	139
Figure 86: Product distribution at a reaction temperature of 500°C for SRE with Ni@CeO ₂ -ZrO ₂ (6:1) calcined and reduced at 500°C.....	140
Figure 87: Product distribution at a reaction temperature of 550°C for SRE with Ni@CeO ₂ -ZrO ₂ (6:1) calcined and reduced at 550°C.....	140
Figure 88: Product distribution at a reaction temperature of 550°C for SRE with Ni@CeO ₂ -ZrO ₂ (6:1) calcined and reduced at 550°C.....	141
Figure 89: Product distribution at a reaction temperature of 600°C for SRE with Ni@CeO ₂ -ZrO ₂ (6:1) calcined and reduced at 600°C.....	141
Figure 90: Product distribution at a reaction temperature of 450°C for SRE with Ni@CeO ₂ calcined and reduced at 450°C.	142
Figure 91: Ethanol conversion at a reaction temperature of 450°C for SRE with Ni@CeO ₂ -ZrO ₂ (1:1) calcined and reduced at 450°C.....	142
Figure 92: Product distribution at a reaction temperature of 450°C for SRE with Ni@CeO ₂ -ZrO ₂ (1:1) calcined and reduced at 450°C.....	143

Figure 93: Ethanol conversion at a reaction temperature of 450°C for SRE with Ni@CeO ₂ -ZrO ₂ (2:1) calcined and reduced at 450°C.	143
Figure 94: Product distribution at a reaction temperature of 450°C for SRE with Ni@CeO ₂ -ZrO ₂ (2:1) calcined and reduced at 450°C.	144

LIST OF TABLES

TABLES

Table 1: Energy contents and carbon emissions of hydrogen and other fuels	3
Table 2: Main reactions take place in the steam reforming of ethanol process	14
Table 3: Metal composition of CeO ₂ -ZrO ₂ catalyst supports.....	41
Table 4: Composition and Calcination & Reduction Temperatures of the Catalysts	43
Table 5: Physicochemical properties of zirconia incorporated supports.....	52
Table 6: Physicochemical properties of Ni impregnated zirconia based catalysts....	55
Table 7: Physicochemical properties of the CeO ₂ -ZrO ₂ support materials	60
Table 8: Physicochemical properties of the CeO ₂ -ZrO ₂ supported catalysts.....	61
Table 9: Activity data for ethanol steam reforming of zirconia incorporated catalysts at different temperatures and water-to-ethanol ratios. (Average of 5 h).....	70
Table 10: Activity results towards ethanol steam reforming of CeO ₂ -ZrO ₂ supported nickel catalysts	80
Table 11: Properties and activity results of zirconia incorporated mesoporous catalysts	103
Table 12: Summary of catalyst properties and activity test results of CeO ₂ -ZrO ₂ supported catalysts	105
Table 13: XRD data of Ni@ZrO ₂	119
Table 14: XRD data of Ni@Zr-SBA-15.....	121
Table 15: XRD data of Ni@Mg-Zr-SBA-15.....	121
Table 16: XRD data of Ni@Zr-MCM-41.....	121
Table 17: XRD data of Ni@Ce-Zr-SBA-15.....	122
Table 18: XRD data of Ni@CeO ₂ -ZrO ₂ (6:1) calcined and reduced at 400°C.....	122
Table 19: XRD data of Ni@CeO ₂ -ZrO ₂ (6:1) calcined and reduced at 450°C.....	122
Table 20: XRD data of Ni@CeO ₂ -ZrO ₂ (6:1) calcined and reduced at 500°C.....	122
Table 21: XRD data of Ni@CeO ₂ -ZrO ₂ (6:1) calcined and reduced at 600°C.....	123

Table 22: XRD data of Ni@CeO ₂ -ZrO ₂ (6:1) calcined and reduced at 650°C	123
Table 23: XRD data of Ni@CeO ₂ calcined and reduced at 450°C	123
Table 24: XRD data of Ni@CeO ₂ -ZrO ₂ (4:1) calcined and reduced at 450°C	124
Table 25: XRD data of Ni@CeO ₂ -ZrO ₂ (2:1) calcined and reduced at 450°C	124
Table 26: XRD data of Ni@CeO ₂ -ZrO ₂ (1:1) calcined and reduced at 450°C	124
Table 27: XRD data of used Ni@CeO ₂ -ZrO ₂ (4:1) calcined and reduced and exposed to reaction at 450°C	125
Table 28: XRD data of used Ni@CeO ₂ -ZrO ₂ (6:1) calcined and reduced and exposed to reaction at 450°C	125
Table 29: XRD data of used Ni@CeO ₂ -ZrO ₂ (6:1) calcined and reduced and exposed to reaction at 650°C	125
Table 30: Calibration parameters of gases involved in the SRE process.....	127
Table 31: Data of 40 th minute obtained with Ni@CeO ₂ /ZrO ₂ at 450°C.....	129

NOMENCLATURE

Calc: Calcined

D_p : Pore diameter

DRIFTS: Diffuse Reflectance Infrared Fourier Transform Spectroscopy

EtOH: Ethanol

IUPAC: International Union of Pure and Applied Chemistry

MCM: Mobil Composition of Matter

Red: Reduced

S_{BET} : BET surface area

SBA: Santa Barbara Acid

SEM: Scanning Electron Microscopy

SRE: Steam reforming of ethanol

SS: Solid solution

T: Temperature ($^{\circ}C$)

TEM: Transmission Electron Microscopy

V_p : Pore volume

X: Conversion

XRD: X-Ray Diffraction

CHAPTER 1

INTRODUCTION

1.1 DEPLETION OF ENERGY RESOURCES AND RELATED PROBLEMS

Energy related problems are growing in the world. Energy is not just a commodity; it is a factor that connects other commodities such as air, water and earth [1]. Quality of life of the society is directly related to the energy, since the use of low priced and clean fuel is connected to industrial and technological developments around the world [2]. Development of technology lead to change in the used energy sources from firewood, water mills, animal and slave work to hydroelectric energy, coal, oil, gas, nuclear energy, solar energy, wind energy and others. Every energy source has in greater or minor form of difficulties [3]. Today, greatest problems of energy systems are energy security, energy access and low carbon systemic energy transition. Depletion of primary energy resources due to increasing world population, developing technology and increased living standards is one of the main reasons of these problems. Primary energy means the natural energy resources such as coal, crude oil, natural gas and even sunlight, wind or falling water. Primary energy is converted to end-use energy which is then supplied to the consumer such as kerosene, gasoline or electricity [2, 4].

Energy security is defined as to provide attainable, affordable efficient and environmentally benign energy services to end-users. Energy access is related to the unjust energy distribution over the world. Billions of people have no access to electricity or use traditional fuels which are highly pollutant for household needs. Low carbon transition is related to quality, quantity and structure of energy production and use. Environmental outcomes of low quality energy usage known as greenhouse gas

emissions are widely known. To stabilize CO₂ emissions at sustainable levels; energy production, consumption and use should be controlled by enabling the use of available energy in a highly efficient way and alternative energy production and consumption should be improved [4].

The majority of energy used today comes from fossil fuel reserves which are limited and will not be available for much longer times. It is reported by energy experts that petroleum reserves have less than 40 years, natural gas has less than 60 years and coal has less than 250 years before these primary energy resources will be depleted [2]. It is possible to find other fossil fields by searching greater depths and higher extraction costs, but fossil fuels cannot be identified as the principal energy source and there is also increase in energy consumption in the world which can only be provided if alternative energy solutions are found [3]. Studies on alternative energy are increased recently due to these reasons for future world stability in both environmentally and economically [2]. Renewable energy alternatives, such as solar, wind and biomass are seen to be very promising, but produced energy is not stable and cannot be stored. Hydrogen has been considered as an ideal energy carrier that will reduce the dependence on fossil fuels. Hydrogen powered fuel cell vehicles are expected to be harmless to the environment and efficient, but use of fuel cells can only be environmentally friendly as long as hydrogen is produced cleanly from non-fossil resources. Thus, production of hydrogen from abundant energy resources cleanly and renewably is essential to support sustainable energy development [5].

1.2 HYDROGEN ENERGY STRATEGIES

Hydrogen is seen as the future energy carrier due to its primary effect on reducing global environmental effects of fossil fuels. Besides reducing carbon footprint, energy of hydrogen per unit mass is much higher than fossil fuels used currently and other fuel alternatives (Table 1). However, it does not exist in free state in nature due to its high reactivity. Hydrogen is abundantly available in natural sources such as in hydrocarbons, water and biomass (Figure 1). It comes from Greek words

“hydro” and “genes” meaning “water” and “generator”. Hydrogen is the first element in the periodic table; it is very simple and found in universe plentifully being the key part of water [2].

Table 1: Energy contents and carbon emissions of hydrogen and other fuels [2].

Fuel Type	Energy per unit mass (J/kg)	Energy per unit volume (J/m³)	Specific carbon emission (kg C/kg fuel)
Liquid Hydrogen	141.90	10.10	0.00
Gaseous Hydrogen	141.90	0.013	0.00
Fuel Oil	45.50	38.65	0.84
Gasoline	47.40	34.85	0.86
Jet Fuel	46.50	35.30	-
LPG	48.80	24.40	-
Methanol	22.30	18.10	0.50
Ethanol	29.90	23.60	0.50
Bio diesel	37.00	33.00	0.50
Natural Gas	50.00	0.04	0.46
Charcoal	30.00	-	0.50

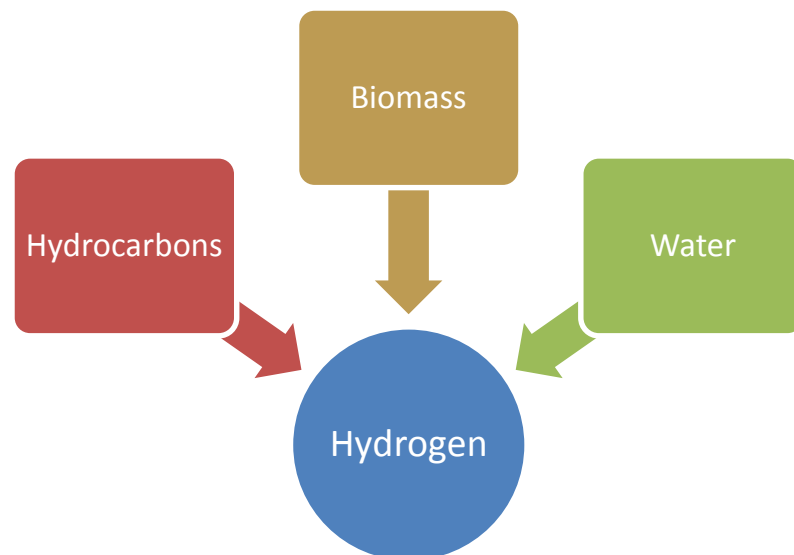


Figure 1: Natural Hydrogen Sources

Important advantages of hydrogen are [2];

- Hydrogen is a non-toxic, clean energy carrier and possesses high specific energy.
- Combustion of hydrogen with air produces energy and only pure water as the reaction product.
- Hydrogen can be produced from fossil fuels and renewable sources using different production processes such as steam reforming of natural gas or other light hydrocarbons like ethanol, gasification of coal and other heavy hydrocarbons or electrolysis of water.
- Produced energy can be easily distributed according to the needs of end users in accordance with the developing technology.
- It is possible to produce valuable hydrocarbons using hydrogen as feedstock.
- During combustion of hydrogen, non-toxic exhaust emissions occur except at its flame temperature where significant NO_x levels are reached.
- Storage period of hydrogen is longer compared to electricity and it can be used to generate electricity using fuel cells or directly used as automobile fuel.

Despite these important advantageous, there are multiple disadvantages of hydrogen [2];

- There are safety issues related to mostly hydrogen being burned in even lower concentrations when it is mixed with air.
- Storage of hydrogen is very problematic in both liquid and gaseous forms. To store hydrogen in liquid form, very low temperatures are necessary requiring high energy and since hydrogen is a very small element, it could escape through the storage in gas form.

Despite the fact that hydrogen is very promising as an energy carrier considering environmental quality, development of optimum technologies for

hydrogen production, transportation, storage and usage are necessary. Hydrogen has begun to be used in fuel cell powered vehicles in which hydrogen is stored at high pressures, in many parts of the world and improvement of the fuel cell technology from the point of view of hydrogen economy will enhance the usage of hydrogen-powered vehicles [6, 7].

In order to increase of usage of hydrogen, several suggestions are made. To use hydrogen as transportation fuel, it is proposed to mix hydrogen with natural gas for internal combustion engines increasing the engine performance and reducing the pollution caused by natural gas. Another proposition is to produce hydrogen in a central facility and distribute it to refueling stations where hydrogen can be pumped to vehicles to be used in fuel cells. Beside fuel cells, hydrogen can be used in many applications which are summarized in Figure 2 [2]. Power generation applications include fuel cells, gas turbines and hydrogen plants. Domestic applications refer to heating, cooling and cooking devices. Industrial applications includes all the industries that uses hydrogen such as methanol and ammonia synthesis, fertilizer production, oil distillation, petrochemical industry, nickel and iron production and many others. Vehicle operations includes fuel cells, IC engines, combustion included applications and defense industry. Navigation applications are related to hydrogen in power generation, ship engines, communication purposes, pollution control and energy storage areas. Lastly, aeronautics applications include gas turbines, jet engines, defense industry, rockets and space industry.



Figure 2: Hydrogen Utilization [2]

It is expected in short term that hydrogen will be produced by steam reforming of natural gas which is the most economic method. Unfortunately, natural gas usage does not solve the world's one of the major problem of carbon dioxide emissions. In the intermediate term, hydrogen powered fuel cells are expected to be used for in situ generation of electricity, thermal energy for hot water, space heating and industrial processes. In the long term, fuel cells will produce electricity for higher demand, hydrogen will be produced from water and sunlight and storage and transportation of hydrogen will be possible with the advanced technologies [2]. In spite of the fact that hydrogen is seen as the future of energy, there are some economic and environmental concerns regarding production techniques and feedstock used in the production. Use of fossil fuels are accepted as economically viable with current technology and

methods such as steam reforming of natural gas, coal gasification and partial oxidation of hydrocarbons are among the most suitable hydrogen production methods. Catalytic steam reforming uses only light hydrocarbons and contains three stages; generation of synthesis gas, shift reaction reforming and gas purification. Desulfurization process is required for steam reforming of hydrocarbons in order to prevent catalyst poisoning. Coal gasification is a high temperature endothermic process and uses pulverized coal, pure oxygen and steam. Partial oxidation of hydrocarbons can be used when reforming of natural gas is not economically feasible, since the process requires pure oxygen and result in low efficiency compared to reforming of natural gas [7]. Hydrogen production methods based on fossil fuels have a huge impact on environmental pollution and fossil fuel usage for the production of secondary energy is not sustainable [5].

Apart from the environmental point of view, hydrogen production from renewable sources has also attracted interest from the technological point of view due to the developed methods such as thermochemical processes from biomass, thermal decomposition of water, photo-electrochemical conversion and water electrolysis. Hydrogen production using water as the source has accomplished, but when the hydrogen economy with the current technology is concerned, application of these processes is not feasible yet. Biodegradable fraction of product such as waste, agriculture residues, forestry residues and industrial and city garbage are called biomass and hydrogen can be produced from these materials via gasification and pyrolysis processes [7]. Instead of using biomass for hydrogen production directly, converting biomass to bio-ethanol is a promising approach for in-situ hydrogen production.

CHAPTER 2

BIO-ETHANOL AS A FEEDSTOCK FOR HYDROGEN PRODUCTION

Hydrogen production from bio-ethanol has been considered as a promising opportunity; since bio-ethanol is the most available bio-fuel in the world. Ethanol possess many advantages for in-situ hydrogen production to be supplied to fuel cells for generation of electricity. Some these advantages are;

- Ethanol possesses very high hydrogen content (103 g H₂/ liter of ethanol)
- Storage and transportation of ethanol is safe
- It can be produced from cellulosic biomass which is abundant in nature by fermentation
- Produced ethanol contains significant amount of water which can be directly used in steam reforming reaction
- It possess no sulfur derivatives that would be poisonous to the catalyst
- Using bio-ethanol for hydrogen production completes the carbon balance since carbon dioxide produced from the production of hydrogen is reabsorbed during the growth of biomass [8].

2.1 PRODUCTION OF BIO-ETHANOL

Bio-ethanol is the product of anaerobic respiration (R.1) done by yeasts converting glucose into ethanol and carbon dioxide and generally called biomass fermentation [5].



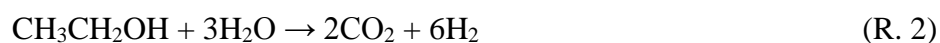
Bio-ethanol can be produced by fermentation of biomass sources, like energy plants, agroindustrial wastes, forestry residue materials and organic fraction of municipal solid waste. While using starch-rich materials such as sugar cane, switch grass, corns as feedstock is efficient, it is not preferred due to high cost of feedstock plantation. Production of ethanol using lignocellulosic biomass as the feedstock has many advantages such as lower production price and abundance of lignocellulosic biomass which corresponds to 50% of the biomass in the world. However, due to its more complex molecular structure, process is more challenging compared to process using starch-rich materials as feedstock. Fermentation of lignocellulosic biomass starts with hydrolysis of cellulose and hemicellulose to monomeric sugars and continues with the fermentation step in which bio-ethanol is obtained. In the fermentation step enzymes, concentrated and dilute acids are used that makes this process different from other fermentation processes. Despite its low efficiency, this process is expected to be more efficient and cost effective with the developing technology [5].

2.2 HYDROGEN PRODUCTION ROUTES FROM BIO-ETHANOL

Bio-ethanol is preferred to be used for hydrogen production instead of a fuel directly in internal combustion engines. The reason is the costly separation processes required for separating water from ethanol produced from biomass which contains 13 mol of water per mol of ethanol [8]. Hydrogen can be produced from ethanol generally by three different routes which are steam reforming, partial oxidation and oxidative steam reforming.

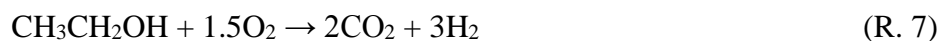
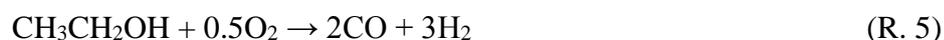
2.2.1 Steam Reforming of Ethanol

Steam reforming of ethanol is an endothermic process as shown by (R.3). When combined with water gas shift reaction (R.4), 6 mol of hydrogen can be obtained from one mol of ethanol via the ideal pathway which is overall steam reforming of ethanol (R.2). Hydrogen production rate can be changed significantly by adjusting steam supply and operating temperature. Major disadvantage of this process is coke formation.



2.2.2 Partial Oxidation of Ethanol

Partial oxidation reaction (R. 5, R. 6, R. 7) is incomplete oxidation of ethanol and it is an exothermic reaction producing carbon monoxide, carbon dioxide and hydrogen. Formation of carbon monoxide needs to be avoided since it is an inefficient by-product. For this reason water gas shift reactor is used after partial oxidation reactor to convert carbon monoxide to carbon dioxide [9].



Pure ethanol is used for partial oxidation. Pure feed has a higher energy content and partial oxidation process requires lower energy input since evaporation of water is not necessary. However, air is used as oxygen feed and nitrogen should be separated at the output for fuel cell applications bringing an additional separation cost. Maximum

theoretical hydrogen yield that can be obtained from partial oxidation of ethanol is 3 [9].

2.2.3 Auto-thermal Reforming of Ethanol

Auto-thermal reforming is the combination of steam reforming and partials oxidation reactions and aims to achieve minimum energy input. Moreover, using oxygen in steam reforming environment reduce coke formation which is the major problem with steam reforming of ethanol. Auto-thermal reforming also decreases carbon monoxide amount simplifying gas processing in water gas shift reactors. However, problem of separating nitrogen from the product gas in partial oxidation process remains in this process, as well [9].

From these three processes that can be used for hydrogen production from ethanol, steam reforming of ethanol was selected due to its lower total energy demand compared to partial oxidation and auto-thermal reforming processes reported by Rabenstein and Hacker [9] and higher hydrogen yield possibility. Ethanol steam reforming is discussed in detail in Chapter 3.

CHAPTER 3

STEAM REFORMING OF ETHANOL

Operating conditions of steam reforming of ethanol does not only favor R.2, there are also other reactions which could reduce the hydrogen production, depending on the temperature, supplied steam amount and catalyst properties. Thermodynamics of this process and reaction pathways are studied extensively and findings are given in this chapter.

3.1 STEAM REFORMING OF ETHANOL AND SIDE REACTIONS

Ideal reaction pathway for maximum hydrogen production is overall steam reforming reaction (R. 2), as mentioned before. For this reaction to dominate, sufficient steam should be supplied and side reaction occurrence should be minimized. If steam supply is insufficient or reaction environment is not suitable for water gas shift reaction (R.4), only ethanol steam reforming reaction (R. 3) takes place instead of overall reaction, reducing the maximum allowable hydrogen yield from 6 to 4. Besides water gas shift reaction, insufficient steam could also lead to the occurrence of R. 21 which was illustrated in Table 2. Occurrence of R.21, R.22, R. 23 and R.24 decreases the hydrogen productivity by using hydrogen as reactant and forming methane which is the main side product of this process. Methane could also form mainly from ethanol cracking reaction (R. 10, R. 11). Acetaldehyde and ethylene are accepted to be important intermediates formed through ethanol dehydrogenation (R. 8) and ethanol dehydration (R. 9) reactions, respectively. Decomposition of acetaldehyde (R. 12 and R. 13) and ethylene (R. 14) leads to formation of main undesired side products;

methane, carbon and carbon monoxide. Other than ethylene decomposition (R. 14), carbon depositions also occurs via Boudouard reaction (R. 16) and methane decomposition reaction (R. 15) [5], [10], [11].

Table 2: Main reactions take place in the steam reforming of ethanol process [5, 11]

Decomposition reactions			
Ethanol	$\text{CH}_3\text{CH}_2\text{OH} \rightarrow \text{C}_2\text{H}_4\text{O} + \text{H}_2$	Dehydrogenation	(R. 8)
	$\text{CH}_3\text{CH}_2\text{OH} \rightarrow \text{C}_2\text{H}_4 + \text{H}_2\text{O}$	Dehydration	(R. 9)
	$\text{CH}_3\text{CH}_2\text{OH} \rightarrow \text{CO} + \text{CH}_4 + \text{H}_2$	Cracking	(R. 10)
	$2\text{CH}_3\text{CH}_2\text{OH} \rightarrow 3\text{CH}_4 + \text{CO}_2$	Cracking	(R. 11)
Acetaldehyde	$2 \text{C}_2\text{H}_4\text{O} \rightarrow \text{C}_3\text{H}_6\text{O} + \text{CO} + \text{H}_2$	Acetone formation	(R. 12)
Acetaldehyde	$\text{C}_2\text{H}_4\text{O} \rightarrow \text{CH}_4 + \text{CO}$	Decarbonilation	(R. 13)
Ethylene	$\text{C}_2\text{H}_4 \rightarrow 2\text{C} + 2\text{H}_2$	Ethylene polymerization	(R. 14)
Methane	$\text{CH}_4 \rightarrow 2\text{H}_2 + \text{C}$	Methane decomposition	(R. 15)
Carbon monoxide	$2\text{CO} \rightarrow \text{CO}_2 + \text{C}$	Boudouard reaction	(R. 16)
Steam Reforming Reactions			
Ethanol	$\text{CH}_3\text{CH}_2\text{OH} + \text{H}_2\text{O} \rightarrow 2\text{CO} + 4\text{H}_2$		(R. 3)
Acetaldehyde	$\text{C}_2\text{H}_4\text{O} + \text{H}_2\text{O} \rightarrow 3\text{H}_2 + 2\text{CO}$		(R. 17)
Ethylene	$\text{C}_2\text{H}_4 + 2\text{H}_2\text{O} \rightarrow 4\text{H}_2 + 2\text{CO}$		(R. 18)
Methane	$\text{CH}_4 + \text{H}_2\text{O} \rightarrow 3\text{H}_2 + \text{CO}$		(R. 19)
Carbon monoxide	$\text{CO} + \text{H}_2\text{O} \rightarrow \text{H}_2 + 2\text{CO}_2$	Water gas shift	(R. 4)
Carbon	$\text{C} + \text{H}_2\text{O} \rightarrow \text{H}_2 + \text{CO}$	Carbon gasification	(R. 20)
Reactions using Hydrogen			
Ethanol	$\text{CH}_3\text{CH}_2\text{OH} + 2\text{H}_2 \rightarrow 2\text{CH}_4 + \text{H}_2\text{O}$		(R. 21)
Carbon monoxide	$\text{CO} + 3\text{H}_2 \rightarrow \text{CH}_4 + \text{H}_2\text{O}$	Methanation	(R. 22)
Carbon monoxide	$2\text{CO} + 2\text{H}_2 \rightarrow \text{CH}_4 + \text{CO}_2$	Reverse dry reforming	(R. 23)
Carbon dioxide	$\text{CO}_2 + 4\text{H}_2 \rightarrow \text{CH}_4 + 2\text{H}_2\text{O}$	Methanation	(R. 24)

3.2 THERMODYNAMICS OF STEAM REFORMING OF ETHANOL

Ethanol steam reforming is a thermodynamically limited reaction. In order to reach highest hydrogen yield, operating temperature and supplied steam amount should be carefully selected. While high temperatures and steam to ethanol ratios favor the production of hydrogen, they also require high energy input. An optimization between the cost of hydrogen production and efficiency of ethanol steam reforming reaction must be found. Thermodynamic equilibrium analysis provide insight for selection of these conditions before considering the catalyst properties and their effect on product distribution.

According to the analysis done by Fishtik et al. [12], ethanol is unstable compared to H_2 , CH_4 , H_2O , CO and CO_2 mixture and while low steam supply results in predominance of ethanol cracking reactions (R. 10 and R. 11), higher supply of steam lead to dominance of overall ethanol steam reforming reaction (R. 2). Methane formation also decreased at higher steam supply due to occurrence of methane steam reforming reaction at high temperatures. It was found that at low temperatures R. 11 is dominant and at high temperature R. 10 is favored. Alvarado et al. [13] reported that when steam to ethanol ratio is below 4, carbon deposits form and operating temperature defines the type of the carbon formed. Graphite was observed below $400^\circ C$ and multi wall carbon nanotube was observed above $400^\circ C$. According to Lima da Silva et al. [14], ethanol steam reforming produce ethylene and acetaldehyde at very low contact times resulting in coke deposition regardless of the temperature and steam supplied and they are known as carbon promoters. At moderate to high contact times, acetaldehyde and ethylene are converted to CH_4 , CO and CO_2 and high temperatures and steam to ethanol ratios favor hydrogen production. It is stated that besides high steam to ethanol ratios, high contact times are also beneficial for carbon activity. They concluded that above $550^\circ C$ and inlet steam to ethanol ratio of 3, carbon deposition can be avoided.

Thermodynamic equilibrium analysis was performed in the present work, in order to specify the operating conditions that will be used. A well-known equilibrium model: GasEq model which is based on the minimization of the free energy, developed

by Chris Morley was used in these analysis similar to the analysis performed by Kayadelen and Ust [15]. Gibbs energy minimization method was also used for equilibrium calculations by many researchers such as Lima De Silva et al. [14]. This method benefits from the fact that the ratio of Gibbs free energy to multiplication of gas constant to temperature being minimum at equilibrium conditions. Calculations are made considering the formation of H_2 , CO , CO_2 , CH_4 , C_2H_4 , C_2H_4O and $C_{(g)}$ by changing temperature and steam to ethanol ratio of the feed (H_2O and C_2H_5OH). Consideration of these products allows us to analyze the occurrence of all reactions given in Table 2. Obtained results were in agreement to the previous studies reported in the literature [8, 12]. It is found that, ethanol conversion was complete at all cases and increase in both temperature and steam to ethanol ratio of the feed enhances hydrogen production and hydrogen yield, as shown in Figure 3 and Figure 4, respectively. Selecting higher steam to ethanol ratios could be reasonable considering the difference between the hydrogen productions, but as the temperature increases after stoichiometric steam to ethanol ratio which is 3, supplied steam amount does not have a significant effect on the hydrogen production.

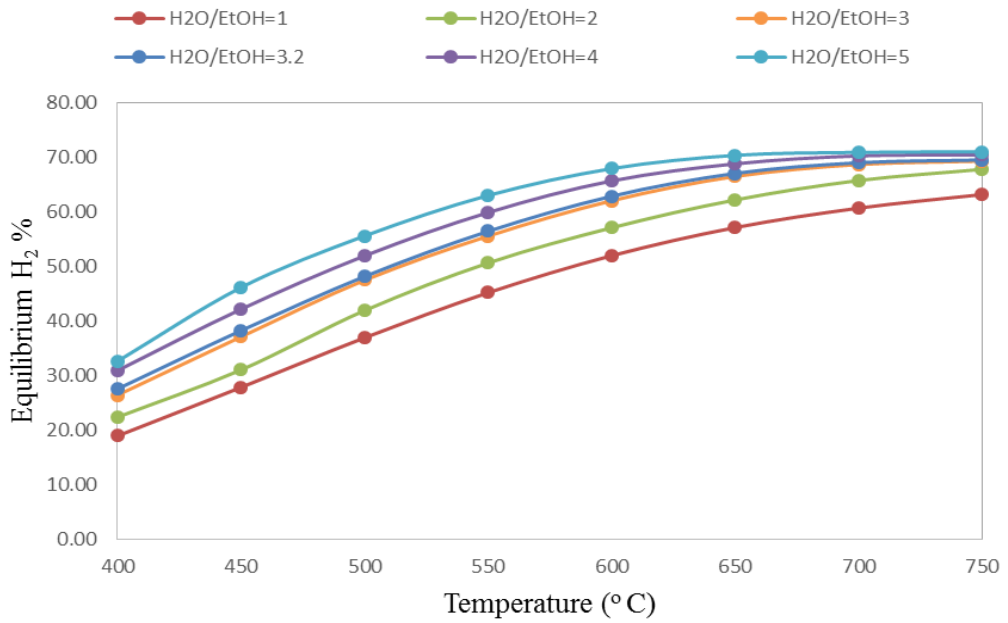


Figure 3: Equilibrium H₂% in product stream calculated with Gaseq between 400°C and 750 °C with steam to ethanol ratio changing between 1 and 5.

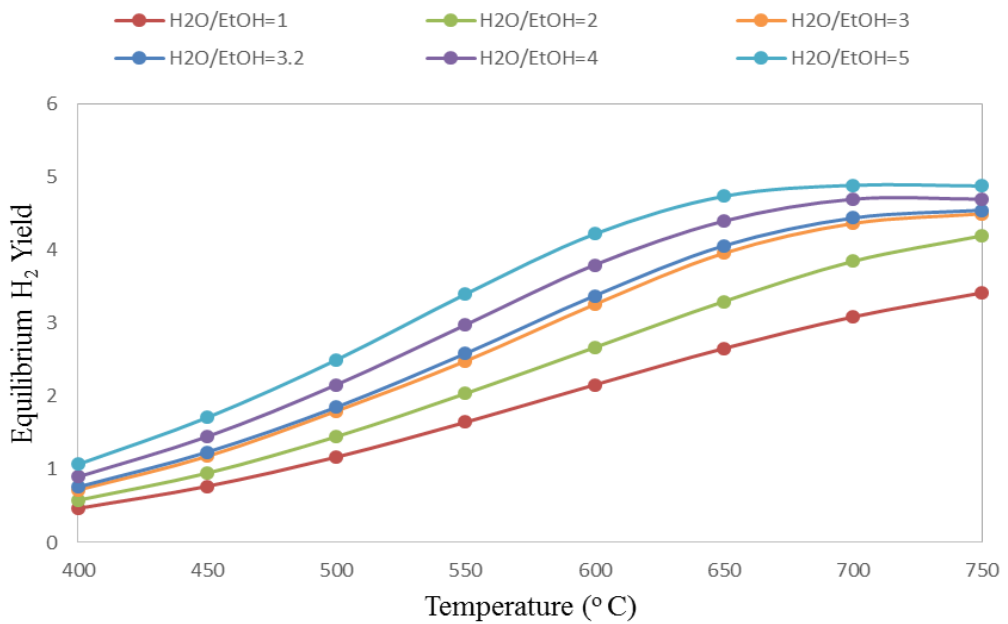


Figure 4: Equilibrium H₂ yield calculated with Gaseq between 400°C and 750 °C with steam to ethanol ratio changing between 1 and 5.

When equilibrium carbon formation was analyzed according to the change in both temperature and steam to ethanol ratio, it was observed that at low steam to ethanol ratios (1 and 2) carbon formation was very high and decreased with increasing temperature (Figure 5). Increase of steam to ethanol ratio above 3 completely inactivated carbon formation.

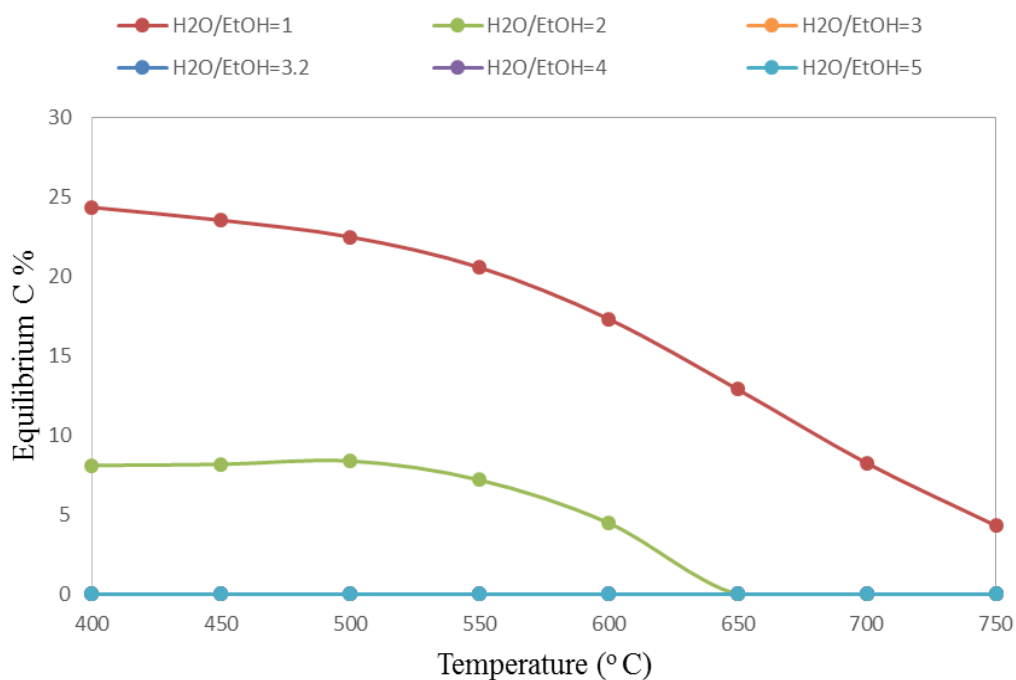


Figure 5: Equilibrium carbon% in product stream calculated with Gaseq between 400°C and 750 °C with steam to ethanol ratio changing between 1 and 5.

Effect on temperature and steam to ethanol ratio on other main and side products can be clearly seen in Figure 6, Figure 7 and Figure 8, respectively. Increase of temperature lead to decrease in thermodynamics of methane formation due to diminished ethanol cracking and reverse dry reforming and enhanced steam reforming. Water gas shift reaction also decreases with increasing temperature leading to increase in carbon monoxide and decrease in carbon dioxide formations, as expected. Acetaldehyde and ethylene were observed in trace amounts during equilibrium calculations at all temperatures and steam to ethanol ratios. Increase in steam to ethanol

ratio result in enhanced water gas shift reaction as well as steam reforming reactions leading to higher carbon dioxide and lower carbon monoxide formation.

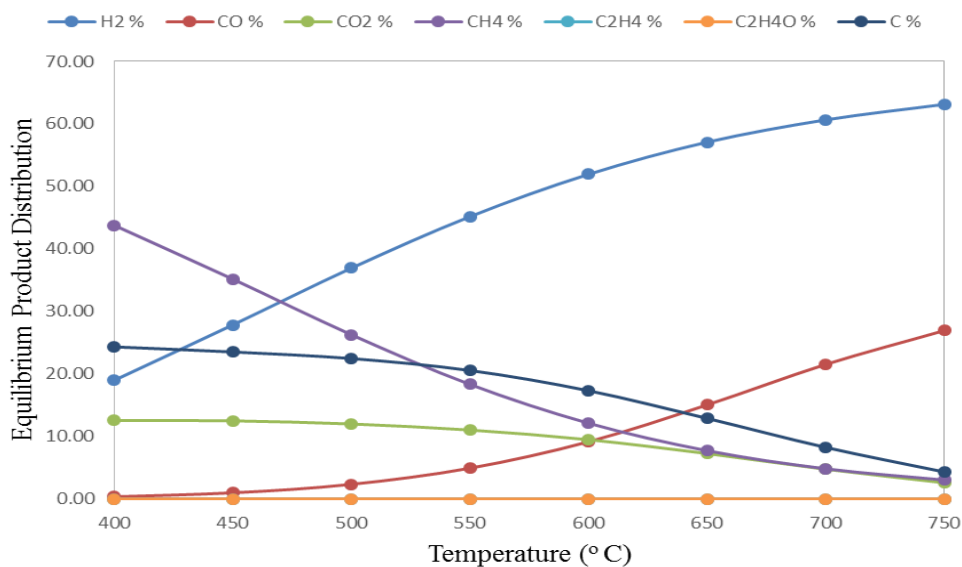


Figure 6: Equilibrium product distributions calculated with Gaseq considering possible side product formation between 400°C and 750 °C with steam to ethanol ratio of 1.

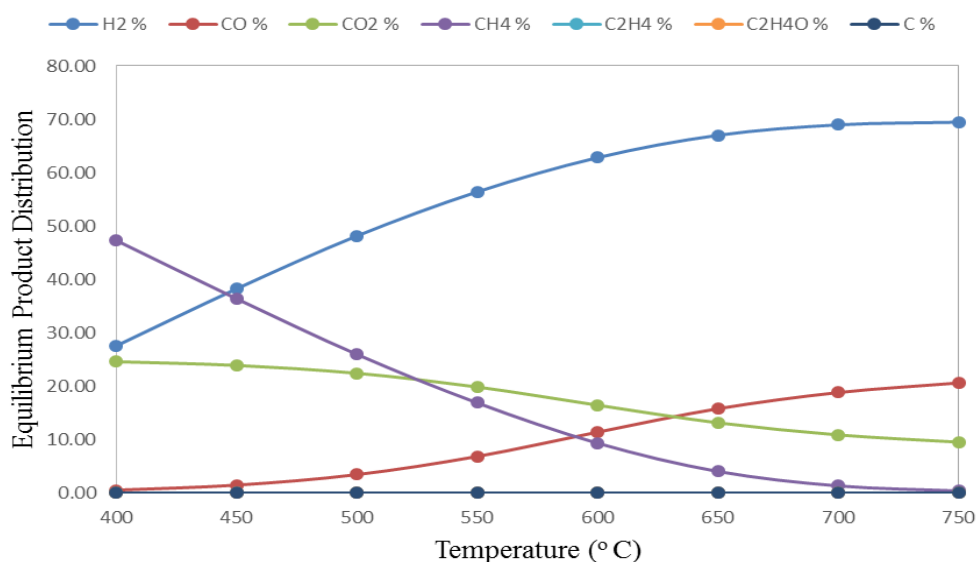


Figure 7: Equilibrium product distributions calculated with Gaseq considering possible side product formation between 400°C and 750 °C with steam to ethanol ratio of 3.2.

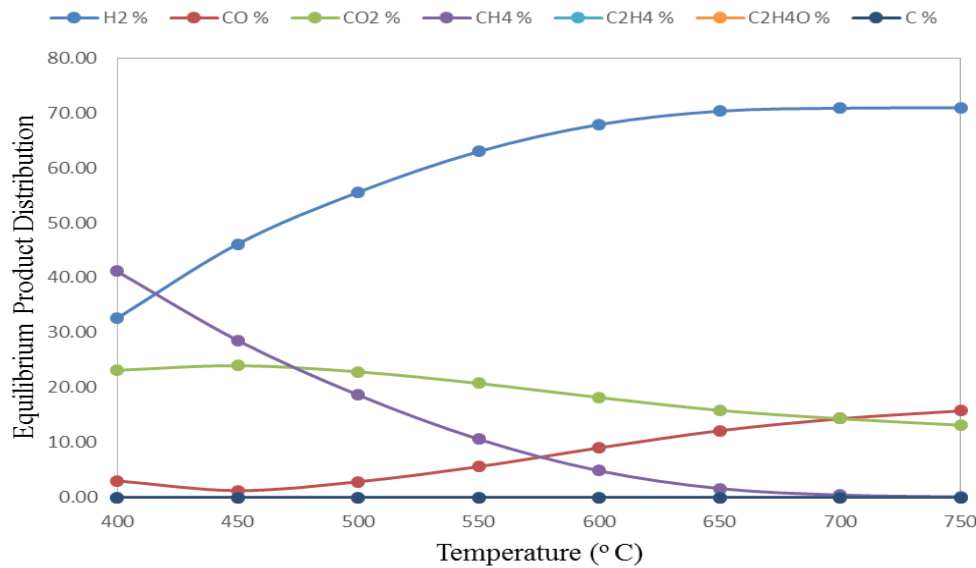


Figure 8: Equilibrium product distributions calculated with Gaseq considering possible side product formation between 400°C and 750 °C with steam to ethanol ratio of 5.

Use of Gibbs energy minimization method is useful to understand the effect of steam to ethanol ratio and temperature on the product distribution in ethanol steam reforming process. However experimental mol fractions that were reported in many studies were found to be higher than the equilibrium mol fractions calculated using energy minimization method. The reason was explained as the instability of the oxygenates with respect to the mixture of H₂O, H₂, CH₄, CO and CO₂ by Fishtik et al. [12]. Global equilibrium was found to be unrealistic in small packed-bed reactors with high flow rates and formation of CH₄ may be also prevented by catalysts causing occurrence of local minima case rather than global minimum. In the case of local minima, results would be quite different. For this reason, CH₄ was excluded from the calculations and equilibrium hydrogen presence, which are more realistic, was presented. When only steam reforming and water gas shift reactions were considered, (Figure 9), it was seen that equilibrium mole fraction of hydrogen is above 70% at all temperatures. Increase of temperature reduces hydrogen and carbon dioxide production slightly while increasing carbon monoxide formation due to diminished

water gas shift reaction activity at high temperatures. Equilibrium H₂ yield change according to temperature in these conditions was also given in Figure 10. It can be seen that increase of temperature from 400°C to 750°C decreases H₂ yield from 5.3 to 4.6 due to decrease in thermodynamics of water gas shift reaction (R. 4). Since it is an exothermic reaction, low temperatures are better for this reaction to be more active.

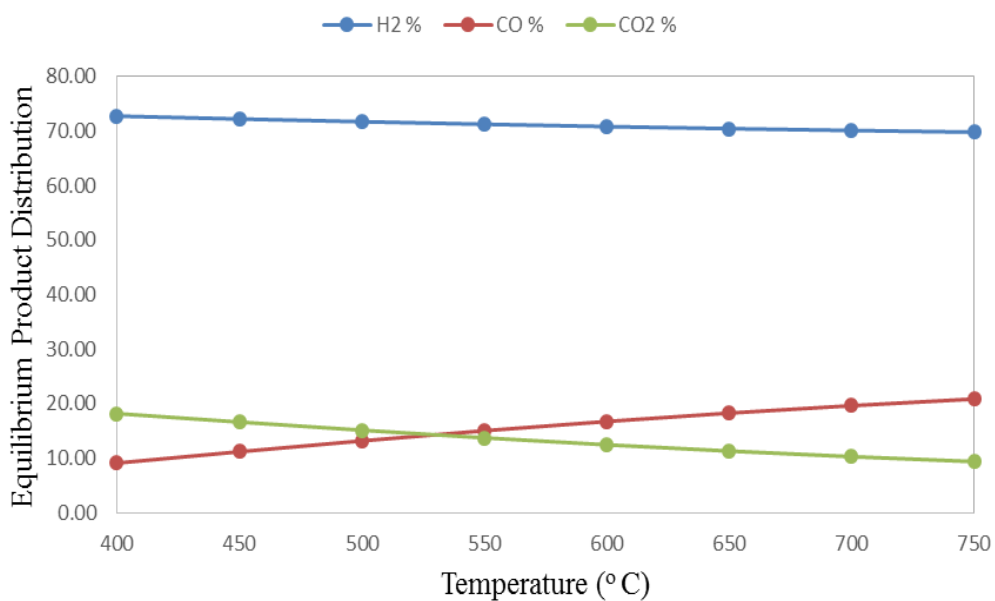


Figure 9: Equilibrium product distributions calculated with Gaseq considering only ethanol steam reforming reaction products between 400°C and 750 °C with steam to ethanol ratio of 3.2.

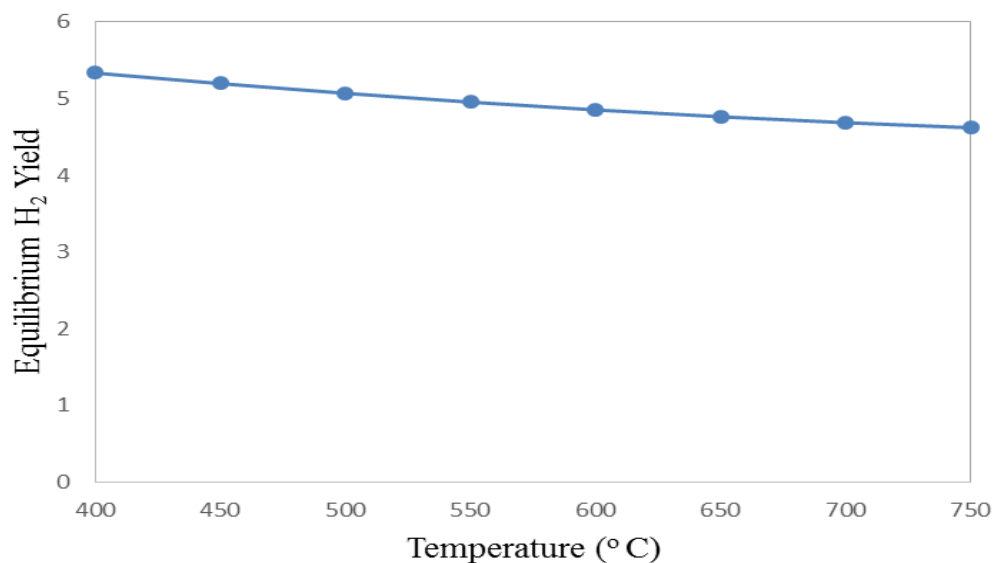


Figure 10: Equilibrium H₂ yield calculated with Gaseq considering only ethanol steam reforming reaction products between 400°C and 750 °C with steam to ethanol ratio of 3.2.

Steam to ethanol ratio should be kept above 3 in order to avoid carbon deposition and enhance hydrogen production while minimizing methane and carbon monoxide formation. However, energy input necessary to evaporate extra water limits the usage of very high steam to ethanol ratios. As a result of these considerations, steam to ethanol ratio was selected as 3.2 in this study.

3.3 CATALYSTS USED IN STEAM REFORMING OF ETHANOL

Other than thermodynamic limitations that affect the hydrogen productivity, the most important factor in this process is the catalyst selection, which could alter the pathway of reaction network. Selected catalyst should maximize hydrogen selectivity via activating ethanol steam reforming reaction, while minimizing side product formation by inhibiting cracking reactions and coke formation. Catalyst properties which are specified by the metals selected, their proportions and synthesis method used

has an important impact on the activity of the catalyst. While active metal generally used for the cleavage of C-C bonds in steam reforming of ethanol, catalyst support has also effects on the cleavage and activation of the bonds. For ethanol steam reforming reaction, generally noble metal catalysts such as Rh, Ru, Pd and Pt and non-noble metal catalysts such as Ni and Co have been extensively investigated [5].

3.3.1 Noble Metal Catalysts

Noble metal catalysts are found to be very active towards ethanol steam reforming reaction. Liguras et al. [16] investigated the effect of Rh, Ru, Pd and Pt loaded on Al₂O₃ support material with metal loading changing between 0 wt.% and 5 wt.% between 600°C and 850°C and at a steam to ethanol ratio of 3. Rh catalyst was found to be the most active and selective noble metal towards hydrogen production by ethanol steam reforming reaction. Activity of Ru catalyst was very promising at high metal loadings and activity was stable in long term tests. Similar study conducted by Erdohelyi et al. [17] suggested that Ru catalyst supported by Al₂O₃ (1 wt.%) results in higher activity towards hydrogen formation followed by Rh catalyst at 450°C and at a steam to ethanol ratio of 3. In their study, Pt/Al₂O₃ catalyst favored formation of ethylene. When CeO₂ was used as the support instead of Al₂O₃, Rh catalyst showed higher hydrogen selectivity over Pd/CeO₂, Ir/CeO₂, Pt/CeO₂ and Ru/CeO₂. Surprisingly, Ru/CeO₂ and Pd/CeO₂ catalysts was more active towards acetaldehyde formation, probably due to basic nature of CeO₂ proving the importance of the catalyst support properties. Ir/CeO₂ catalyst was proven to be very active and stable at 650°C and at a steam to ethanol ratio of 3.2 towards hydrogen production according to Zhang et al. [18]. As primary reaction, ethanol dehydrogenation to acetaldehyde occurrence was reported which than decomposed to carbon monoxide and methane and reformed to hydrogen. Ir was active in breaking C-C bonds and CeO₂ was believed to be responsible from the activation of water molecules favoring the steam reforming reactions. When MgO was used as support for Rh (3 wt.%), Pd (3 wt.%), Co (21 wt.%)

and Ni (21 wt.%) for ethanol steam reforming reaction at 650°C and at a steam to ethanol ratio of 8.4 by Frusteri et al. [19], Rh catalyst showed complete ethanol conversion differently from other catalyst, but hydrogen selectivity did not reach to the result of Ni/MgO catalyst. 0.5 wt.% Pt loaded Al₂O₃, CeO₂ and ZrO₂ catalysts were investigated by Panagiotopoulou et al. [20] at a steam to ethanol ratio of 3 and at between 300°C and 400°C. ZrO₂ supported Pt showed slightly higher ethanol conversion and lower carbon monoxide formation. CeO₂ support was found ineffective for ethanol steam reforming compared to Al₂O₃, and ZrO₂ supported catalysts and it was more active towards decomposition reaction.

3.3.2 *Non-noble Metal Catalyst*

The high cost of noble-metal catalysts lead to the search of non-noble metal catalysts that are active for ethanol steam reforming reaction. Especially, Ni and Co were found to be very active towards hydrogen production. They were investigated with different supports, such as MgO, ZrO₂, Al₂O₃, CeO₂, TiO₂ and SiO₂ [21]. Co was used in ethanol steam reforming due to its activity in breaking C-C bonds and suppressing methanation and decomposition reactions of ethanol [5]. Soykal et al. [22] studied Co/CeO₂ in ethanol steam reforming at between 350°C and 500°C and at a steam to ethanol ratio of 10 and catalyst found to be very active at 500°C resulting in 80% hydrogen yield with very low carbon monoxide formation. Torres et al. [11] investigated Co catalyst supported by ZnO and promoted with Fe or Mn at 500°C with a steam to ethanol ratio of 8 and found to be very active leading to hydrogen selectivity at about 70% by minimizing methane formation. Haga et al. [23] compared the effect of catalyst supports used with Co in ethanol steam reforming reaction and found that selectivity of hydrogen decreased in the order: Co/Al₂O₃> Co/ZrO₂> Co/MgO> Co/SiO₂>Co/C. ZnO catalyst support used with Co by Llorca et al. [24] at 450°C with a steam to ethanol ratio of 5 resulted in very high hydrogen selectivity (73%), very low carbon monoxide selectivity (1.1%) and showed to be stable in long term, for 75 h.

Nickel based catalysts are generally preferred over noble metal catalysts and other non-noble metal catalysts due to their low cost, availability, superior capability in the cleavage of C-C, C-H and O-H bonds despite their high tendency for carbon formation and deposition [25]. Ni is active towards ethanol steam reforming, acetaldehyde steam reforming, hydrogenation/dehydrogenation and water gas shift reactions [26]. Fatsikostas et al. [27] studied Ni catalysts supported on La_2O_3 or γ - Al_2O_3 materials and found that while La_2O_3 catalyst showed stable activity and ethanol conversion in the range of 300°C and 650°C at which complete conversion was reached. Also reaction products were H_2 , CO , CO_2 , CH_4 , $\text{C}_2\text{H}_4\text{O}$ and C_2H_4 in the experiments conducted with the $\text{Ni}/\text{La}_2\text{O}_3$ above 550°C. Formation of high amounts of C_2H_4 which is known to be formed through ethanol dehydration reaction with Ni/γ - Al_2O_3 catalyst indicates significant coke deposition. Al_2O_3 supported catalysts were also reported by many other researchers as coke promoters, due to their strong acidic sites. Alberton et al. [28] reported the main reaction occurring on Ni/γ - Al_2O_3 was ethanol dehydration to ethylene at 600°C with a steam to ethanol ratio of 3. Other than La_2O_3 and γ - Al_2O_3 materials, various metal oxides such as TiO , MgO , ZnO , CeO_2 , ZrO_2 and mixed oxides such as $\text{CeO}_2/\text{ZrO}_2$ have been used for ethanol steam reforming reaction with nickel. Vizcaino et al. [29] studied nickel catalysts based on ternary mixed oxides; NiMgAl , NiCaAl , NiZnAl , NiMgLa and NiMgCe in ethanol steam reforming at 600°C with a steam to ethanol ratio of 3.7. Best catalytic performance among these catalysts was obtained with NiCaAl catalysts with 87% hydrogen selectivity and minimum coke deposition (0.219 g/g_{cat} h). NiMgLa and NiMgCe catalysts lead to formation of significant amounts of acetaldehyde and with other catalysts methane formation rate was high indicating high activity towards cracking reactions. Shi et al. [30] studied nickel catalysts supported by MgO , CeO_2 and MgO-CeO_2 in a temperature range of 300-500°C with a steam to ethanol ratio of 3 and found that $\text{Ni}/\text{MgO-CeO}_2$ catalysts exhibits better performance towards ethanol steam reforming compared to single supports approaching to 90% hydrogen selectivity at 500°C. Nichele et al. [31] investigated the effect of using ZrO_2 and Ca promoted ZrO_2 supports for nickel catalysts since in order to neutralize highly acidic sites of ZrO_2 with a basic metal oxide. While Ni/ZrO_2 was found to be very active in ethanol steam

reforming, catalyst deactivation due to coke formation occurred, as expected. CaO incorporated catalyst improved hydrogen productivity and coking resistance of the catalysts. Li et al. [26] also analyzed Ni/ZrO₂ catalyst with different crystalline phases and particle sizes for ethanol steam reforming and smaller nickel particle size and tetragonal zirconia support compared to monoclinic support showed higher reforming activity and at high temperatures also higher stability. Nichele et al. [32] investigated the performance of Ni/TiO₂ catalyst. Main parameters that affected the catalytic performance of TiO₂ supported catalysts was found to be nickel reducibility and stability.

3.4 COKE FORMATION ROUTES IN STEAM REFORMING OF ETHANOL

Hydrogen productivity and ethanol conversion in ethanol steam reforming reaction depends on many factors, such as type of active metal used, type of catalyst support, catalyst synthesis route, presence of additional metals and operating conditions. Among active metals investigated by many researchers, Ni found as being the most promising catalyst for high purity hydrogen production. However, Ni catalysts suffer from deactivation due to coke formation, limiting the usage of nickel based catalysts in long term applications. Deposited coke could rupture catalyst structure and reduce surface area leading to deactivation of the catalyst [5].

Coke formation may occur following different pathways on nickel based catalysts. When operations are carried out at moderate to high temperatures, carbonaceous intermediates may form and condense on the surface via Boudouard reaction (R. 16) or methane decomposition (R. 15), respectively. Another pathway for carbonaceous deposits to accumulate on the catalyst is ethanol dehydration to ethylene which is known as a strong coke formation promoter. Dehydration of ethanol to ethylene on acidic sites of catalyst could lead to formation of highly reactive carbon species which polymerizes to less active carbon. Three types of carbon that could be observed in steam reforming of ethanol process were reported in the literature; amorphous carbon, filamentous carbon and graphitic carbon which are different in

morphology and reactivity. Amorphous carbon is reported to be very active, can easily be removed from the catalyst surface at low temperatures and may not cause deactivation of the catalyst while others require high temperatures to oxidize and could limit the activity of the catalysts [33, 34]. Coke formation could occur following gas phase reactions resulting in the formation of carbonaceous intermediates. Part of this carbon may gasify and then react (steam reforming) or dissolve in the nickel crystallites and precipitate [34–36]. Continuous precipitation could lead to formation of filamentous carbon, which does not cause direct catalyst deactivation, but continuous deposition could plug the catalyst pores and rupture the structure [28]. Precipitated carbon through dissociation of CO (Boudouard reaction, R.16) between nickel and the support may create carbon islands formed by graphitic carbon. This type of carbon also does not cause significant catalyst deactivation, unless it encapsulates or removes nickel from the surface [27]. If precipitation continues at the rear end of the crystallite, carbon whiskers grow and eventually result in deactivation of catalyst by lifting and leading to fragmentation of nickel from the surface causing deactivation of the catalyst [36].

Coke formation can be minimized by optimization of operating conditions such as operating temperature and steam-to-ethanol ratio and formulation of the catalyst [31]. Low temperatures are preferred for ethanol steam reforming reaction to achieve energy conservation. Unfortunately, coking is generally observed near temperatures of 500°C due to insufficient gasification by steam. At high temperatures, filamentous and graphitic carbon can be removed by steam with gasification reactions [25]. Minimization of coke formation can be achieved by using feedstock having high steam-to-ethanol ratios. Increase of partial pressure of steam in the reaction medium increases the chemisorbed water on the catalyst leading to higher gasification of coke deposited on the surface [33, 37].

CHAPTER 4

IDEAL CATALYSTS FOR STEAM REFORMING OF ETHANOL

Support material used for nickel based catalysts plays a crucial role for determining the activity of the catalyst in steam reforming of ethanol process. Used support has an important influence on the cleavage and the activation of the bonds and properties of nickel such as reducibility, dispersion on the support surface and resistance to thermal sintering. In order to have high hydrogen productivity with minimum carbon deposition that could allow long term stability, it is required to use a catalyst support that possess;

- High thermal and chemical stability that allows high temperature operations
- High surface area providing high concentration of active sites per mass of catalyst
- Strong interaction with nickel that can stabilize it and prevent it from sintering at high temperature operations.

Surface and structural properties of catalyst depends on the metals selected as support and preparation route of the support [40–42].

4.1 MESOPOROUS MATERIALS

Since the discovery of MCM-41 (Mobil Crystalline Matter No. 41) type silicate based materials by Mobil in 1992, high surface area mesoporous molecular sieves with ordered pore structure attracted significant attention due to their potential application

in reaction and separation processes. According to International Union of Pure and Applied Chemistry definition, materials with pore diameters between 2 nm and 50 nm are called mesoporous materials. Materials having pore diameter smaller than 2 nm are classified as microporous materials and higher than 50 nm are called macroporous materials. Due to high and adjustable pore diameter and pore shape of these materials, diffusion limitation problem in reaction systems was broken.

MCM-41 material possess a one dimensional hexagonal array of uniform mesopores and surface area of this material is above 700 m²/g. They can be synthesized by using templating agents as ionic surfactants such as cetyltrimethylammonium bromide (CTMABr) and cetyltrimethylammonium chloride (CTMACl) and by changing the chain length of surfactant molecules pore size of MCM-41 can be adjusted. The crucial problem with MCM-41 is its poor hydrothermal stability limiting usage of this material in reactions involving steam. SBA-15 (Santa Barbara Acid) discovered by Zhao et al. [42] which is also a mesoporous silica based material with ordered pore structure and was preferred over MCM-41. SBA-15 possess cylindrical two dimensional hexagonally ordered pores and thicker walls giving it a much higher hydrothermal stability. Due its highly acidic synthesis route, SBA-15 type materials possess a slightly acidic nature. Differently than MCM-41, SBA-15 has micropores in the silica walls caused by the surfactant (Pluronic P123) used during the synthesis [43]. Despite their advantageous properties, catalytic activity of these materials is very low and incorporation of metals is required to obtain high catalytic activity and stability. Even when nickel was impregnated to MCM-41 and SBA-15, hydrogen production was not very successful and high coke deposition rate was observed [44].

4.2 ZIRCONIA INCORPORATED MESOPOROUS MATERIALS

Ideal support used for ethanol steam reforming catalyst should possess a strong interaction with nickel which would prevent nickel from sintering during high temperature operations. Zirconia containing catalysts has been considered for ethanol steam reforming reaction lately, due to their high thermal and chemical stability, strong

interaction with nickel and high water adsorption-dissociation capability allowing an optimum environment for hydrocarbon gasification and water gas shift reaction [40, 41, 45]. Zirconia contains Lewis acidity which is unfavorable for ethanol steam reforming reaction leading to coke deposition, but Youn et al. [46] reported that moderate acidity enhances the catalytic performance of a catalyst in ethanol auto-thermal reforming reaction. Also they found that electronic structure of nickel was modified by ZrO_2 , favoring the steam reforming reaction while MgO and ZnO supported nickel catalysts prevented active metallic nickel formation. Moreover, zirconia surface contains hydroxyl groups which improves the performance of the catalyst in steam reforming reaction [47]. Li et al. [26] investigated Ni catalysts supported on ZrO_2 with different crystalline phases in ethanol steam reforming reaction at 400°C with a steam to ethanol ratio of 3. According to their findings, smaller zirconia crystal size enhances the interaction with nickel particles, resulting in higher activity. Smaller zirconia crystals as well as small nickel crystals suppresses coke formation. Tetragonal zirconia phase was found to be more active in water gas shift reaction compared to monoclinic zirconia phase and ethanol steam reforming tests performed at 600°C resulted in high hydrogen production with a hydrogen yield of 80%. Benito et al. [48] also obtained high ethanol steam reforming activity with zirconia containing monoclinic and tetragonal phases supported nickel catalyst and reached over 75% hydrogen yield with high stability at 700°C and with a steam to ethanol ratio of 6.4. They also investigated silica incorporation to ZrO_2 structure in order to stabilize the tetragonal zirconia phase which was found to be the active phase for this reaction. Incorporation of silica modified the crystal structure, textural properties and surface acidity of the catalyst, increasing the efficiency of the catalyst towards hydrogen production. Instead of incorporating silica to zirconia, other researchers incorporated zirconia into mesoporous silica structures such as SBA-15 and MCM-41 for various reactions [25, 40, 45, 49, 50]. Incorporation of zirconia into silica structure is advantageous due to the higher surface area and more stable structure of the final product. Also, zirconia incorporation was reported to enhance hydrothermal stability and alkali resistance of mesoporous silica structures [49, 51]. Seo et al. [45] reported that zirconia incorporation enhanced the resistance of silica to

steam and increased the metal-support interaction preventing growth of nickel crystals during calcination of the material. In the reaction of steam reforming of liquefied natural gas, zirconia incorporation affected the catalytic activity significantly. Ni (20 wt. %)/SiO₂-ZrO₂ catalyst containing Zr/Si=0.54 found to be very active for LNG conversion and hydrogen production. The main reasons for high activity was believed to be due to the role of zirconia in adsorption and spillover of steam from the support to nickel crystals and the crystal size of metallic nickel. Wan et al. [50] investigated Ce_xZr_{1-x}O₂ promoted Ni based SBA-15 catalysts in methane steam reforming reaction and Ce_xZr_{1-x}O₂ promoter increased methane conversion compared to Ni/SBA-15. Takahashi et al. [49] added zirconia in silica structure in order to increase the steam resistance of the material for methane steam reforming reaction. It was found that while Ni/SiO₂ loses its activity at high temperature due to destroyed pore structure by the presence of steam, Ni/SiO₂-ZrO₂ catalyst showed stable activity and preserved its pore structure after reaction. Other than reforming reactions, SiO₂-ZrO₂ supports used in reactions requiring an acidic catalyst. Zr-SBA-15 catalyst was used by Iglesias et al. [52] for transesterification of crude palm oil with methanol for biodiesel synthesis and catalyst showed superior activity and stability.

Despite all advantageous properties, acidity of SiO₂-ZrO₂ catalysts which causes coke formation limits their high activity in steam reforming reactions. Zirconia based catalysts have been modified in order to reduce its acidity and thus increase stability with basic metal oxides such as MgO or CaO. They could prevent excessive carbon deposition by favoring gasification and preventing ethanol dehydration to ethylene [29, 53, 54]. Garcia et al. [54] incorporated MgO to zirconia in order to decrease the acidity and increase the activity of the catalyst in carbon dioxide reforming of methane. MgO addition to catalyst support resulted in stabilized tetragonal zirconia phase, increase of thermal stability and decrease of acidity which enhanced the stability of the catalyst by preventing deactivation and decrease of the reducibility of nickel causing necessity to increase the reduction temperature.

4.3 CeO₂/ZrO₂ MATERIALS AS CATALYST SUPPORTS

Ceria is a stable fluorite type oxide and has been used in various reactions such as water gas shift, NO oxidation, methanol steam reforming and CO oxidation other than ethanol steam reforming reaction as catalyst support or promoter. Ceria is preferred because of its unique properties providing strong metal-support interaction, high oxygen storage and release capability and increased metal dispersion. Good redox and metal-support interaction properties increases catalytic activity and coking resistance of CeO₂. CeO₂ inhibits the dissolution and diffusion of carbon species through nickel clusters. It also enhances the adsorption of steam to its surface by increasing active surface oxygen concentration which can remove the deposited carbon species [22, 33, 55, 56]. Studies showed that the incorporation of ZrO₂ to CeO₂ enhances oxygen storage and release capacity through the redox process by Ce⁴⁺/Ce³⁺ and nickel dispersion of the material. Moreover, ceria is known to have a sintering problem that decreases its surface area at high temperatures and ZrO₂ incorporation increases its thermal stability [33, 57, 58]. ZrO₂ incorporation creates mobile lattice oxygen available for reduction increasing the reducibility of the material [59].

Jalowiecki-Duhamel et al. [39] studied ethanol steam reforming reaction with cerium-nickel mixed oxide catalysts (CeNi_xO_y (0<x<5)) at between 200°C and 500°C and with a steam to ethanol ratio of 3. While they reached complete ethanol conversion at 400°C, they obtained 70% hydrogen in product gas stream at 300°C. Biswas and Kunzru [60] investigated Ni/CeO₂-ZrO₂ catalyst synthesized with co-precipitation with ammonia with changing CeO₂/ZrO₂ ratios in ethanol steam reforming reaction at a temperature range of 400 to 650°C and with a steam to ethanol ratio of 8. Most successful result which was 5.8 mol hydrogen production from one mol of ethanol was obtained with Ni/CeO₂-ZrO₂ catalyst having CeO₂/ZrO₂ ratio of 4 at 600°C. The most important reasons for high activity of this catalyst over the other was believed to be its high oxygen storage capacity which enhanced the availability of surface oxygen and degree of reduction of nickel changing accordingly with properties of the support. Srinivas et al. [61] also studied ceria-zirconia supported nickel catalysts with changing metal contents in ethanol steam reforming reaction at 550°C, with a steam to ethanol

ratio of 8. The best metal content for Ni:CeO₂:ZrO₂ found to be 40:30:30 (wt. %) that gave 68% hydrogen production and did not deactivate for time-on-stream tests extending up to 500 h. Other than ethanol steam reforming, CeO₂/ZrO₂ supported nickel catalysts were also used in partial oxidation of methane [62], steam reforming of acetic acid [63], carbon dioxide reforming of methane [33, 64, 65] and oxidative steam reforming of methanol [66]. Takeguchi et al. [62] analyzed reduction behaviors of NiO modified CeO₂-ZrO₂ catalysts and their activity towards partial oxidation of methane. They found that catalytic activity increased with increasing oxygen storage capacity and interaction of support with nickel particles. Catalysts having weak interaction between nickel and CeO₂-ZrO₂ resulted in high coke formation. Hu et al. [63] investigated steam reforming of acetic acid between 650-750°C with a steam to acetic acid ratio of 3 by using Ni/CeO₂-ZrO₂ catalysts. High conversion and hydrogen yield were obtained, but catalyst deactivation occurred due to coke formation with time-on-stream. Kumar et al. [33] studied nickel based ceria, zirconia and ceria-zirconia catalysts in carbon dioxide reforming of methane at 700°C. Ni/Ce_{0.6}Zr_{0.4}O₂ synthesized using a surfactant (CTAB) was found to be the most active catalyst and preserved its stability for 100 h. they stated that the stability of ceria-zirconia depends on its enhanced reducibility at lower temperatures compared to ceria and zirconia. Perez-Hernandez et al. [66] used single ZrO₂ and mixed CeO₂-ZrO₂ oxides with different CeO₂/ZrO₂ ratios were as catalyst supports for nickel in oxidative steam reforming of methanol. CeO₂ rich supported catalyst showed the best catalytic activity and stability without noticeable deactivation. Ni-ZrO₂ catalyst presented high hydrogen selectivity, but poor methanol conversion. Synthesis method applied for CeO₂-ZrO₂ is also proven to have an important effect on the activity of the catalyst and coke deposition in carbon dioxide reforming of methane. Crnivec et al. [65] and Djinovic et al. [64] found that CeO₂/ZrO₂ synthesized by following glycothermal reduction method result in much smaller CeO₂ crystalline sizes (6 nm) compared to the materials synthesized with deposition precipitation method (20-82 nm). Difference in crystal size and morphological differences between two materials changed carbon deposition rates significantly in CH₄-CO₂ dry reforming, favoring the glycothermal reduction method.

4.4 OBJECTIVES

The main objective of this study is to achieve the highest hydrogen productivity with minimum coke deposition in ethanol steam reforming reaction in a temperature range of 400-650°C. In order to accomplish this objective, the scope of this study is to synthesize zirconia-silicate and ceria-zirconia supported nickel catalysts with various metal contents, high surface area and strong metal-support interaction and to optimize catalyst properties according to its success in ethanol steam reforming process.

CHAPTER 5

EXPERIMENTAL METHODS

Experimental methods include four main parts, which are catalyst synthesis, characterization of the synthesized catalysts, activity tests in ethanol steam reforming reaction system and lastly characterization of the catalysts used in activity tests in this study. Firstly, catalytic supports are synthesized. The catalyst supports selected for this study for high purity long-term hydrogen production are CeO₂-ZrO₂ mixed oxide materials, CeO₂, ZrO₂, Zr-SBA-15, Zr-MCM-41, Ce-Zr-SBA-15 and Mg-Zr-SBA-15 type mesoporous materials. After the synthesis of support materials, nickel impregnation was performed and the resulting materials were characterized to understand their structural and physical properties.

5.1 CATALYST SYNTHESIS METHODS

5.1.1 *Synthesis of ZrO₂ catalyst support*

Mesoporous ZrO₂ support was synthesized following a hydrothermal procedure (Figure 11), similar to the route described by Tsoncheva et al. [67]. In this method, hexadecyltrimethyl ammonium bromide (CTMABr) supplied by Merck was used as the surfactant, zirconium (IV) oxynitrate hydrate (Sigma Aldrich, >99% purity) was used as zirconia source and ammonia solution (25%, Merck) was used as pH regulator.

Firstly, surfactant solution (2 g of CTMABr in 50 mL of deionized water) was prepared at 30°C and stirred until a clear solution was obtained. Surfactant solution

was added into zirconium(IV) oxynitrate hydrate solution dissolved in 30 mL of deionized water dropwise. Then, ammonia solution was added until the pH of solution became 10.0. Final solution was stirred at 50°C for 24 h, then put into a teflon bottle, which was placed into a stainless-steel autoclave. Hydrothermal synthesis was performed at 100°C for 96 h. The solid product produced was filtered and washed with deionized water, dried and calcined at 450°C with dry air for 4 h.

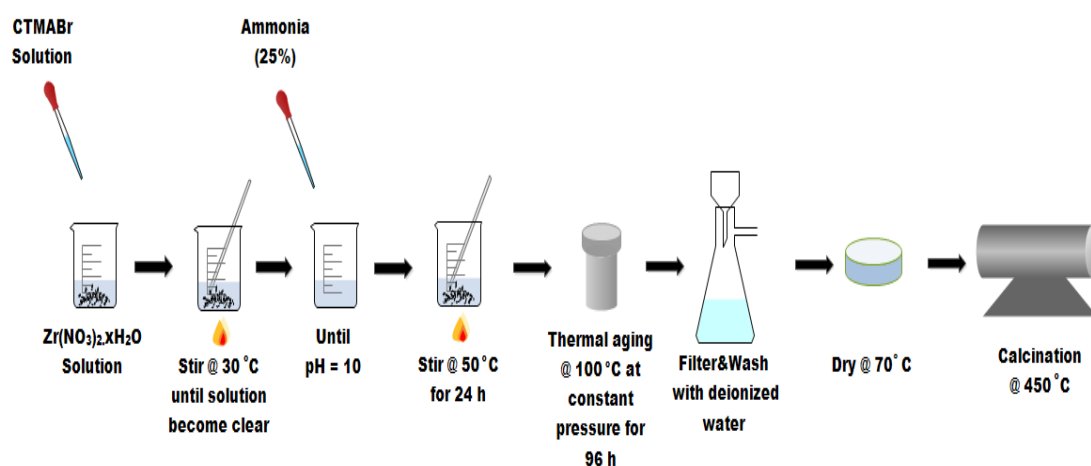


Figure 11: Synthesis procedure of ZrO₂ catalyst support.

5.1.2 Synthesis of Zr-SBA-15, Ce-Zr-SBA-15 and Mg-Zr-SBA-15 catalyst supports

Zr-SBA-15, Ce-Zr-SBA-15 and Mg-Zr-SBA-15 were synthesized following the hydrothermal procedure reported by Mbraka et al. [68] (Figure 12). For the synthesis, poly(ethylene glycol)-block-poly(propylene glycol)-block-poly(ethylene glycol), Pluronic P123 supplied by Sigma-Aldrich was used as surfactant, tetraethyl orthosilicate (TEOS) supplied by Merck was used as the silica source, zirconium(IV) oxynitrate hydrate, cerium(III) nitrate hexahydrate and magnesium chloride hexahydrate (Sigma Aldrich, >99% purity) were used as the metal sources.

In the synthesis, 2 g surfactant (Pluronic 123) was dissolved with deionized water (62.5 ml) and hydrochloric acid (12.5 ml). 4.1 ml of TEOS was added dropwise

to the surfactant solution which is highly acidic ($\text{pH} < 1$). Required amount of zirconium(IV) oxynitrate ($\text{Zr}/\text{Si}=0.3$) and if used, cerium(III) nitrate hexahydrate or magnesium chloride hexahydrate ($\text{Mg}/\text{Si}=0.15$) were added to the solution which was then put into a teflon bottle, placed into a stainless-steel autoclave. Hydrothermal synthesis was performed at 90°C for 48 h. The resulting solid product was filtered and washed with deionized water, dried and calcined at 600°C with dry air for 6 h.

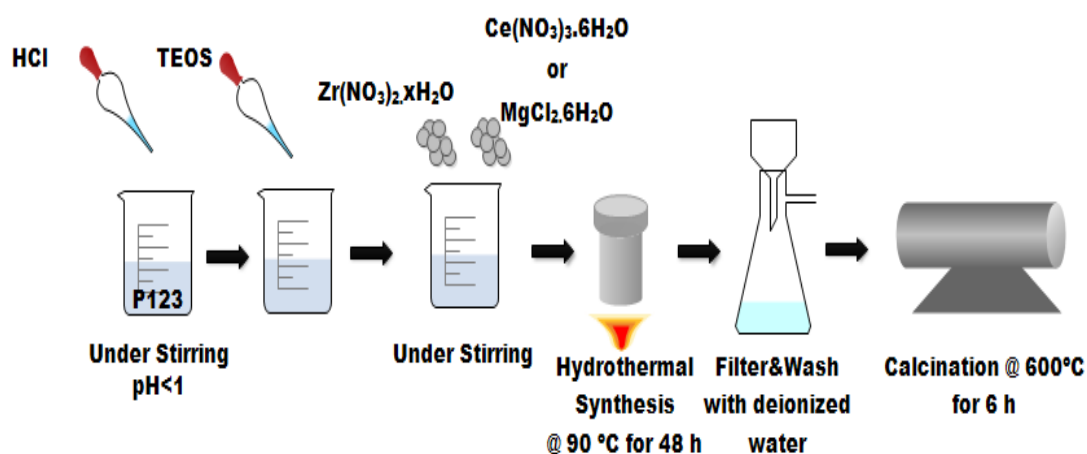


Figure 12: Synthesis procedure of Zr-SBA-15, Ce-Zr-SBA-15 and Mg-Zr-SBA-15 catalyst support

5.1.3 Synthesis of Zr-MCM-41 catalyst support

Synthesis of Zr-MCM-41 was performed following a procedure similar to the one (Figure 13) described by Wang et al. [69]. In this method, hexadecyltrimethyl ammonium bromide (CTMABr) supplied by Merck was used as the surfactant, zirconium (IV) oxynitrate hydrate (Sigma Aldrich, >99% purity) was used as zirconia source. NaOH (1 N, Merck) was used for pH adjustment and sodium silicate solution (Merck) was used as the silica source.

In the synthesis, 13.2 g surfactant (CTMABr) was dissolved with deionized water. Zirconium(IV) oxynitrate solution ($\text{Zr}/\text{Si}=0.3$) was added to surfactant solution dropwise under vigorous stirring. Then, 11.3 mL sodium silicate solution was added

to the surfactant solution and the pH was adjusted to 8.5 with NaOH. Final solution was put into a teflon bottle, placed into a stainless-steel autoclave. Hydrothermal synthesis was performed at 120°C for 96 h. The solid product produced was filtered and washed with deionized water until pH of the wash water became constant, solid product dried and calcined at 600°C with dry air for 6 h.

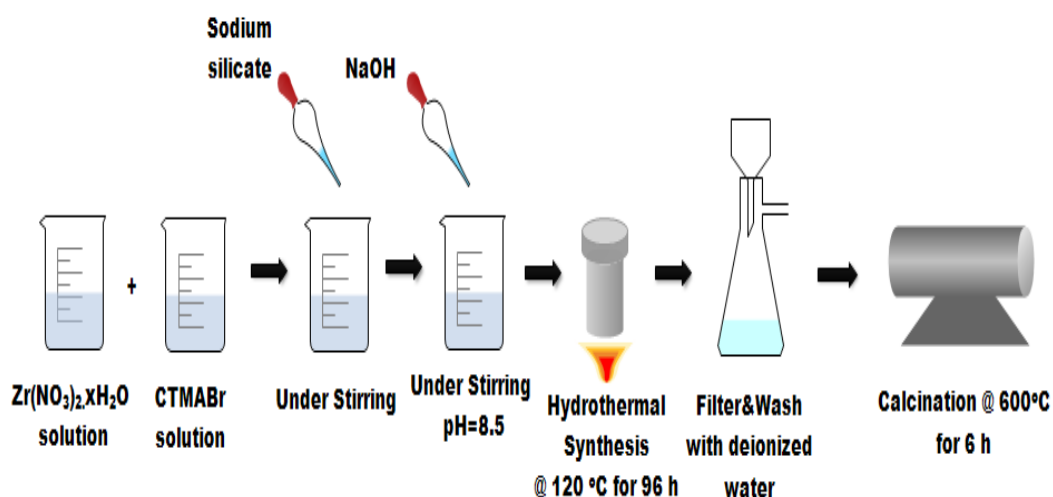


Figure 13: Synthesis procedure of Zr-MCM-41 catalyst support.

5.1.4 Synthesis of CeO₂-ZrO₂ Support Materials

CeO₂-ZrO₂ catalyst supports were synthesized following the synthesis method described by Djinovic et al. [64], using ethylene glycol (Merck, >99% purity), propionic acid (Merck, >99% purity), zirconium(IV) oxynitrate hydrate (Sigma Aldrich, >99% purity) and cerium(III) nitrate hexahydrate (Sigma Aldrich, >99% purity).

In the synthesis of CeO₂ and CeO₂-ZrO₂, 2 g of cerium (III) nitrate hexahydrate and the required amount (Table 3) of zirconium (IV) oxynitrate hydrate to have CeO₂/ZrO₂ ratio changing as 1, 2, 4 and 6 were dissolved in deionized water until a clear solution was obtained (Figure 14). Two ml of propionic acid and 60 ml of ethylene glycol were added to metal solution dropwise to enlarge surface modification

by esterification reaction. Formed ester and ethylene glycol behave like structure directing agents and lead to the formation of mesoporous structure. Resulting solution were placed in a teflon bottle, placed into a stainless-steel autoclave and hydrothermal synthesis was performed at 175°C for 4 h. Liquid portion of the product were separated from the gel by centrifugation at 9000 rpm in 10 min cycles. The resulting product was washed with ethanol and deionized water, dried and calcined with dry air for 6 h at 400°C.

Table 3: Metal composition of CeO₂-ZrO₂ catalyst supports

Catalyst Support	CeO ₂ /ZrO ₂ weight ratio
CeO ₂ -ZrO ₂ (1:1)	1
CeO ₂ -ZrO ₂ (2:1)	2
CeO ₂ -ZrO ₂ (4:1)	4
CeO ₂ -ZrO ₂ (6:1)	6

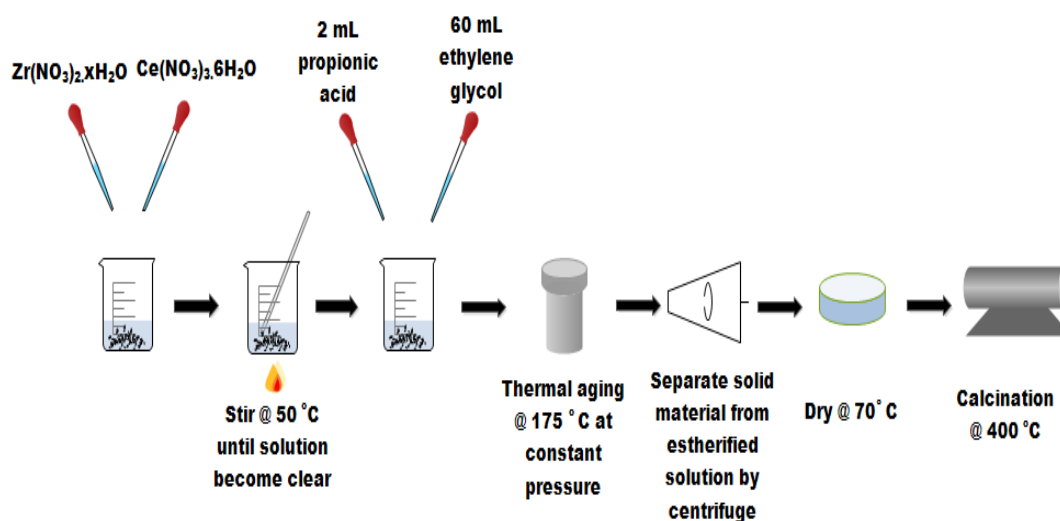


Figure 14: Synthesis procedure of CeO₂-ZrO₂ catalyst support.

5.1.5 Nickel Impregnation to the synthesized catalyst supports

After the synthesis of support materials nickel impregnation was conducted. Required amount (Table 4) of $\text{Ni}(\text{NO}_3)_2 \cdot 6\text{H}_2\text{O}$ (Merck, >99% purity) was dissolved in deionized water. Support materials were suspended in deionized water and after sufficient mixing, Ni solution was added to the suspension dropwise, under continuous stirring. The resultant mixture was stirred for 24 hours and dried at 60°C . Each solid product was calcined for 4 hours with dry air and reduced for 4 hours with hydrogen. For zirconia and zirconia-silicate supported catalysts, calcination and reduction temperature was 650°C . For $\text{CeO}_2\text{-ZrO}_2$ supported catalyst calcination and reduction temperature was changed from 400°C to 650°C (Table 4). $\text{CeO}_2\text{-ZrO}_2$ supported, nickel impregnated catalysts were named as $\text{Ni@CeO}_2\text{-ZrO}_2 (x:1)$, x representing the weight ratio of CeO_2 to ZrO_2 , changing from 1 to 6.

Table 4: Composition and Calcination & Reduction Temperatures of the Catalysts

Catalyst	Targeted Composition, (Ni wt. %)	Calcination Temperature (°C)	Reduction Temperature (°C)
Ni@CeO₂-ZrO₂ (1:1)	3	450	450
Ni@CeO₂-ZrO₂ (2:1)	3	450	450
Ni@CeO₂-ZrO₂ (3:1)	3	450	450
Ni@CeO₂-ZrO₂ (4:1)	3	450	450
Ni@CeO₂-ZrO₂ (5:1)	3	450	450
Ni@CeO₂-ZrO₂ (6:1)	3	400	400
		450	450
		500	500
		550	550
		600	600
		650	650
Ni@CeO₂	3	450	450
Ni@ZrO₂	6	650	650
Ni@Zr-SBA-15	6	650	650
Ni@Ce-Zr-SBA-15	6	650	650
Ni@Mg-Zr-SBA-15	6	650	650
Ni@Zr-MCM-41	6	650	650

5.2 CATALYST CHARACTERIZATION METHODS

Synthesized catalysts were characterized by X-ray diffraction (XRD, Rigaku Ultima-IV diffractometer), energy-dispersive spectroscopy (EDS; JEOL JSM- 6400), N₂ adsorption-desorption (Quantachrome Autosorb-6), X-Ray photoelectron spectroscopy (XPS, PHI 5000 VersaProbe) and diffuse reflectance FTIR spectroscopy (DRIFTS; Perkin Elmer Spektrum 1) techniques. Spent catalysts and coke formation were also characterized using X-ray diffraction (Rigaku Ultima-IV diffractometer), scanning electron microscopy (SEM; Quanta 400F Field Emission), transmission electron microscopy (TEM: JEOL 2100F HRTEM) and thermal analysis equipment (TGA; Shimadzu TA-60 WS). XRD, XPS, SEM, TEM and N₂ adsorption-desorption analysis were performed at Central Laboratory of Middle East Technical University, FTIR spectroscopy and thermal analysis were conducted at Chemical Engineering Department of Middle East Technical University. EDS analysis were performed at Metallurgical Engineering Department of Middle East Technical University.

5.2.1 X-Ray Diffraction Analysis

X-ray diffraction analysis generally gives information about the crystal structures of solids, especially for ordered materials. Diffraction is a property of crystals that are larger than X-ray wavelengths. Diffraction patterns are unique to crystalline metals.

Low angle XRD patterns are used to analyze the structure of ordered mesoporous materials such as SBA-15 and MCM-41. These materials only show diffraction peaks at low angles ($2\theta < 10^\circ$). MCM-41 type materials presents a sharp peak at around $2\theta = 2^\circ$ (100) and three reflection peaks corresponding to (110), (200) and (210) at between $2\theta = 2^\circ - 6^\circ$ indicating the ordered pore structure of the materials. SBA-15 type materials presents also a sharp peak (100) and two reflection peaks (110) and (200) at around $2\theta = 1^\circ - 2^\circ$.

Scherrer equation (Equation 1) can be used to calculate the crystal sizes of metals from the X-ray diffraction pattern. Peak location and the size of the full width at half max of the peak are necessary.

$$t_{\text{particle}} = \frac{C \times \lambda}{B \times \cos\left(\frac{2\theta}{2}\right)} \quad (\text{Equation 1})$$

C : crystal shape factor (0.89)

λ : Wavelength (0.154 nm)

B : Full width at half max

2θ : Peak angle

5.2.2 *N₂ Adsorption-Desorption Analysis*

Surface area, porosity, pore volume and pore size of catalytic materials can be obtained from N₂ adsorption-desorption isotherms. Nitrogen is used as the molecular probe and surface available for interaction with the reactant molecules is found with this technique. For the calculation of surface area, BET (Brunauer Emmett Teller) method is generally used. For the calculation of pore size distribution, various methods have been suggested such as BJH (Barrett, Joyner, Halenda) and DH (Dollimore-Heal). BJH pore size distribution data were presented in this study. Prior to the analysis, materials were degassed at 110°C for 6 hours for our study. Pore size distribution was determined from adsorption-desorption isotherms.

5.2.3 X-Ray Photoelectron Spectroscopy Analysis

X-Ray photoelectron spectroscopy is a surface analysis technique used to obtain information about the elemental composition and chemical states of the elements that exists on the surfaces of solid materials. The analyzed material is bombarded with monoenergetic soft X-rays while simultaneously the kinetic energies and the number of electrons escaping from the material are identified. Small variations in the kinetic energies also give information about the chemical states of the elements on the surface. XPS analyzes the elemental composition of the top surface (0-10 nm) and detection limit for most of the elements are in the parts per thousand range.

5.2.4 Energy-Dispersive Spectroscopy Analysis

Energy-dispersive spectroscopy is a technique used for elemental analysis and chemical characterization of materials. EDS is based on the collection and energy dispersion of the characteristic X-rays. Each element has a unique X-ray spectrum pattern. With the ionization by a high energy radiation, atoms in the material emit the characteristic X-rays. Since energy of X-rays are characteristic for atomic structure of the elements, the spectrum obtained with energy-dispersive spectroscopy indicates the element content and type in the sample analyzed.

5.2.5 Diffuse Reflectance FTIR Spectroscopy of Pyridine Adsorption (DRIFTS) Analysis

DRIFTS of pyridine adsorption is used to determine the nature of acidity; Lewis or Brønsted of the material analyzed. Before DRIFTS analysis, the materials were dried at 110°C, then 1 ml of pyridine was adsorbed on the materials. A reference

spectrum was recorded prior to the analysis with the samples that do not contain pyridine.

5.2.6 Scanning Electron Microscopy (SEM) Analysis

Scanning electron microscope is used to obtain highly magnified images of a sample surface by using focused electron beam. Beam of electrons interacts with the atoms and produces various signals that are used to obtain highly magnified images. Electron sample interactions are used to get information about the texture, chemical composition and crystalline structure of the sample surface. Kinetic energy carried by accelerated electrons dissipated as various signals which are secondary electrons, backscattered electrons, photons and heat. Secondary electrons produces SEM images and backscattered electrons are used to adjust contrast. Surface of the sample can be analyzed from selected areas and ranging from 1 cm to 1 μm in width. Chemical compositions of the selected areas can also be obtained by further analysis. SEM analysis was used in this study for determination of the type of deposited carbon on the catalysts used in activity tests.

5.2.7 Transmission Electron Microscopy (TEM) Analysis

Transmission Electron Microscopy is a special kind of material characterization equipment that uses imaging and diffraction techniques to analyze the microstructural and crystalline structures of the material. It is a technique that allows to obtain morphologic and crystalline information simultaneously by taking images from very small and thin segments of the material by magnification up to million times. TEM analysis was used in our study to analyze the structure of a catalyst used in activity tests.

5.2.8 Thermal Analysis (TGA)

TGA was used to determine the nature and amount of carbon deposition on catalysts in activity tests. The samples were exposed to air with increasing temperature and the weight change of the sample was monitored. Temperature range was between 20°C and 900°C with a heating rate of 10 °C/min.

5.3 EXPERIMENTAL SET-UP OF THE ETHANOL STEAM REFORMING PROCESS

The catalytic experiments were performed at atmospheric pressure and between 400 °C and 650 °C in the system given in Figure 15. The reaction system consists of a syringe pump (Cole Palmer), an evaporator, a furnace, a quartz fixed bed tubular reactor having an inner diameter of 13 mm, a condenser and a gas chromatograph (Agilent Technologies 6850). Thermal conductivity detector and Porapak S column were used in the gas chromatograph and Argon were selected as the reference gas.

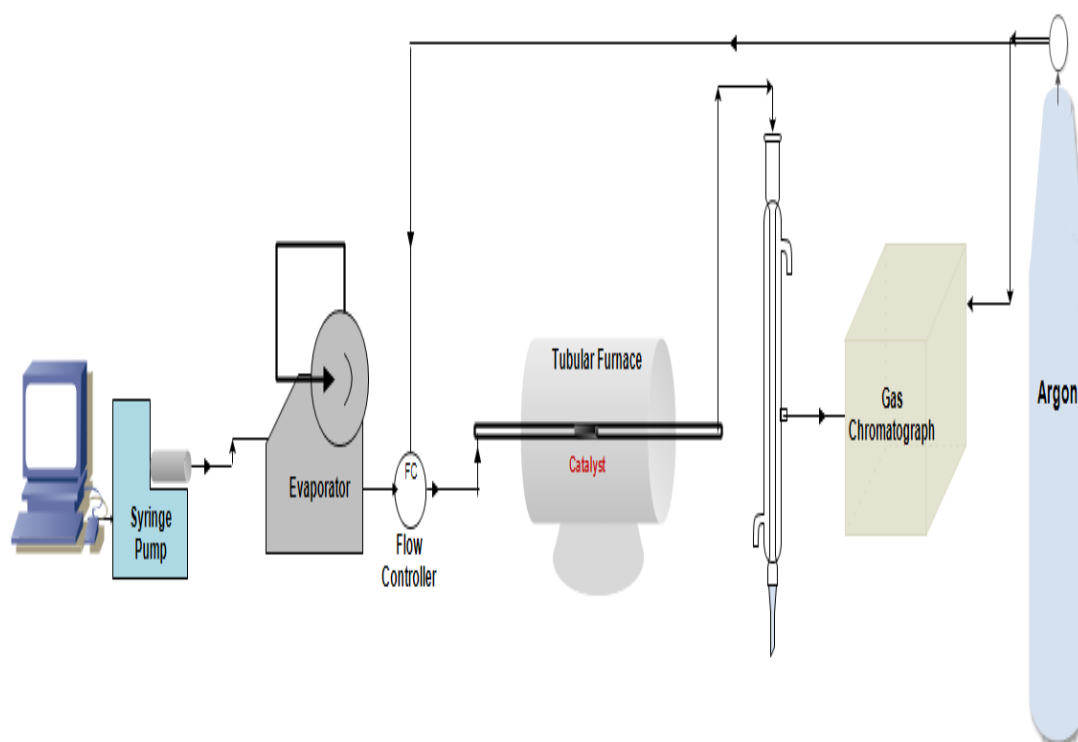


Figure 15: Schematical representation of experimental set-up

In each experiment 0.15 g catalyst was placed in the quartz reactor which was then put into the tubular furnace. The liquid feed was the mixture of water and ethanol having a $\text{H}_2\text{O}/\text{C}_2\text{H}_5\text{OH}$ molar ratio of generally 3.2 (1:1 volume ratio) and 4, 5 for some catalysts. The liquid feed was sent from syringe pump with a volumetric flow rate of 0.9 ml/h and evaporated in the evaporator which was at around 130-150°C. Then the vaporized feed having 20 ml/min volumetric flow rate was mixed with Argon which was passed through a flow controller at a rate of 30 ml/min. Then the gas stream having a flow rate of 50 ml/min passed from the reactor placed in a furnace and sent to the condenser to separate liquid products. Gas products were analyzed with the gas chromatograph placed after the condenser. All activity tests were conducted for 300 min. Space time was 0.18 gcat.s/ml.

Determination of the catalytic activities of the catalysts were done by calculating ethanol conversion (Equation 2), hydrogen yield (Equation 3) and product

distribution in the exit gas stream which mainly consists of H₂, CO, CO₂, CH₄, C₂H₄, (Equation 4). Detailed calculations are given in the Appendices section.

$$X_{\text{EtOH}} = \frac{\text{Moles of ethanol Reacted}}{\text{Moles of ethanol fed to the reactor}} \times 100 \quad (\text{Equation 2})$$

$$Y_{\text{H}_2} = \frac{\text{Moles of hydrogen produced}}{\text{Moles of ethanol fed to the reactor}} \times 100 \quad (\text{Equation 3})$$

$$\text{Mol \% of product Z} = \frac{\text{Moles of Z produced}}{\text{Total number of moles of products}} \times 100 \quad (\text{Equation 4})$$

in the product stream

CHAPTER 6

RESULTS AND DISCUSSION

6.1 CHARACTERIZATION RESULTS OF ZIRCONIA INCORPORATED MESOPOROUS CATALYSTS

Physicochemical properties of the synthesized supports are given in Table 5. The smallest surface area belongs to ZrO_2 material, as expected. Zr^{4+} containing SBA-15 and MCM-41 type support materials have much higher surface area and pore volume. This is expected for mesoporous materials with ordered pore structures. According to EDS measurements of silica-based materials, zirconia was not completely incorporated into the silica framework, possibly due to saturation in the micelles ability for accommodation of metal precursor [52]. Loss of zirconia was encountered with SBA-15 structures probably due to low pH of the synthesis mixture [43, 69]. Even though same Zr/Si ratio was aimed during the synthesis of SBA-15 and MCM-41 type materials, Zr incorporation into MCM-41 was much more successful with a Zr/Si ratio of 0.45. EDS analysis showed that only 7% of Mg^{2+} used in the synthesis solution was observed in the Mg-Zr-SBA structure. This indicated that most of the used Mg^{2+} did not precipitate upon addition of Zr^{4+} and Mg^{2+} salts to the solution or lost in the filtration & washing step of the synthesis procedure. Similar behavior was also observed with Zr^{4+} and Ce^{4+} incorporation to SBA-15. Basic natures of magnesia and ceria prohibited their incorporation to Zr-SBA-15 during its highly acidic synthesis procedure.

Table 5: Physicochemical properties of zirconia incorporated supports

Material	S _{BET} (m ² /g)	V _P (cm ³ /g)	D _P (nm)	Zr/Si		Mg/Si		Ce/Si	
				EDS	Synthesis	EDS	Synthesis	EDS	Synthesis
ZrO ₂	185	0.3	3.4	∞	∞	-	-	-	-
Zr-SBA-15	670	1.3	6.6	0.13	0.3	-	-	-	-
Ce-Zr-SBA-15	644	1.1	6.6	0.16	0.3	-	-	0.01	0.15
Mg-Zr-SBA-15	726	1.7	6.6	0.13	0.3	0.01	0.15	-	-
Zr-MCM-41	595	1.1	3.4	0.45	0.3	-	-	-	-

*EDS and synthesis results of Zr/Si, Mg/Si and Ce/Si indicates atomic ratios

N₂ adsorption/desorption isotherms and pore size distributions of the synthesized zirconia incorporated catalyst supports are given in Figure 16 and Figure 17, respectively. N₂ adsorption/desorption isotherms and pore size distributions of the nickel impregnated catalysts are given in Figure 18 and Figure 19, respectively. When surface areas, N₂ adsorption/desorption isotherms and pore size distributions of support materials and nickel impregnated catalysts are compared, it can be seen that other than a slight decrease in surface area, pore volume and pore diameter values after nickel impregnation (Table 5 and Table 6), there is no difference in the type of hysteresis loops and pore structures. All SBA-15 type materials showed Type IV N₂ adsorption isotherms and H1 type hysteresis loops, with an inflection between the relative pressures of 0.6 and 0.8. This sharp inflection is caused by capillary condensation in the mesopores according to IUPAC definition [70]. Catalysts containing Mg²⁺ exhibited higher pore volume resembling to the isotherms of pure SBA-15. When the relative pressure of closing point of hysteresis loops of supports and catalysts are compared, it was observed that hysteresis loops of catalysts closed at lower P/P₀ indicating slight pore blockage caused by nickel impregnation. Absence of the ordered uniform porous structure in MCM-41 type material is due to pore blockage caused by excess amount of Zr⁴⁺ incorporation. As it can be seen from Figure 18, Ni@ZrO₂ catalyst exhibited type H3 isotherm according to IUPAC definition indicating the presence of slit-shaped pores with a broad pore size distribution with

2.67 nm desorption pore diameter [70]. Other than hysteresis loop closing pressure, decrease of pore volume, pore diameter and surface area as a result of Ni incorporation is a sign of pore blocking caused by nickel (Table 6).

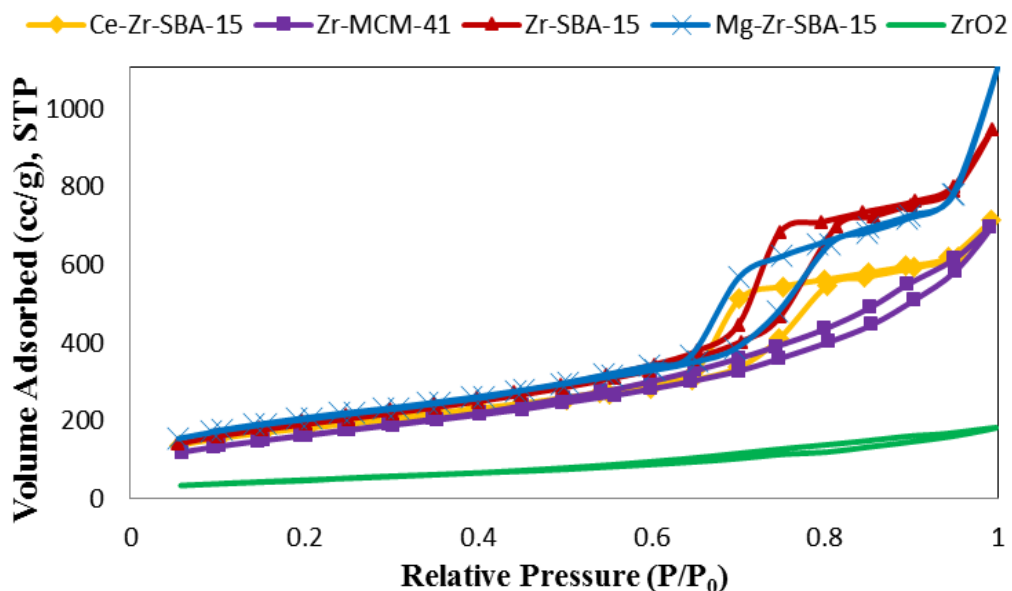


Figure 16: N₂ adsorption/desorption isotherms of the zirconia incorporated catalyst supports.

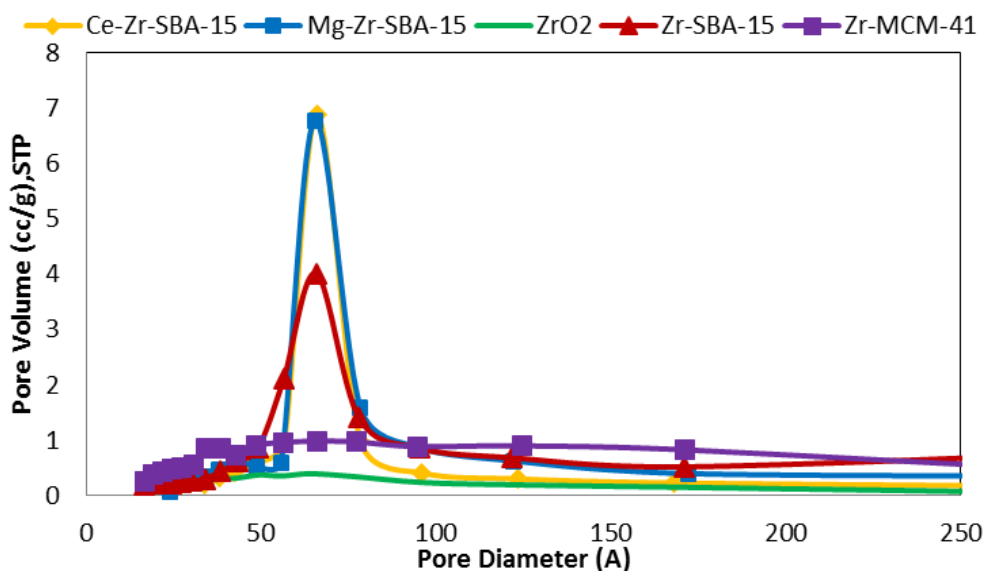


Figure 17: Pore size distribution of the zirconia incorporated catalyst supports.

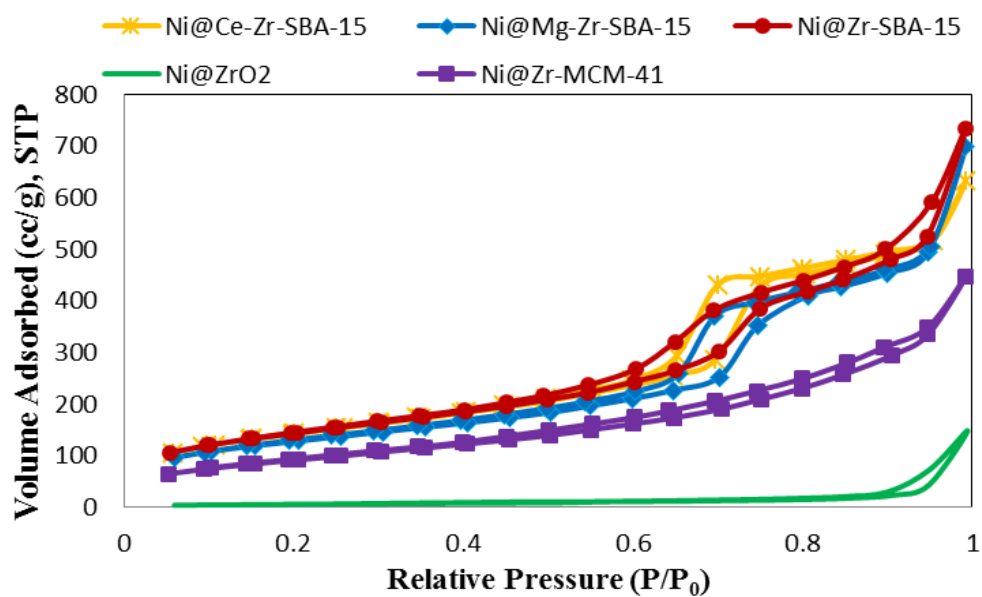


Figure 18: N₂ adsorption/desorption isotherms of Ni impregnated zirconia based catalysts.

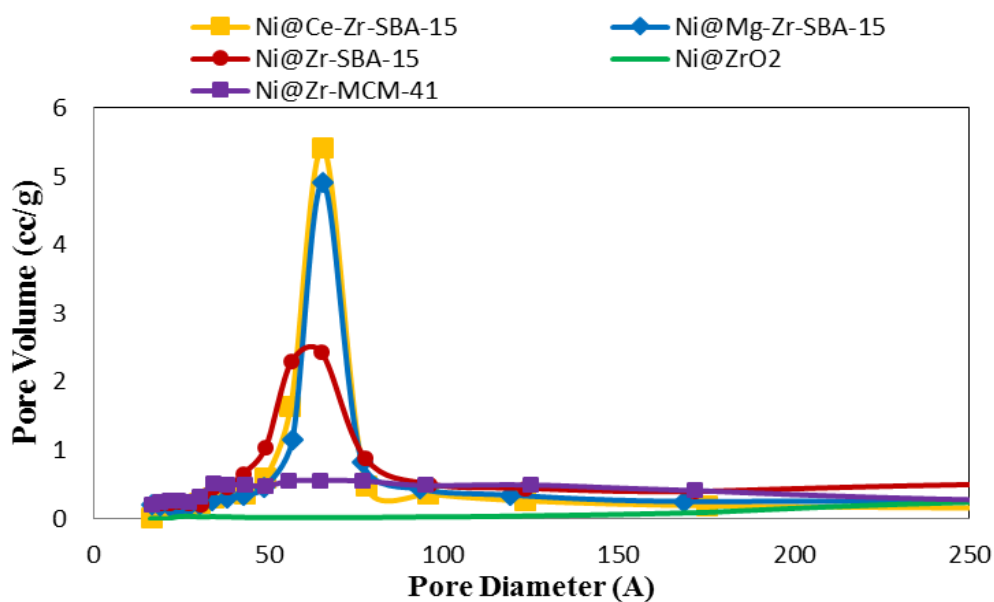


Figure 19: Pore size distribution of Ni impregnated zirconia based catalysts.

Table 6: Physicochemical properties of Ni impregnated zirconia based catalysts.

Material	S_{BET} (m²/g)	V_P (cm³/g)	D_P (nm)	Ni^o Crystal Size (nm)
Ni@ZrO₂	23.8	0.24	2.7	15.2
Ni@Zr-SBA-15	515	1.1	5.7	22.9
Ni@Ce-Zr-SBA-15	509	1.0	6.6	10.4
Ni@Mg-Zr-SBA-15	456	1.1	6.6	21.2
Ni@Zr-MCM-41	338	0.7	3.4	17.0

Low angle XRD patterns of the ZrO₂ support material and Ni@ZrO₂ catalyst are given in Figure 20. Absence of reflection peaks of main d₁₀₀ peak at low angle XRD patterns of both materials showed that there is no ordered pore structure in these materials. In the wide angle XRD pattern of the pure ZrO₂, presence of diffraction peaks at 30°, 50.4° and 60.2° suggested the formation of tetragonal zirconia phase. However, peaks positioned at 28.2° and 31.5° mainly showed the characteristics of the monoclinic phase and trace amounts of tetragonal phase in the wide angle diffraction pattern of Ni impregnated catalyst (Figure 21). Besides, peaks become narrower and more intense for Ni@ZrO₂ catalyst indicating the occurrence of crystalline growth which can also explain the loss of surface area after nickel impregnation (Table 5, Table 6). Scherer equation (Equation 1) reveals that average crystal size of zirconia calculated from the main peaks of the materials which are 30° for ZrO₂ and 28.2° for Ni@ZrO₂ increased from 4.4 nm to 21.3 nm, respectively. The nature of thermally unstable tetragonal-zirconia phase and high temperature treatment during its impregnation procedure may have caused tetragonal to monoclinic phase transformation and growth of crystal size of zirconia. It is reported that tetragonal phase of zirconia is meta-stable at room temperature and transformation to monoclinic phase was observed at high temperatures [45]. Another reason of phase transformation could be the crystal size growth of zirconia. When it exceeds a critical value, sintering proceeds and phase transformation from the tetragonal zirconia phase to monoclinic zirconia phase could take place according to Klimova et al. [71]. Other than zirconia,

metallic nickel phase was observed in the XRD pattern of Ni@ZrO₂ at 44.5°. Crystal size of Ni⁰ was calculated as 15.2 nm from Scherrer equation as presented in Table 6.

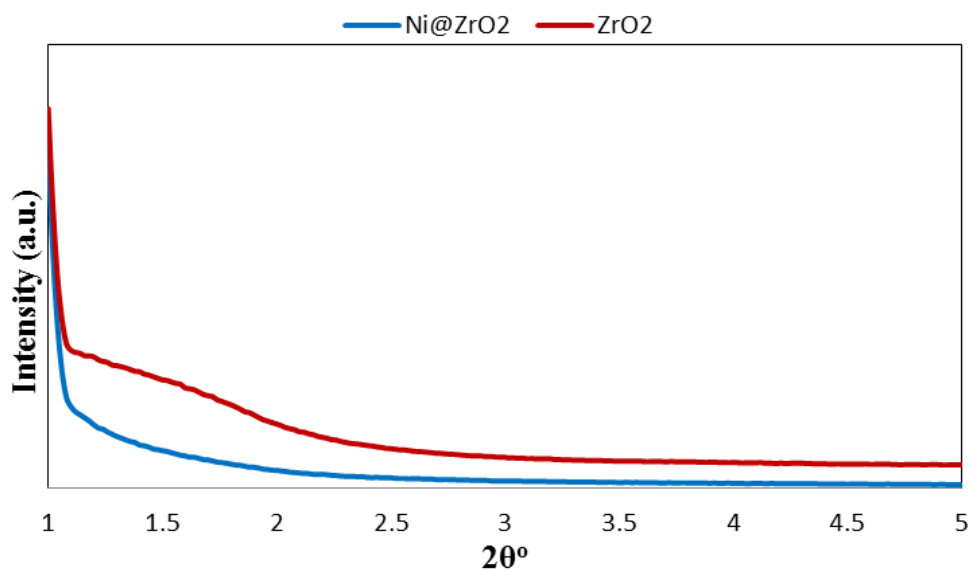


Figure 20: Low angle XRD pattern of ZrO₂ and Ni@ZrO₂.

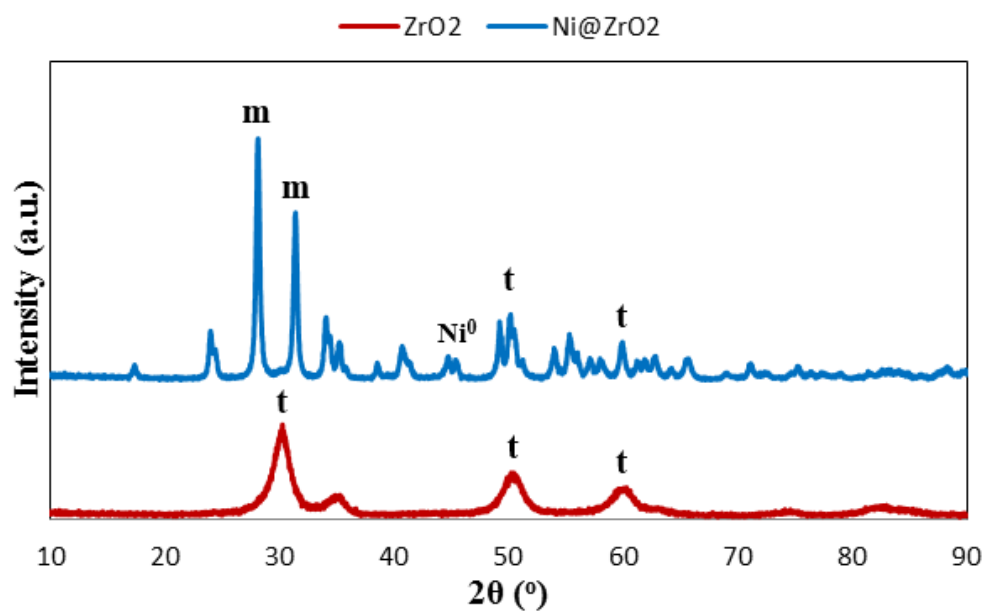


Figure 21: Wide angle XRD pattern of ZrO₂ and Ni@ZrO₂ (t represents tetragonal and m represents monoclinic zirconia phase)

Low angle X-ray diffraction patterns of the Ni@Zr-SBA-15, Ni@Ce-Zr-SBA-15 and Ni@Mg-Zr-SBA-15 catalysts given in Figure 22 exhibited two distinct reflection peaks of the main peak observed at about 1° , which corresponds to d_{100} . Reflection peaks of Ni@Zr-SBA-15 and Ni@Mg-Zr-SBA-15 are positioned at 1.5° and 1.7° indexed as (110) and (200) reflections, respectively, associated with hexagonal symmetry characteristic for SBA-15 [72]. For Ni@Ce-Zr-SBA-15 catalysts, these reflection peaks shifted about 1° to higher angles compared to other catalysts suggesting that the pore diameters were decreased due to the deposition of Ce^{4+} which has a larger atomic radius than Zr^{4+} or Mg^{2+} , on the pore walls. It can be inferred that pore structure is more ordered since the characteristic peaks of SBA-15 are more distinct in Mg^{2+} and Ce^{2+} containing materials compared to Ni@Zr-SBA-15. More ordered structure of these catalysts were probably caused by the change of acidity of the synthesis mixture. It is known that the acidity of the synthesis solution of SBA-15 is a very important factor for the development of its hexagonal porous structure regularity [42]. When Mg^{2+} and Ce^{4+} were incorporated, besides Zr^{4+} , they prevented the acidity decrease caused by Zr^{2+} . Absence of reflection peaks of d_{100} in the XRD pattern of MCM-41 type catalyst is due to the poorly developed ordered porous structure caused by high zirconia incorporation (Table 5).

Peaks present at 44.4° and 51.7° in all XRD patterns in Figure 23 indicated the presence of metallic nickel (Ni^0) with an average crystal size of 22.9, 10.4, 21.2 and 17 nm in Ni@Zr-SBA-15, Ni@Ce-Zr-SBA-15, Ni@Mg-Zr-SBA-15 and Ni@Zr-MCM-41 catalysts, respectively (Table 6). It indicates that Ce^{2+} incorporation increased the dispersion of nickel particles due to the strong interaction of ceria with nickel. The absence of additional Zr^{4+} , Ce^{2+} or Mg^{2+} reflections in the wide angle patterns of the catalysts suggest the formation of amorphous structure with very fine and dispersed metal oxide nanoparticles.

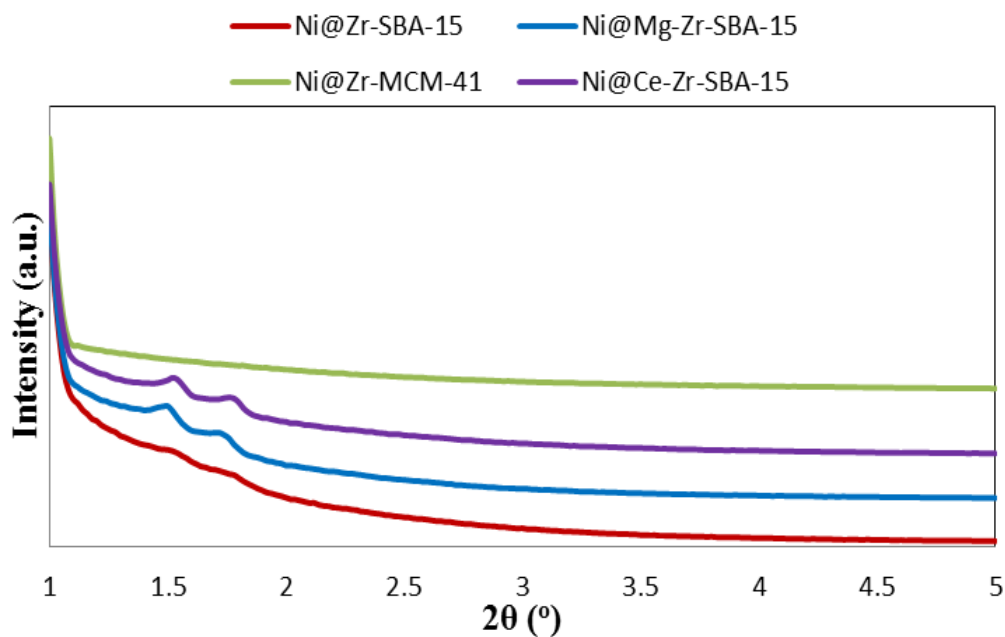


Figure 22: Low angle XRD patterns of Ni@Zr-SBA-15, Ni@Mg-Zr-SBA-15, Ni@Ce-Zr-SBA-15 and Ni@Zr-MCM-41.

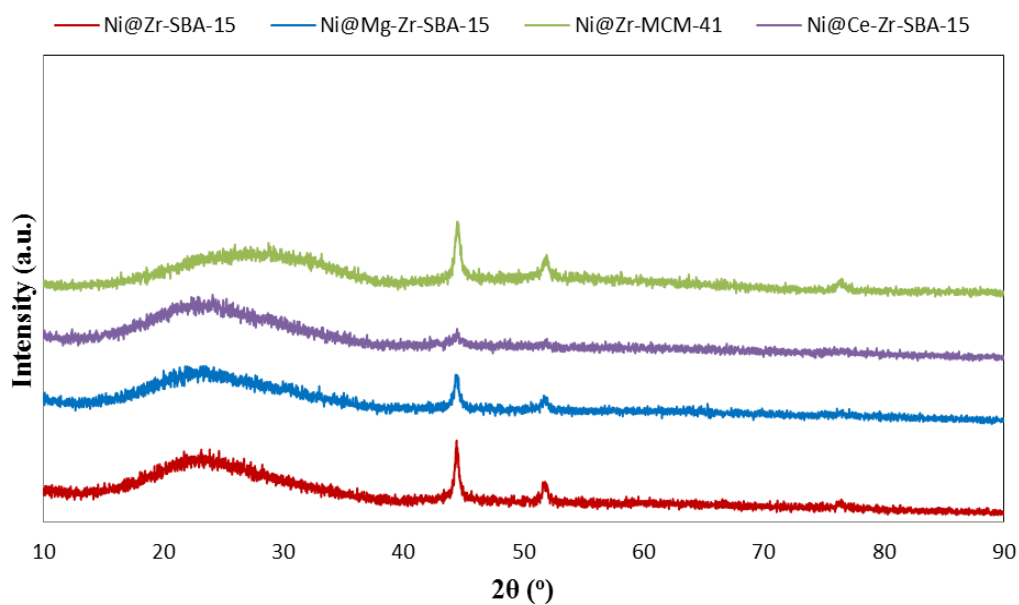


Figure 23: Wide angle XRD patterns of Ni@Zr-SBA-15, Ni@Mg-Zr-SBA-15, Ni@Ce-Zr-SBA-15 and Ni@Zr-MCM-41.

The nature of the acid sites of the catalysts was analyzed with DRIFTS of pyridine adsorbed samples (Figure 24). The presence of Lewis acid sites on all catalysts were observed with adsorption bands located at 1450, 1490 and 1609 cm^{-1} . Brönsted type acid sites, which should be observed at 1540 cm^{-1} , were not observed on any of the synthesized catalysts [73]. Lewis acid strengths of the catalysts were found to change in the following order; $\text{Ni@ZrO}_2 > \text{Ni@Zr-MCM-41} > \text{Ni@Zr-SBA-15} \sim \text{Ni@Ce-Zr-SBA-15} \sim \text{Ni@Mg-Zr-SBA-15}$. Pure zirconia supported catalyst possesses the highest number of acidic sites, as expected and Mg^{2+} or Ce^{4+} incorporation decreased the acidity of Zr-SBA-15.

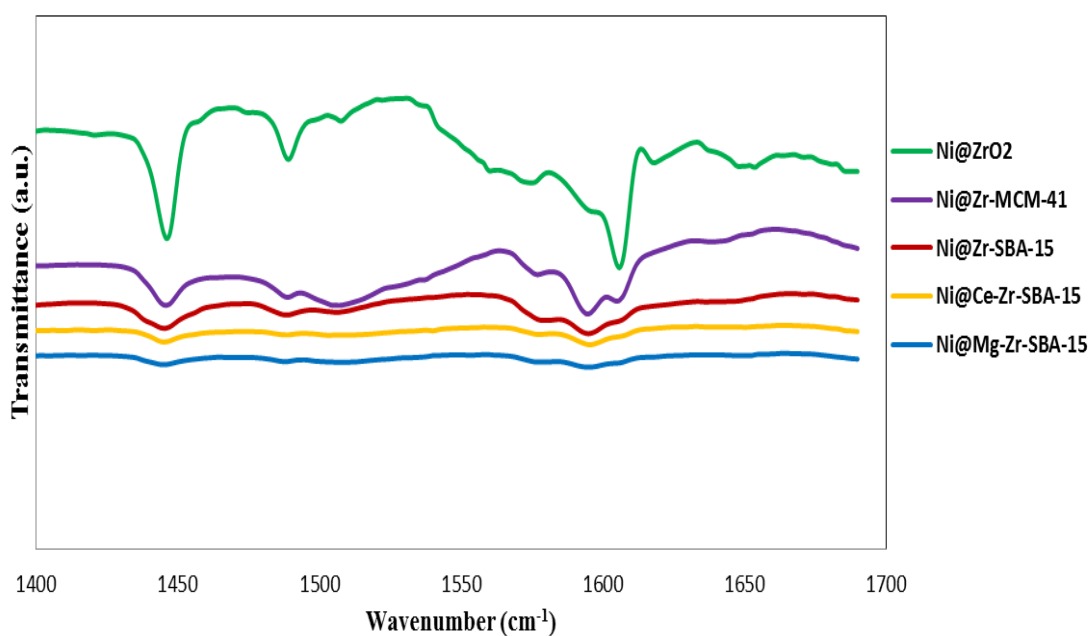


Figure 24: Pyridine adsorbed DRIFT spectra of Ni impregnated zirconia based catalysts.

6.2 CHARACTERIZATION RESULTS OF CeO₂/ZrO₂ SUPPORTED CATALYSTS

Physicochemical properties of the synthesized CeO₂/ZrO₂ support materials are presented in Table 7. As it can be seen that, as the ZrO₂ content of the material increases, surface area and pore volume decreases. Only CeO₂-ZrO₂ (2:1) material does not apply to this pattern with its surface area which is slightly lower than the expected value. All of the materials have mesoporous structure with pore diameters larger than 2 nm. Physicochemical properties of the nickel impregnated CeO₂/ZrO₂ supported catalysts are given in Table 8. Effect of nickel impregnation can be clearly seen when the surface areas and pore volumes on Table 7 and Table 8 are compared. Nickel dispersed over the surface of the material and plugged some of the pores in the structure.

It can be clearly seen from catalyst properties that calcination and reduction temperature significantly affected the surface area and crystal size calculated using Scherrer equation from XRD data (Figure 29) of CeO₂-ZrO₂ solid solution on Ni@CeO₂-ZrO₂ (6:1) catalysts. CeO₂ is known to lose its structural properties at high temperatures due to crystal growth and loss of surface area [55, 57]. Increase of calcination and reduction temperature decreased the surface area of the catalyst significantly due to enhanced crystal size of CeO₂-ZrO₂ solid solution which are presented in the following figures, as expected. Other than surface area, pore diameter also dropped to its half value when treatment temperature was increased above 500°C.

Table 7: Physicochemical properties of the CeO₂-ZrO₂ support materials

Material	S _{BET} (m ² /g)	V _P (cm ³ /g)	D _P (nm)
CeO ₂ -ZrO ₂ (6:1)	137	0.16	3.8
CeO ₂ -ZrO ₂ (4:1)	110	0.11	3.8
CeO ₂ -ZrO ₂ (2:1)	88	0.10	3.8
CeO ₂ -ZrO ₂ (1:1)	95	0.07	2.0
CeO ₂	193	0.24	3.8

Table 8: Physicochemical properties of the CeO₂-ZrO₂ supported catalysts.

Catalyst	Calc&Red T (°C)	S _{BET} (m ² /g)	V _P (cm ³ /g)	D _P (nm)	CeO ₂ -ZrO _{2ss} crystal size
Ni@CeO ₂ -ZrO ₂ (6:1)	400	82.8	0.09	3.8	4.2
Ni@CeO ₂ -ZrO ₂ (6:1)	450	61.0	0.10	3.8	4.9
Ni@CeO ₂ -ZrO ₂ (6:1)	500	16.4	0.07	3.8	7.1
Ni@CeO ₂ -ZrO ₂ (6:1)	550	11.9	0.08	1.9	9.1
Ni@CeO ₂ -ZrO ₂ (6:1)	600	31.7	0.12	1.9	9.2
Ni@CeO ₂ -ZrO ₂ (6:1)	650	12.8	0.04	1.6	13.0
Ni@CeO ₂ -ZrO ₂ (4:1)	450	29.2	0.08	4.2	5.6
Ni@CeO ₂ -ZrO ₂ (2:1)	450	65.2	0.09	3.4	5.0
Ni@CeO ₂ -ZrO ₂ (1:1)	450	60.0	0.05	3.8	3.8
Ni@CeO ₂	450	119	0.16	3.8	6.9

N₂ adsorption/desorption isotherms of Ni@CeO₂-ZrO₂ (6:1) catalyst with different calcination and reduction temperatures are presented in Figure 25. The isotherms of the catalysts treated at 400°C and 450°C shows Type IV isotherm indicating mesoporous structure. Hysteresis loops of these materials can be classified as type H2 loops which is associated with not well-defined pore size and shape distribution. When treatment temperature is increased, mesoporous structure of the material collapsed due to increase of crystal size of CeO₂-ZrO₂ solid solution (Table 8). Loss of the structure due to increased temperature can also be observed from pore size distribution data (Figure 26). While materials calcined and reduced at 400°C and 450°C gave a well-defined pore structure with maxima at 3.8 nm, other materials were lack of this structure.

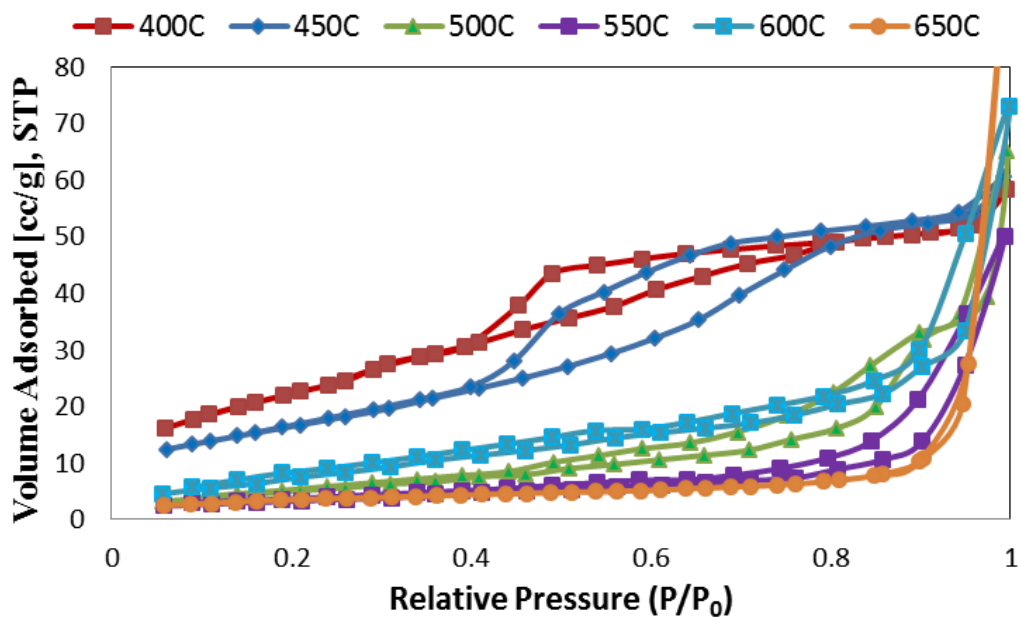


Figure 25: N₂ adsorption/desorption isotherms of Ni@CeO₂-ZrO₂(6:1) calcined and reduced at different temperatures.

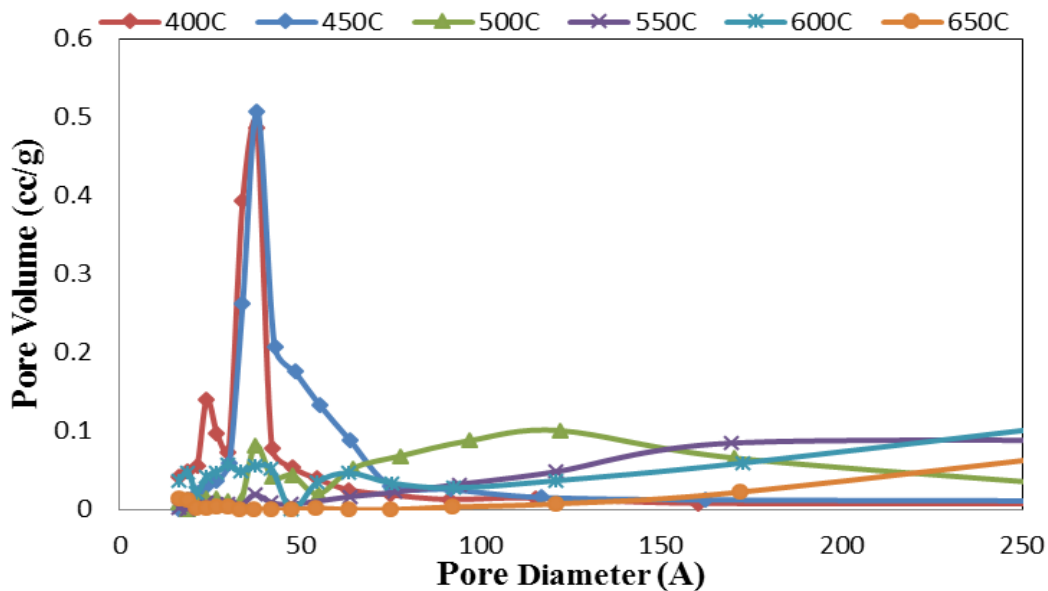


Figure 26: Pore size distributions of Ni@CeO₂-ZrO₂(6:1) calcined and reduced at different temperatures.

Ni@CeO₂ and Ni@CeO₂-ZrO₂ catalysts with CeO₂/ZrO₂ ratio of 2, 4 and 6 indicated the presence of Type IV N₂ adsorption isotherms and H2 type hysteresis loop (Figure 27). Higher pore volume of Ni@CeO₂ catalyst compared to Ni@CeO₂-ZrO₂ catalysts can be clearly seen from the isotherms. However, Ni@CeO₂-ZrO₂ catalysts with CeO₂/ZrO₂ ratio of 1 showed H4 type hysteresis loop which means that high ZrO₂ content of the catalyst prevented the formation of the mesoporous structure during synthesis of the material. Ni@CeO₂-ZrO₂ (4:1) catalyst do not possess a uniform pore size distribution resulting in higher pore volume (Figure 28, Table 8) compared to other catalysts.

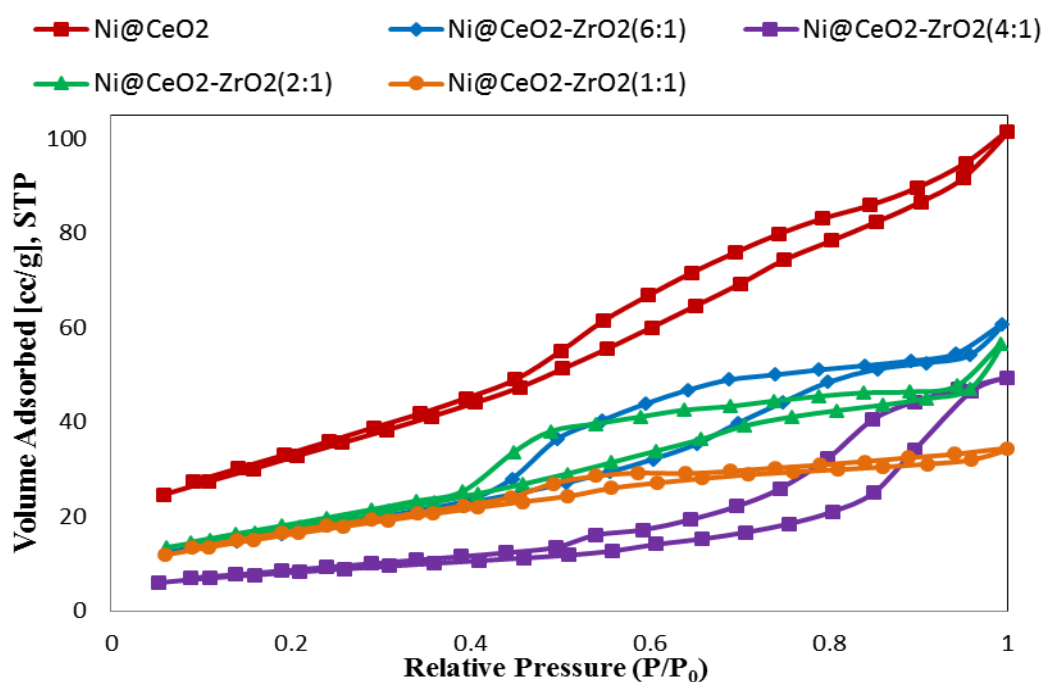


Figure 27: N₂ adsorption/desorption isotherms of Ni@CeO₂-ZrO₂ catalysts containing different CeO₂/ZrO₂ ratios calcined and reduced at 450°C

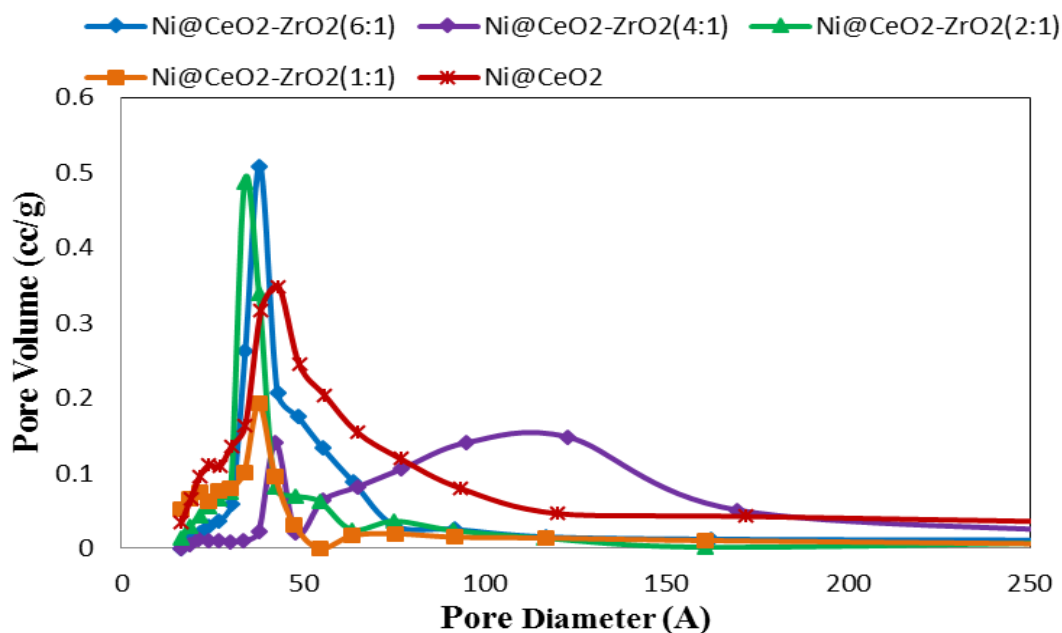


Figure 28: N₂ adsorption/desorption isotherms of Ni@CeO₂-ZrO₂ catalysts containing different CeO₂/ZrO₂ ratios calcined and reduced at 450°C.

XRD patterns of the synthesized catalysts at different calcination and reduction temperatures and with different CeO₂/ZrO₂ ratios are presented in Figure 29 and Figure 30, respectively. It has been reported by Trovarelli et al. [74] that for CeO₂-ZrO₂ material, monoclinic, tetragonal or cubic phases can be obtained and high CeO₂ loading generally cause cubic phase formation. Phase of the material, homogeneity of that phase and also CeO₂-ZrO₂ solid solution particle size has a strong effect on the redox behavior and reducibility of the catalyst affecting the presence of Ni⁰ on the catalyst surface [59]. Studies showed that cubic phase of CeO₂-ZrO₂ material with a CeO₂/ZrO₂ ratio of 4 has higher reducibility and possess stronger capability towards redox coupling between Ce³⁺ and Ce⁴⁺ [74, 75]. The patterns of Ni@CeO₂-ZrO₂ (6:1) solid solutions indicate the presence of cubic fluorite structure with reflections at 28.7°, 33.2°, 47.7° and 56.6° corresponding to (111), (200), (220) and (222) crystal planes, respectively. Presence of other phases; CeO₂ or ZrO₂ were not observed meaning that Ce and Zr ions were homogeneously mixed. Loss of material structure observed from pore size distributions due to crystal growth can be clearly observed from X-ray

diffraction data of catalysts. Peaks became more distinct and narrower with increasing temperature. Scherrer equation revealed that crystal size increased more than 200% when temperature increased from 400°C to 650°C. Nickel presence only observed with catalyst calcined and reduced at 600°C and 650°C at 59.5° corresponding to NiO (220) crystal plane and crystal size of NiO calculated using Scherrer equation was found as 7 nm and 9.1 nm, respectively. Absence of Ni⁰ at all temperatures and absence of NiO on the materials calcined and reduced below 600°C indicates that Ni⁰ and NiO was well dispersed and particles size were very small (< 7 nm) in catalysts treated below 600°C.

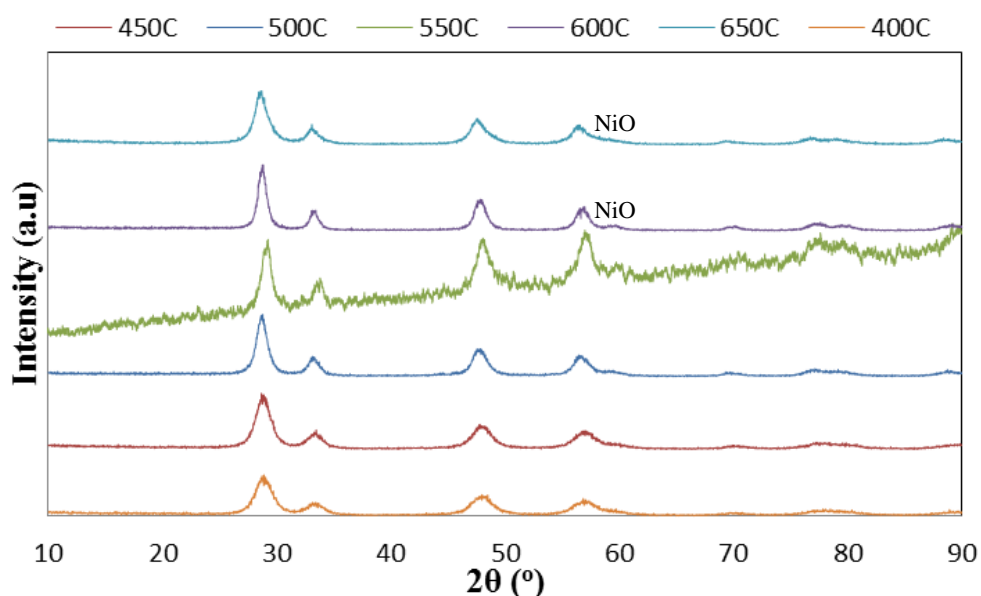


Figure 29: X-ray diffraction patterns of Ni@CeO₂-ZrO₂ (6:1) calcined and reduced at different temperatures.

The XRD patterns Ni@CeO₂-ZrO₂ catalysts containing different CeO₂/ZrO₂ ratios shown in Figure 30 presents true mixed oxide phase at high CeO₂/ZrO₂ ratios whereas, when ZrO₂ content becomes equal to CeO₂, solid solution phase peaks were no longer showed a homogeneous structure. Pure CeO₂ supported catalyst presented fluorite structure with peaks positioned at 28.5°, 33°, 47.4° and 56.4°. Increase of ZrO₂ content in the catalysts shifted XRD peaks towards higher angles due to insertion of

Zr⁴⁺ ions in the lattice of CeO₂ causing shrinkage of the lattice since Zr⁴⁺ ions has smaller radius (0.086 nm) compared to Ce⁴⁺ (0.097 nm). When CeO₂/ZrO₂ ratio increased to one, two combined peak of CeO₂ fluorite structure and tetragonal ZrO₂ structure was observed meaning that mixed oxide phase cannot be obtained with this ratio by following glycothermal reduction method.

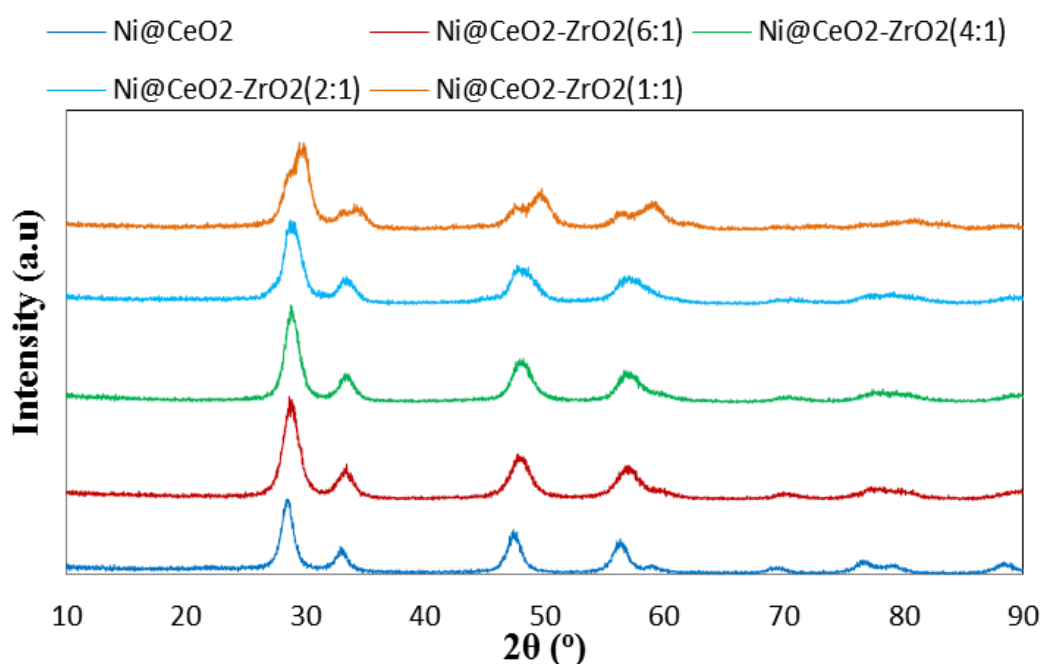


Figure 30: X-ray diffraction patterns of Ni@CeO₂-ZrO₂ catalysts containing different CeO₂/ZrO₂ ratios calcined and reduced at 450°C

The surface composition of Ni@CeO₂-ZrO₂ (6:1) catalyst calcined and reduced at 450°C were analyzed with X-ray photoelectron spectra analysis. Obtained XPS spectra were corrected for charge shifting using the standard C1s binding energy of 284.4 eV and curve fitting was conducted by using XPSPeak 4.1 software package. In the software, Shirley type background fitting and 80% Lorentzian combination peaks were used for determination of spectra baselines and deconvolution, respectively. XPS

spectra of Ce3d region which is composed of 6 peaks can be seen from Figure 31. Curves of Ce 3d spectra were labeled as u and v referring to $3d_{3/2}$ and $3d_{5/2}$ spin-orbit components, respectively. The peaks were labeled on Figure 31 as u^{II} , u^I , u , v^{III} , v^{II} , v^I and v were observed at 907.13 eV, 901.76 eV, 900.15 eV, 898.02 eV, 888.33 eV, 884.43 eV and 882.19 eV. u^{II} and u arise from $Ce^{4+} 3d_{3/2}$, v , v^{II} and v^{III} corresponds to $Ce^{4+} 3d_{5/2}$ and the couples labeled as u^I and v^I represent Ce^{3+} . The relative percentages of cerium species were calculated using the area ratios of the Ce^{4+} and Ce^{3+} ($Ce^{4+} 3d_{5/2}$ (v , v^{II} and v^{III}) / $Ce^{3+} 3d_{5/2}$ (v^I)). It was found that while Ce^{4+} possess 77.6%. About 22.4% of the material surface is composed of Ce^{3+} which was associated with the formation of oxygen vacancies on the material and related with the lattice parameter and reducibility of the material [76, 77].

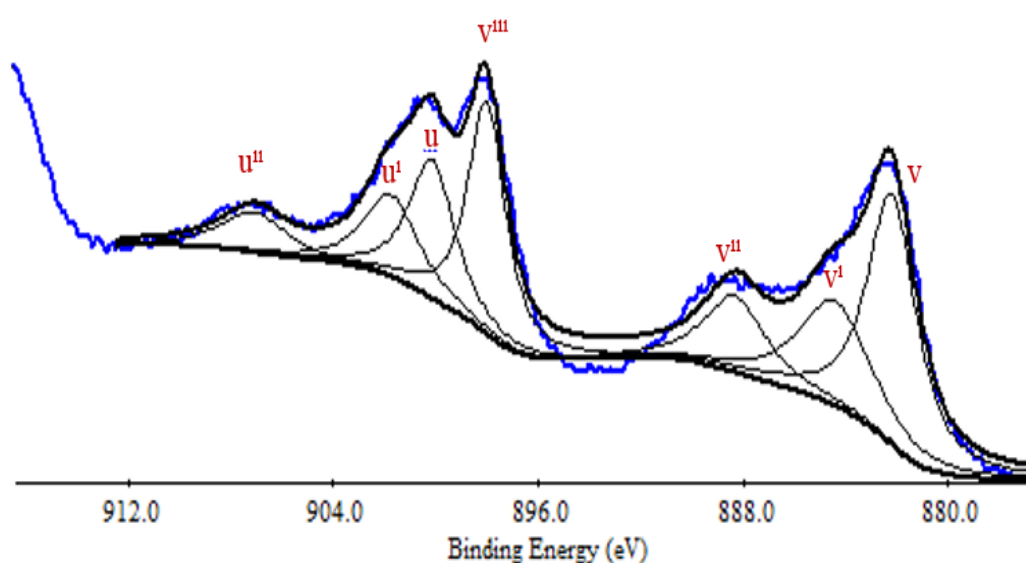


Figure 31: Ce (3d) XPS spectra for of Ni@CeO₂-ZrO₂ (6:1) catalyst calcined and reduced at 450°C

Figure 32 shows the Ni2d XPS spectra for of Ni@CeO₂-ZrO₂ (6:1) catalyst, calcined and reduced at 450°C. Peaks at 851.94 and 856.69 corresponds to metallic nickel and peaks at 854.79 and 861.32 corresponds to NiO [78]. It can be seen that

area of NiO peaks are higher compared to metallic nickel peaks indicating the dominance of NiO on the surface of the material. It can be inferred that NiO was not reduced completely due to low temperature reduction, 450°C, in the presence of CeO₂ which has a strong interaction with nickel clusters [60]. XPS spectra of Zr3d region which is composed of 2 peaks which can be seen from Figure 33. The peak seen at 181.58 corresponds to Zr3d_{3/2} (Zr⁰) and the one observed at 183.8 is accepted as Zr3d_{5/2} (ZrO₂) [79]. Zr⁰ possess slightly larger peak area compared to ZrO₂ indicating higher reducibility of zirconia compared to NiO.

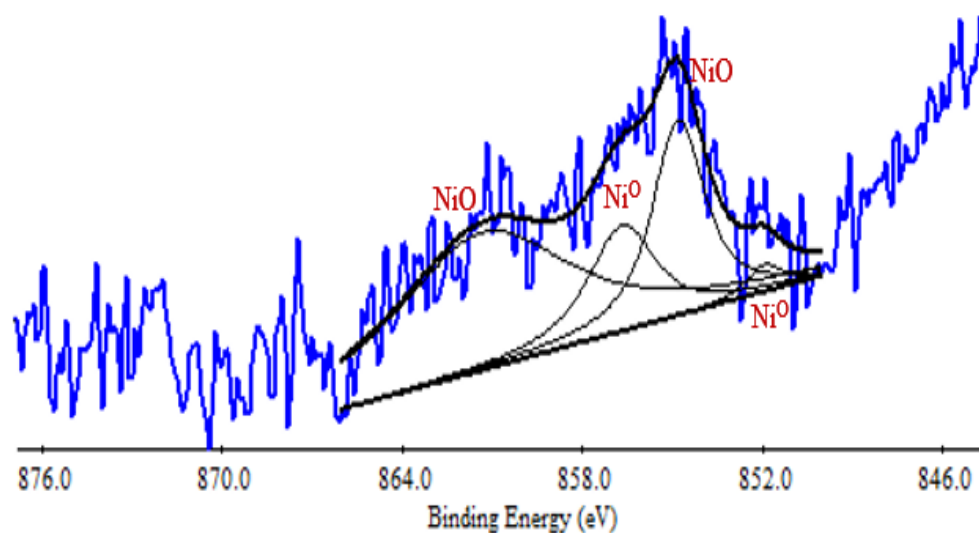


Figure 32: Ni (2d) XPS spectra for of Ni@CeO₂-ZrO₂ (6:1) catalyst calcined and reduced at 450°C

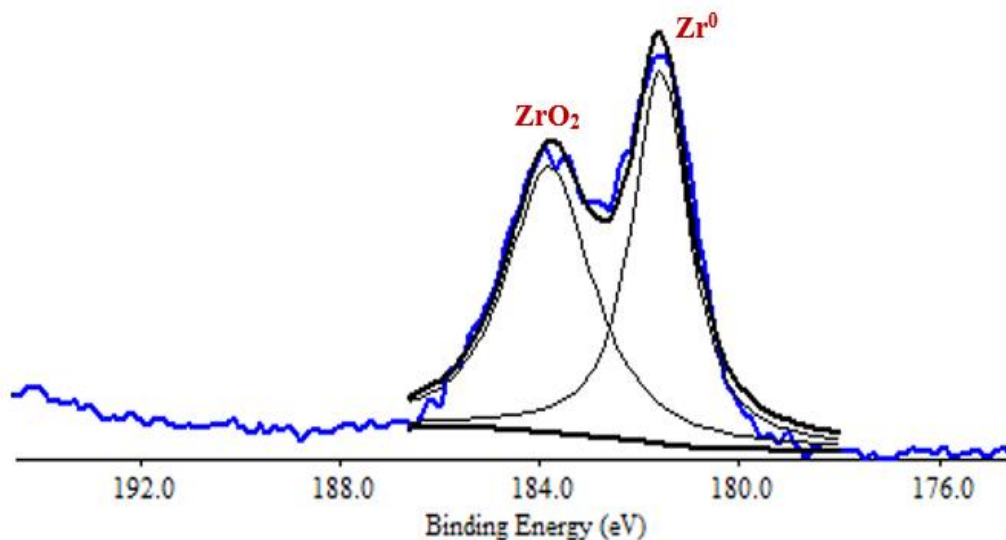


Figure 33: Zr (3d) XPS spectra for of Ni@CeO₂-ZrO₂ (6:1) catalyst calcined and reduced at 450°C

6.3 ACTIVITY RESULTS OF ZIRCONIA INCORPORATED MESOPOROUS CATALYSTS IN ETHANOL STEAM REFORMING PROCESS

Catalytic activities of the zirconia incorporated catalysts; Ni@Zr-SBA-15, Ni@Ce-Zr-SBA-15, Ni@Mg-Zr-SBA-15, Ni@Zr-MCM-41 and Ni@ZrO₂ were tested at the reaction temperatures of 550°C and 600°C and at the H₂O/EtOH ratios of 3.2, 4 and 5 in ethanol steam reforming reaction and the average results obtained within 5 h time-on- stream tests are reported in Table 9, in terms of hydrogen yield, product distribution. Carbon accumulations on the catalysts obtained from thermal analysis after 5 h time on stream were also presented in terms of mg C/g_{cat}.h. Details of carbon deposition are discussed in Section 6.5. Zirconia supported catalysts found to be very active towards ethanol steam reforming reaction, resulting in complete conversion of ethanol at all temperatures and H₂O/EtOH ratios. Activity tests resulted hydrogen yield values in the range of 3.2-5.8 per mole of EtOH reacted, which are 53-97% of the maximum possible yield value of 6 (R.2). Formation of H₂, CO, CO₂, CH₄ at all temperatures and small amount of ethylene at 550°C were observed at the activity tests.

Methane and ethylene are produced via ethanol decomposition (R.10) and ethanol dehydration (R.9), respectively.

Table 9: Activity data for ethanol steam reforming of zirconia incorporated catalysts at different temperatures and water-to-ethanol ratios. (Average of 5 h).

Catalyst	T (°C)	H ₂ O/EtOH (mol/mol)	H ₂ yield	H ₂ %	CO%	CH ₄ %	CO ₂ %	C ₂ H ₄ %	mg C /g _{cat} ·h
Ni@ZrO ₂	550	3.2	4.19	67.2	5.0	7.1	20.4	0.3	60
	600	3.2	4.42	68.9	9.0	4.6	17.3	0.2	58
Ni@Zr-SBA-15	550	3.2	4.84	71.6	3.6	6.0	17.0	1.8	152
	600	3.2	4.90	71.1	8.0	3.5	17.4	0	88
		4.0	5.10	71.7	6.4	2.8	19.0	0	76
		5.0	5.00	71.4	5.8	2.7	20.0	0.1	66
	650	3.2	5.59	73.5	11.8	1.3	13.4	0	75
Ni@Ce-Zr-SBA-15	550	3.2	3.2	62.6	2.6	2.7	15.3	16.8	123
	600	3.2	4.25	68.7	6.9	2.7	14.9	6.8	115
Ni@Mg-Zr-SBA-15	550	3.2	4.25	70.4	3.5	3.6	16.7	5.8	146
	600	3.2	5.54	73.5	7.7	3.1	15.7	0	138
		4.0	5.82	74.3	5.3	2.1	18.3	0	132
		5.0	5.59	73.6	4.3	2.0	20.1	0	90
Ni@Zr-MCM-41	550	3.2	3.88	69.1	2.4	5.9	18.2	5.0	102
	600	3.2	5.40	72.6	6.5	4.5	16.4	0	104

Reaction temperature of 550°C is high enough to achieve desired catalyst activity in ethanol steam reforming reaction thermodynamically. However, it is a critical temperature in this study for coking and possible catalyst deactivation, since acidic sites of zirconia catalysts cause formation of high amounts of coke. In order to reach stable catalytic performance, gasification of carbon from the surface of the catalyst is required. Therefore, activity tests were also performed at 600°C which can increase carbon gasification. As it can be seen from the Table 9, increase of temperature leads to enhancement of hydrogen production and reduction of carbon deposition. It was observed that activities of Ni@Zr-SBA-15, Ni@Ce-Zr-SBA-15,

Ni@Mg-Zr-SBA-15 and Ni@Zr-MCM-41 showed a decreasing trend with reaction time at 550°C. However, at 600°C catalysts showed more stable hydrogen production rates. Reaction temperature also raised to 650°C for Ni@Zr-SBA-15 catalyst to facilitate carbon gasification and increase in hydrogen productivity with a decrease in coke formation rate was observed (Figure 34). Hydrogen yield was found at 650°C as 5.59 which correspond to 93% of the maximum possible value of 6. Increase of temperature also decreased the amount of methane in the product stream, due to higher rate of methane gasification at higher temperatures. Product distributions with respect to time of Ni@Zr-SBA-15 catalyst at 550°C, 600°C and 650°C are given in Figure 35, Figure 36 and Figure 37, respectively. It can be seen that CH₄ formation decreased with increasing reaction temperature due to enhanced methane reforming reaction (R. 19) which requires high temperatures. Enhanced CO production also caused by this reaction and diminished water gas shift reaction (R. 4).

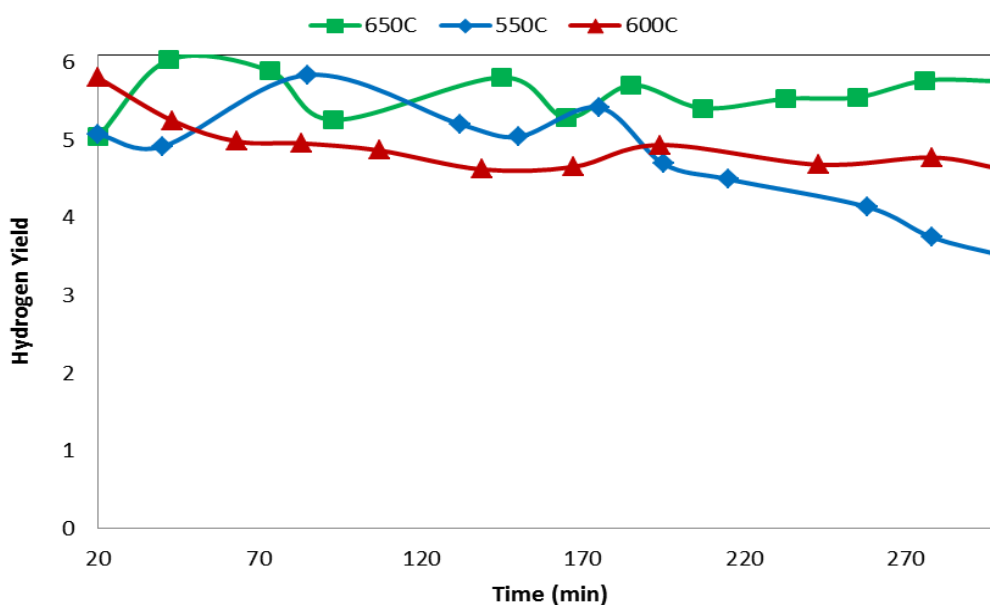


Figure 34: Hydrogen yield observed at 550°C, 600°C and 650°C on Ni@Zr-SBA-15.

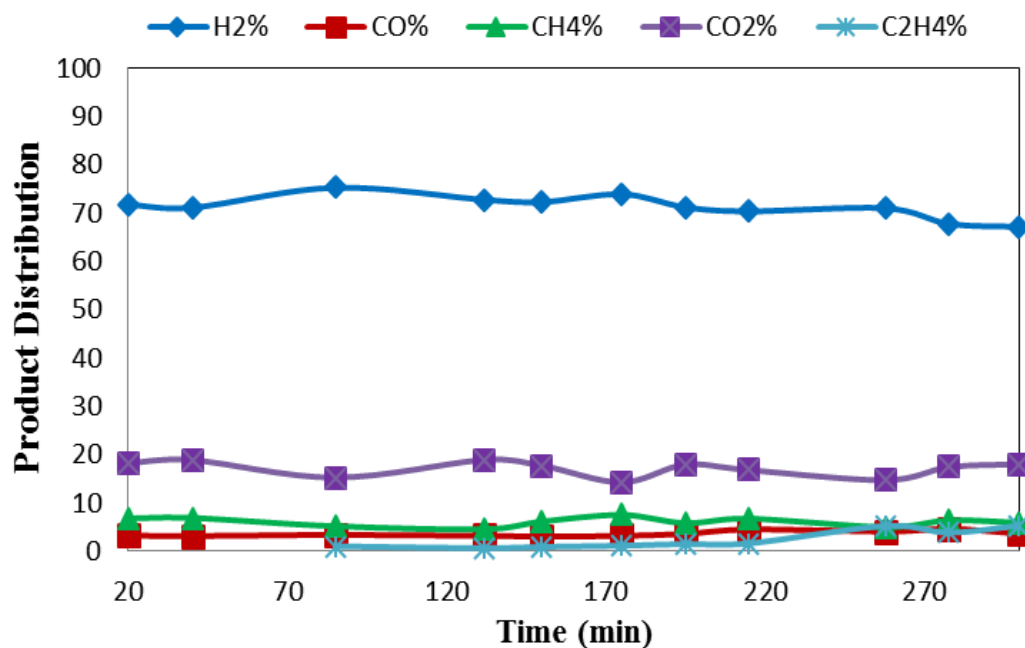


Figure 35: Product distribution of Ni@Zr-SBA-15 catalyst at 550°C.

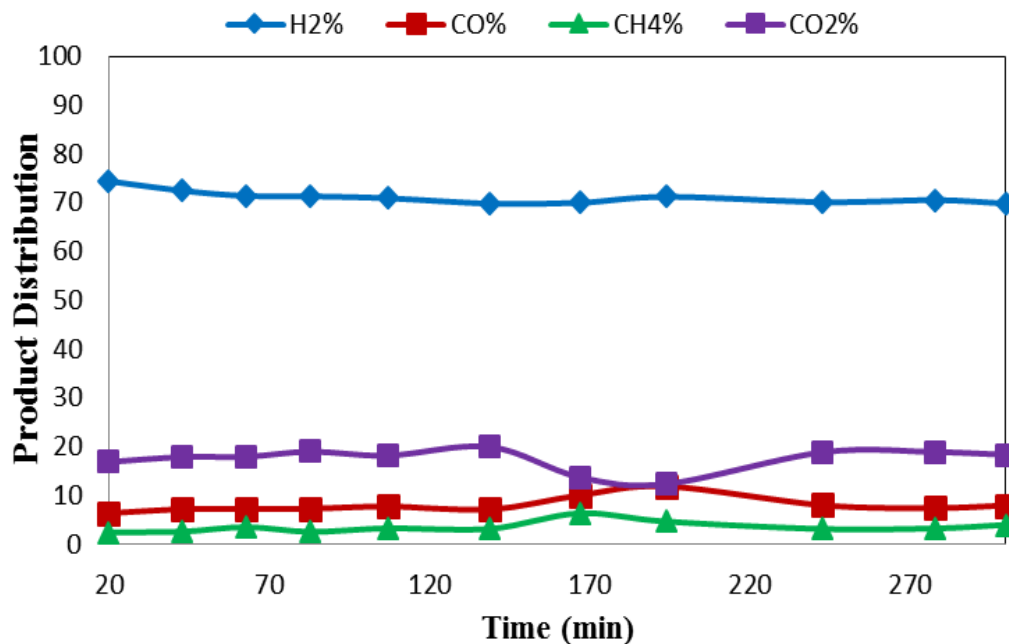


Figure 36: Product distribution of Ni@Zr-SBA-15 catalyst at 600°C.

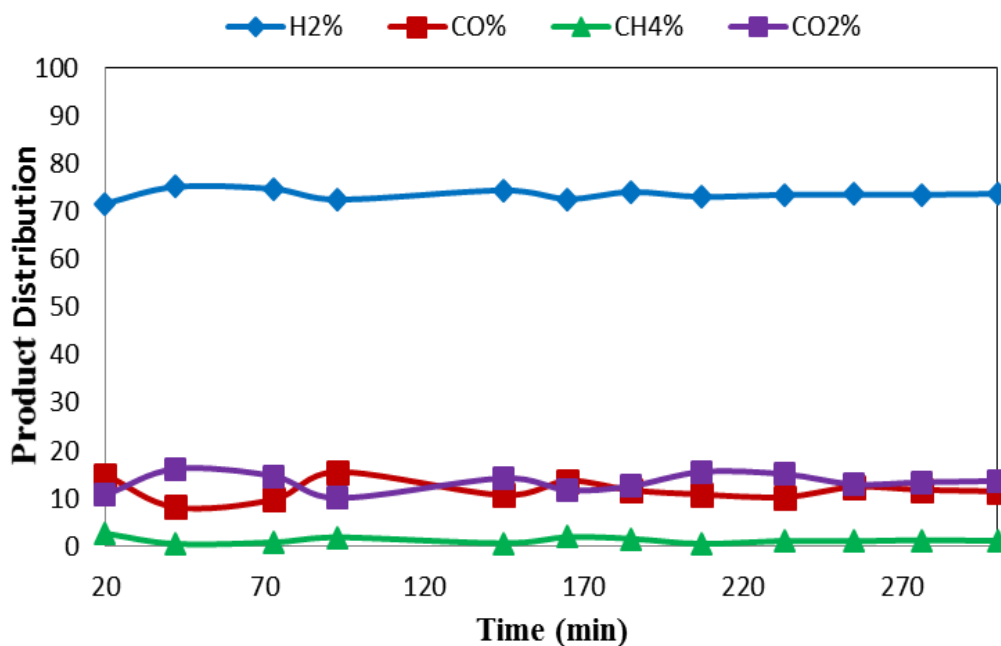


Figure 37: Product distribution of Ni@Zr-SBA-15 catalyst at 650°C.

Mesoporous ZrO₂ supported catalyst (Ni@ZrO₂) showed reasonably good activity with relatively low coke formation, due to high metal dispersion and relatively lower nickel crystal size (15.2 nm). It can be seen in Table 9, that hydrogen production was slightly lower and methane formation was higher over Ni@ZrO₂, compared to the silica containing supports. When zirconia was incorporated to the silicate structure (Ni@Zr-SBA-15), hydrogen yield increased from 74% to 82% of the maximum possible value of 6 at 600°C. Higher catalytic activity of zirconia-silica based catalysts is due to the higher metal-support interfacial area, on which water can dissociate into reactive OH groups. Although higher catalytic activity was observed over Ni@Zr-SBA-15 as compared to Ni@ZrO₂, only about 31% of the added zirconia was successfully incorporated into the mesoporous framework of SBA-15 (Table 5). For this reason, another zirconia incorporated silica-based material; Zr-MCM-41 was synthesized at a high synthesis solution pH, which yielded excellent incorporation of zirconia into the MCM-41 framework. Successful incorporation of zirconia into the

MCM-41 framework lead to higher H₂ yield (time averaged) with poor stability due to excessive coke formation (Figure 38).

High rate of carbon deposition was believed to be caused by the acidic nature of zirconia-silica materials and Mg²⁺ was introduced to the structure of Zr-SBA-15 to decrease its acidity. Even though the incorporated amount of Mg²⁺ was low, DRIFTS analysis indicated that the acidic strength of the catalyst diminished. However, activity tests revealed higher coke formation rate, accompanying with a higher hydrogen yield over Ni@Mg-Zr-SBA-15, at 600°C. A Possible reason of this unexpected result is believed to be the limiting effect of Mg²⁺ towards the activation of carbon gasification by reducing water adsorption-dissociation capability of zirconia support. Ce⁴⁺ was incorporated into Zr-SBA-15 structure due to its high oxygen mobility and for improving zirconia catalysts properties such as thermal stability, metal dispersion and support-metal interaction. High acidity of Zr-SBA-15 material was decreased when it was synthesized with ceria according to DRIFTS analysis (Figure 24). Lower acidity and improved properties of Ni@Ce-Zr-SBA-15 resulted in very unstable activity in ethanol steam reforming reaction. As it can be seen from Figure 38 and Figure 39, very high hydrogen production was observed at the initial hour of the test. However, after this time hydrogen production decreased significantly due to excessive coke formation. Product distribution with respect to time of Ni@Ce-Zr-SBA-15, Ni@Mg-Zr-SBA-15, Ni@Zr-MCM-41 and Ni@ZrO₂ catalysts are given in Figure 39, Figure 40, Figure 41 and Figure 42, respectively. Unstable nature of Ni@Ce-Zr-SBA-15 and Ni@Zr-MCM-41 compared to others can be clearly seen from the product distribution curves.

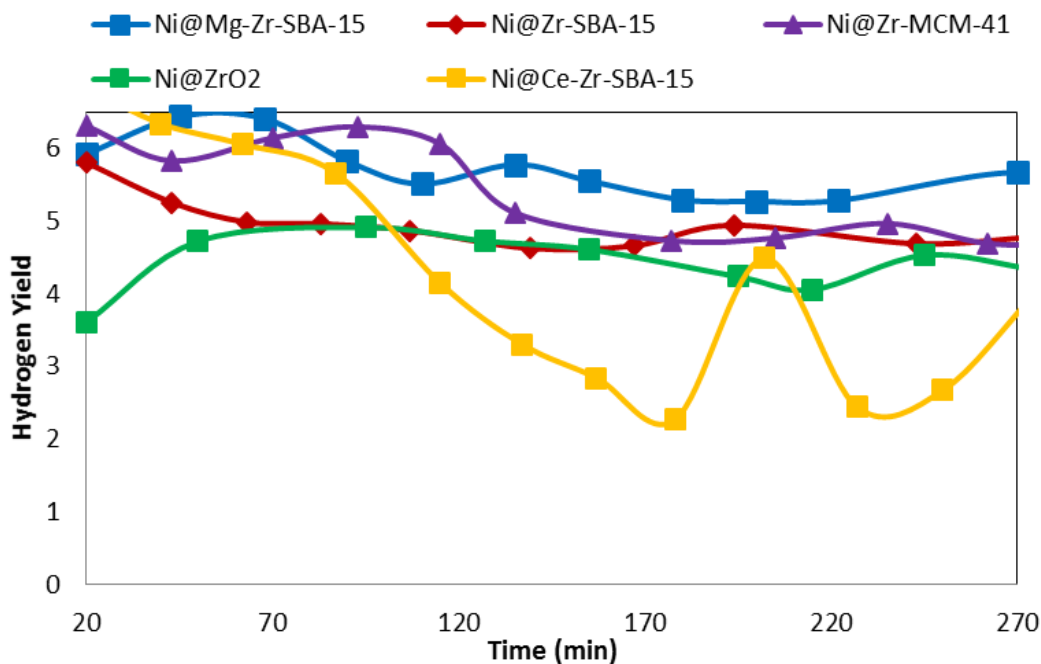


Figure 38: Hydrogen yields of Ni@Zr-SBA-15, Ni@Ce-Zr-SBA-15, Ni@Mg-Zr-SBA-15, Ni@Zr-MCM-41 and Ni@ZrO₂ catalysts at 600°C with a H₂O/EtOH ratio of 3.2.

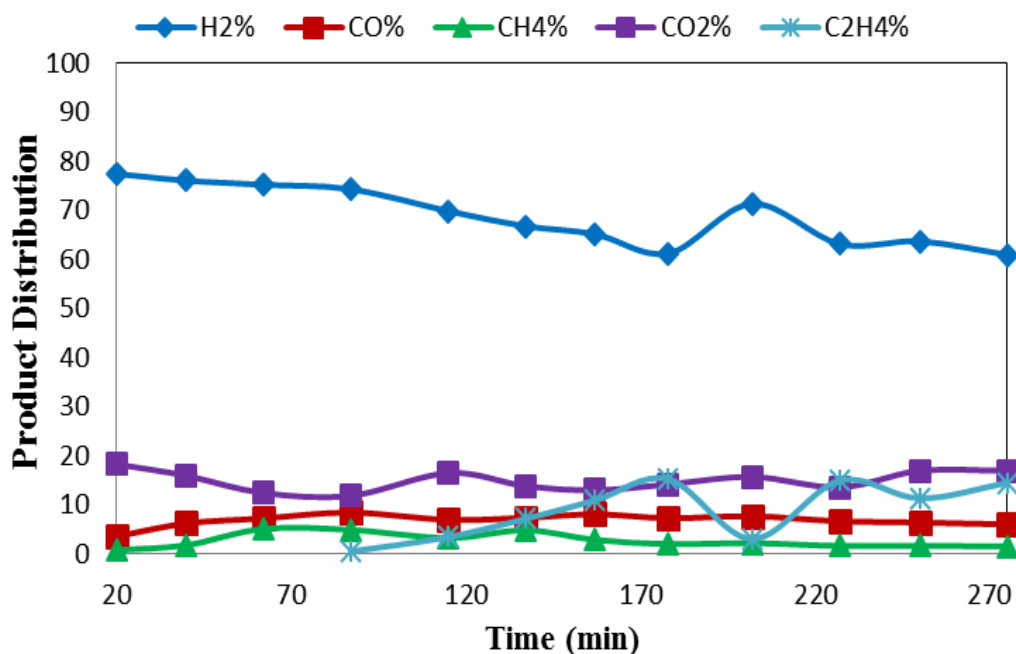


Figure 39: Product distribution of Ni@Ce-Zr-SBA-15 catalyst at 600°C with a H₂O/EtOH ratio of 3.2.

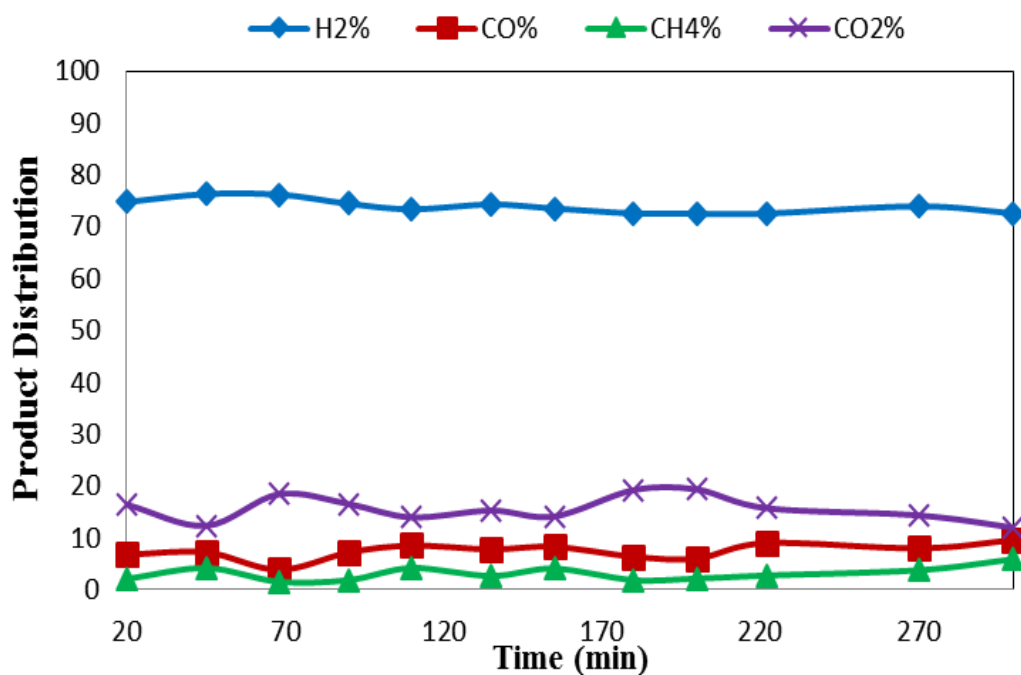


Figure 40: Product distribution of Ni@Mg-Zr-SBA-15 catalyst at 600°C with a H₂O/EtOH ratio of 3.2.

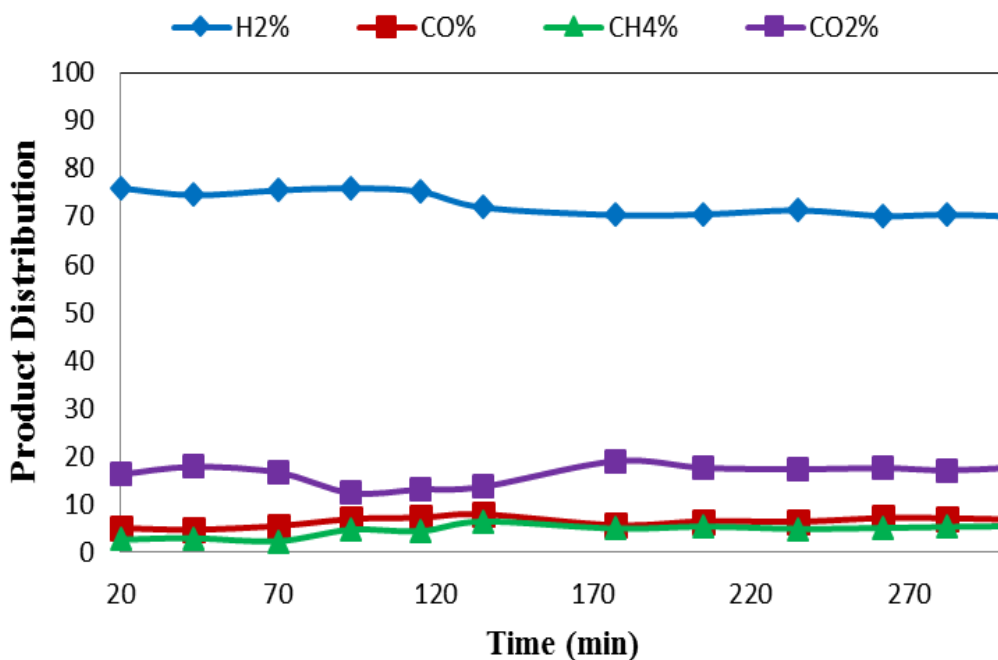


Figure 41: Product distribution of Ni@Zr-MCM-41 catalyst at 600°C with a H₂O/EtOH ratio of 3.2.

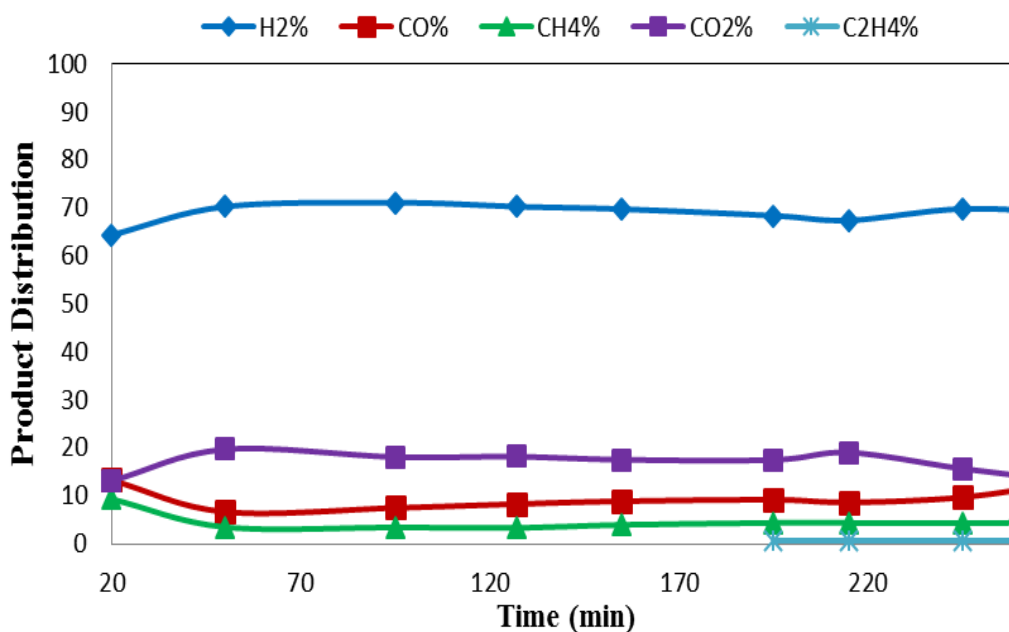


Figure 42: Product distribution of Ni@ZrO₂ catalyst at 600°C with a H₂O/EtOH ratio of 3.2.

A set of experiments were also performed with different H₂O/EtOH ratios over Ni@Zr-SBA-15 and Ni@Mg-Zr-SBA-15. Increase of this ratio from 3.2 to 5 resulted in a decrease of coke formation and CO/CO₂ ratio in the product stream (Table 9). While CO and CH₄ formation decreased, CO₂ production increased as a result of enhanced WGSR and diminished ethanol decomposition reaction rates. As shown in Figure 43 and Figure 44, increase of steam in the reaction zone enhanced catalytic stabilities of Ni@Zr-SBA-15 and Ni@Mg-Zr-SBA-15, respectively.

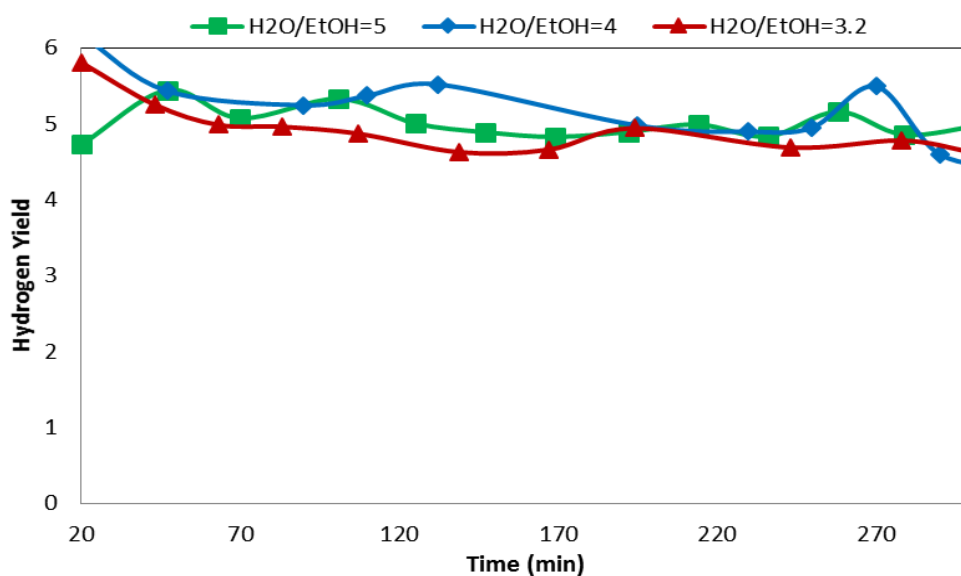


Figure 43: Hydrogen yields of Ni@Zr-SBA-15 at 600°C with H₂O/EtOH=3.2, 4 and 5.

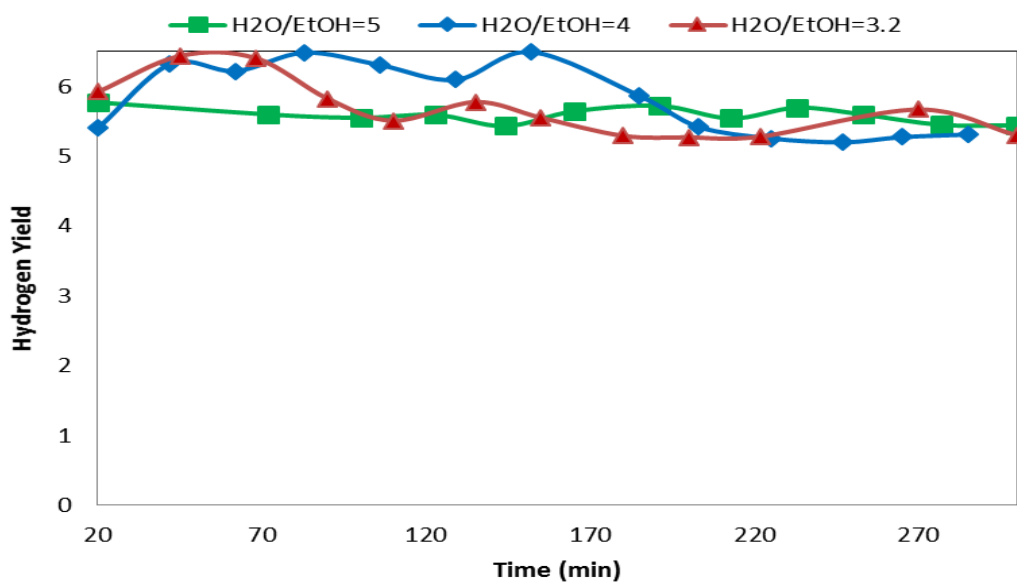


Figure 44: Hydrogen yields of Ni@Mg-Zr-SBA-15 at 600°C with H₂O/EtOH=3.2, 4 and 5.

6.4 ACTIVITY RESULTS OF CeO₂/ZrO₂ SUPPORTED CATALYSTS IN ETHANOL STEAM REFORMING PROCESS

Catalytic activity tests towards ethanol steam reforming of the CeO₂-ZrO₂ supported catalysts were performed between 450°C and 650°C for 5 h and average results are shown on Table 10 in terms of ethanol conversion, hydrogen formation per mole of ethanol and product distribution. Carbon depositions on the catalysts obtained from thermal analysis after 5 h time on stream were also presented in terms of mg C/g_{cat}.h. Details of carbon deposition are discussed in Section 6.6. Ni@CeO₂-ZrO₂ (6:1) catalyst found to be very active in ethanol steam reforming in the temperature range of 400-650°C. CeO₂ is known to be significantly affected by increase of crystal size and loss of surface area at high temperatures [57]. For this reason in the first set of experiments, all temperatures were investigated, starting from 400°C with an increment of 50°C, by keeping calcination and reduction temperatures the same as the reaction temperature. When catalytic activities are analyzed, increase of calcination, reduction and reaction temperatures from 400°C to 650°C gradually, resulted in enhancement of ethanol conversion due to endothermic nature of the ethanol steam reforming reaction (R. 2). However, hydrogen selectivity was higher at low temperatures, due to higher surface area and lower crystal size of Ni@CeO₂-ZrO₂ (6:1) catalysts treated at lower temperatures (Table 8). Besides, CeO₂ is more active at low temperatures towards water gas shift reaction (R.4) with its high surface mobility of OH groups, enhancing hydrogen production via overall steam reforming reaction (R.2). Hydrogen formation per mol of ethanol reacted at 450°C was found as 5.15 corresponding to 86% of the maximum possible value of 6. Carbon deposition on these catalysts were maximum at 500°C and 550°C. Coke formation through Boudouard reaction is highly active at low temperatures. At 400°C and 450 °C, high amounts of carbon deposition was avoided due to the small crystal sizes of the catalysts calcined and reduced at these temperatures. At 600°C and 650 °C, gasification of deposited carbon lead to low coke formation.

Table 10: Activity results towards ethanol steam reforming of CeO₂-ZrO₂ supported nickel catalysts

Catalyst	Calc&Red T (°C)	Rxn T (°C)	EtOH Conv. (%)	H ₂ formation/mol of EtOH (out of 6)	H ₂ %	CO %	CH ₄ %	CO ₂ %	Other %	mg C /g _{cat} .h
Ni@CeO ₂ -ZrO ₂ (6:1)	400	400	57.0	5.08	72.1	6.4	3.2	17.2	1.1*	4
Ni@CeO ₂ -ZrO ₂ (6:1)	450	450	80.0	5.15	72.0	6.8	3.4	17.8	0	6
Ni@CeO ₂ -ZrO ₂ (6:1)	500	500	82.4	3.76	65.2	4.9	9.9	20.0	0	90
Ni@CeO ₂ -ZrO ₂ (6:1)	550	550	89.3	3.98	66.5	6.6	7.7	19.2	0	56
Ni@CeO ₂ -ZrO ₂ (6:1)	600	600	100	4.59	69.6	7.3	4.2	19.0	0	12
Ni@CeO ₂ -ZrO ₂ (6:1)	650	650	100	4.75	70.3	11.6	2.3	15.8	0	8
Ni@CeO ₂ -ZrO ₂ (6:1)	650	450	94.5	3.28	61.7	4.5	15.1	18.7	0	68
Ni@CeO ₂ -ZrO ₂ (6:1)	650	550	96.3	3.74	65.0	9.0	8.7	17.3	0	48
Ni@CeO ₂ -ZrO ₂ (6:1)	650	600	100	4.60	69.5	10.5	3.9	16.1	0	48
Ni@CeO ₂ -ZrO ₂ (4:1)	450	450	100	5.43	73.0	8.8	5.1	13.1	0	60
Ni@CeO ₂ -ZrO ₂ (2:1)	450	450	82.1	4.09	68.1	5.5	5.3	19.1	2.0**	8
Ni@CeO ₂ -ZrO ₂ (1:1)	450	450	85.2	4.46	68.5	8.5	7.8	15.3	0	114
Ni@CeO ₂	450	450	100	2.2	51.6	1.9	24.8	21.6	0	12

* C₂H₄O for Ni@CeO₂-ZrO₂(6:1)(400°C) and Ni@CeO₂-ZrO₂ (5:1)

** C₂H₄ for Ni@CeO₂-ZrO₂ (2:1)

In the second set of experiments, calcination and reduction temperatures were fixed as 650°C in order to observe the effect of reaction temperature alone on the activity and stability of Ni@CeO₂-ZrO₂ (6:1) catalyst (Figure 45). In this case, reaction temperature was varied between 450-650°C. Decrease of reaction temperature lead to reduction in both ethanol conversion and hydrogen production. Moreover, water gas

shift reaction rate (R. 4) and ethanol cracking rate (R. 10, R. 11) were enhanced with decreasing temperature, as expected. This result showed that, decrease of reaction temperature to 450°C, by keeping calcination and reduction temperatures at a high value (650°C), is not beneficial in terms of hydrogen selectivity. Importance of calcination/reduction temperatures on the performance of this catalyst is clearly indicated by these results.

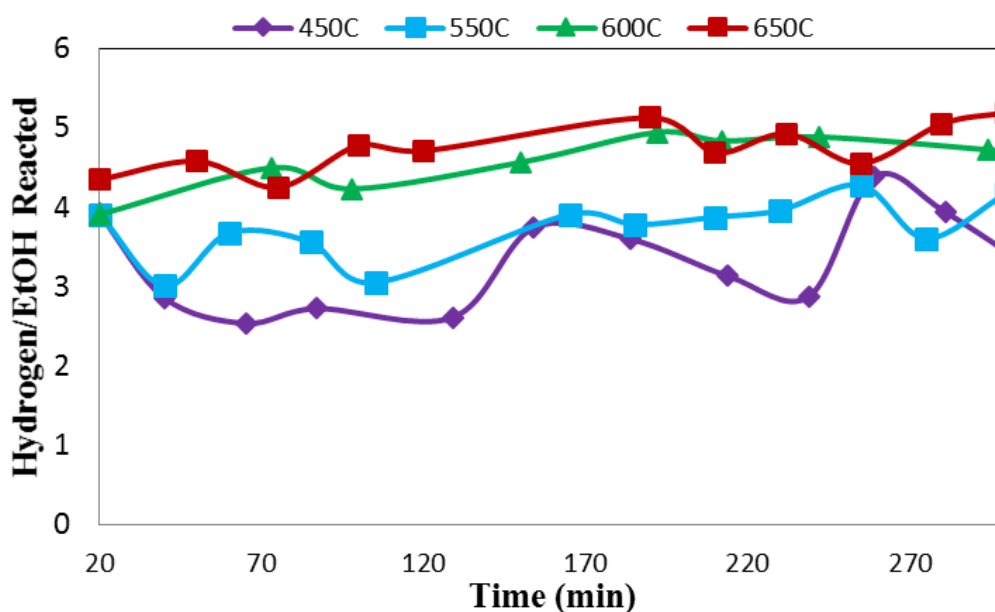


Figure 45: Comparison of hydrogen formation per mole of ethanol with Ni@CeO₂-ZrO₂ (6:1) calcined and reduced at 650°C at different reaction temperatures for SRE.

In order to observe the effect of calcination and reduction temperature alone, results obtained at a reaction temperature of 450°C with Ni@CeO₂-ZrO₂ (6:1), calcined/reduced at different temperatures, are compared in Figures 46-48. Figure 46 shows the hydrogen formation per mole of ethanol reacted over these catalysts. Product distributions were also given in Figure 47 and Figure 48. As it can be seen, the catalyst calcined and reduced at 450°C resulted in superior stability, and over 90% of the maximum possible hydrogen formation selectivity (of 6) per mole of ethanol was obtained. However, hydrogen selectivity on Ni@CeO₂-ZrO₂ (6:1), which was calcined and reduced at 650°C, could not even reach to 60% of the maximum possible value of 6. Also, methane formation carbon deposition was much higher with the

catalyst calcined and reduced at 650°C, due to higher crystal sizes of ceria and nickel (Table 10).

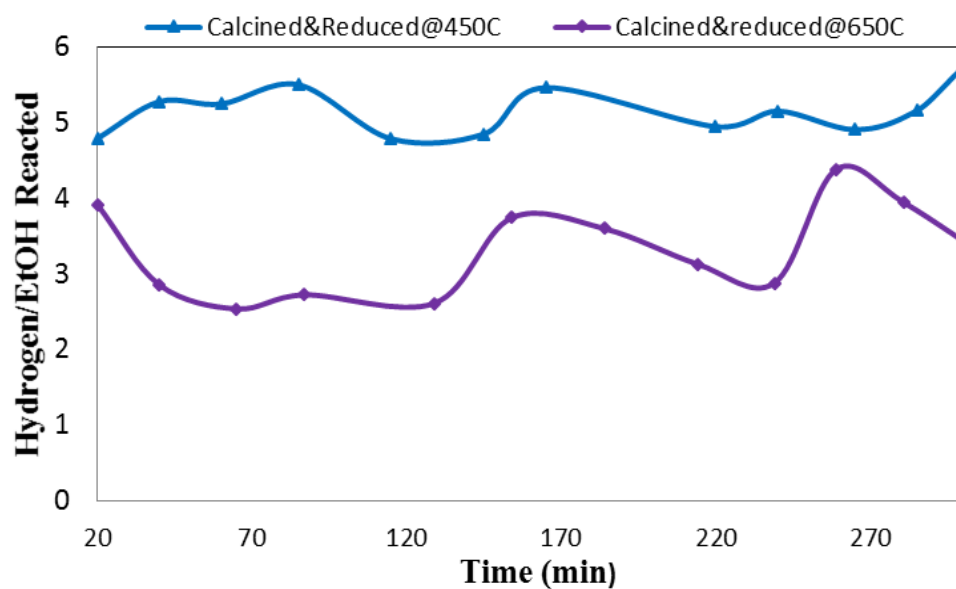


Figure 46: Comparison of hydrogen formation per mole of ethanol with Ni@CeO₂-ZrO₂ (6:1) calcined and reduced at 450°C and 650°C at a reaction temperature of 450°C for SRE.

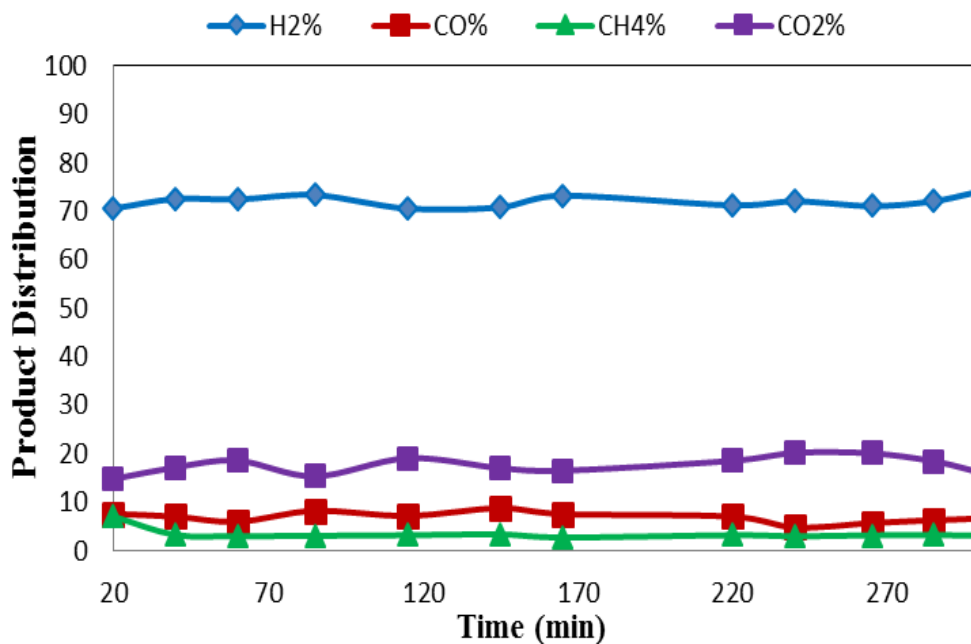


Figure 47: Product distribution at a reaction temperature of 450°C for SRE with Ni@CeO₂-ZrO₂ (6:1) calcined and reduced at 450°C

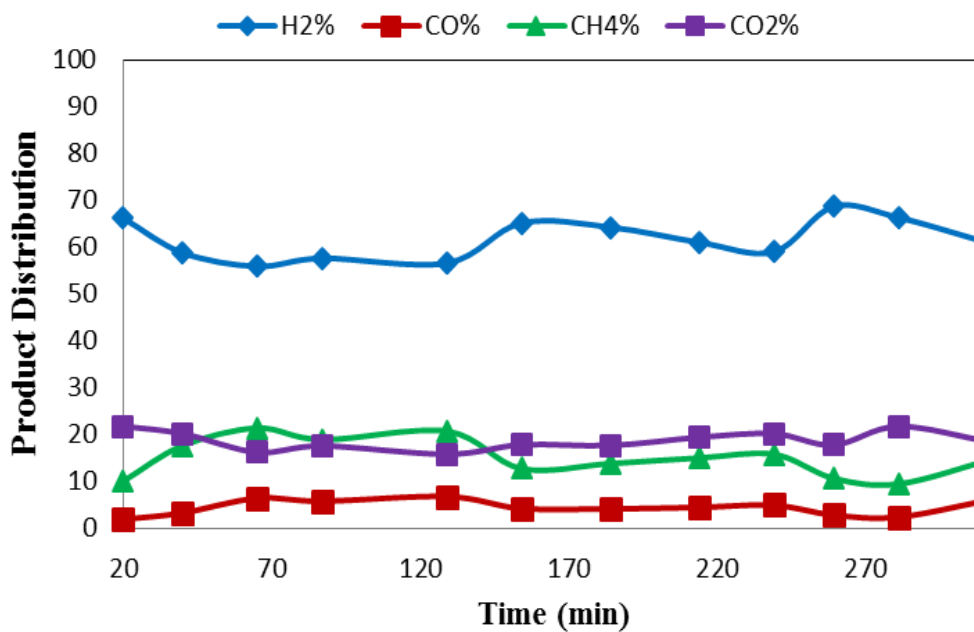


Figure 48: Product distribution at a reaction temperature of 450°C for SRE with Ni@CeO₂-ZrO₂ (6:1) calcined and reduced at 650°C

After the optimization of calcination, reduction and reaction temperatures, a third set of experiments were performed to test the effect of CeO₂/ZrO₂ ratio of the synthesized materials on catalytic performance in ethanol steam reforming. These experiments were performed at 450°C. Calcination and reduction temperatures of the synthesized materials were also kept as 450°C (Figure 49). Pure CeO₂ supported catalyst was found to be the least active one at 450°C and Ni@CeO₂-ZrO₂ (4:1) was found to be the most active catalyst. Inactivity of Ni@CeO₂ catalyst was probably due to the strong interaction of CeO₂ with nickel clusters, resulting in lower reducibility of nickel (quantity of Ni⁰ present on the surface). Similar results were reported by Biswas and Kunzru [60] and Jalowiecki-Duhamel et al. [39]. Another possible reason for inactivity of Ni@CeO₂ could be the lack of water adsorption-dissociation capability provided by ZrO₂ in other catalysts. Water adsorption/dissociation capability of zirconia is expected to facilitate ethanol steam reforming. Ni@CeO₂-ZrO₂ (4:1) catalyst presented very high activity, despite the fact that it possess the smallest surface area among the catalysts which were calcined and reduced at 450°C. The reason of its high hydrogen productivity could be the optimum acidity and reducibility provided by CeO₂/ZrO₂ ratio of 4, which was found elsewhere as the most optimum ratio for highest nickel reduction compared to pure CeO₂, ZrO₂ and CeO₂-ZrO₂ with other CeO₂/ZrO₂ ratios [60]. However, carbon deposition rate was higher on Ni@CeO₂-ZrO₂ (4:1) catalyst than catalysts possessing different CeO₂/ZrO₂ ratios. Change of this ratio from 4 to lower values resulted in a decrease of catalyst activity towards SRE and increase of this ratio from 4 to 6 affected the activity, slightly negatively. Catalysts having CeO₂/ZrO₂ ratio of 4 and 6 showed very stable activity in terms of hydrogen production at 450°C, allowing the possibility of long term stability in SRE (Figure 50, Figure 47). Another effect of the change CeO₂/ZrO₂ ratio on activity results was the CH₄ production rate. Increase of CeO₂ content resulted in an increase for CH₄ production, which indicates that CeO₂ favors mainly ethanol cracking reactions (R. 10, R. 11).

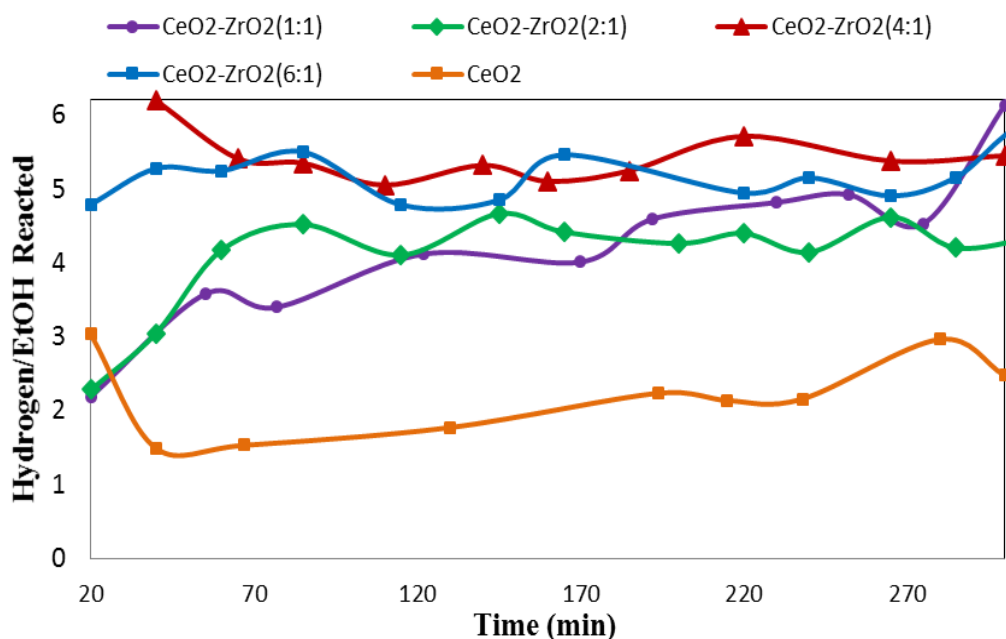


Figure 49: Comparison of hydrogen formation per mole of ethanol with Ni@CeO₂-ZrO₂ catalyst containing different CeO₂/ZrO₂ ratios calcined and reduced at 450°C at a reaction temperature of 450°C for SRE

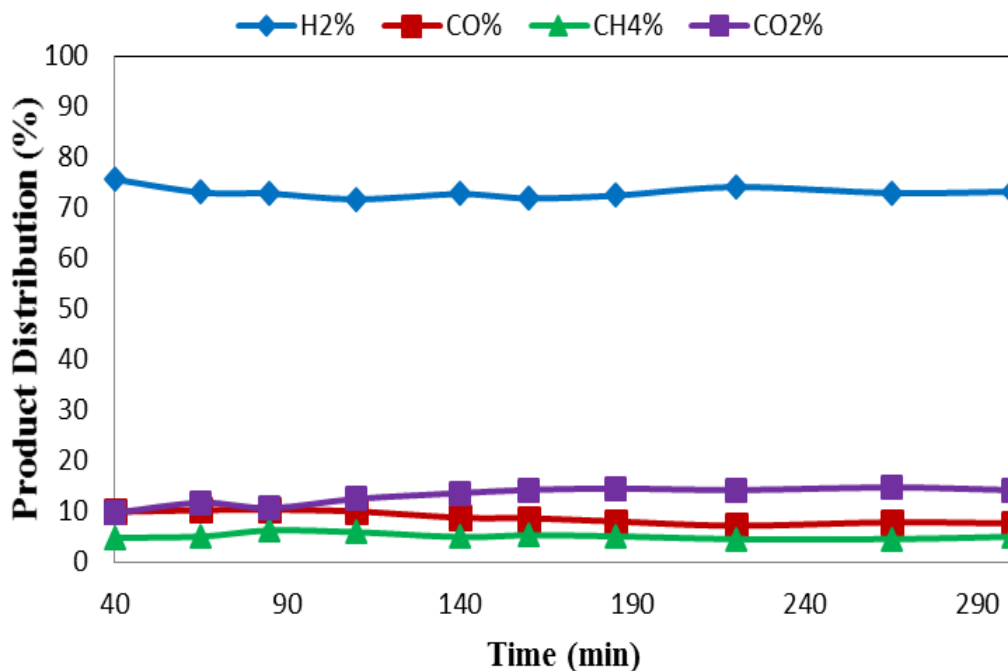


Figure 50: Product distribution at a reaction temperature of 450°C for SRE with Ni@CeO₂-ZrO₂ (4:1) catalyst calcined and reduced at 450°C.

6.5 CHARACTERIZATION RESULTS OF ZIRCONIA INCORPORATED MESOPOROUS CATALYSTS USED IN ACTIVITY TESTS

Thermal analysis (TGA), SEM and TEM images of the zirconia incorporated catalysts after 5 h of reaction period gave significant information about the nature of carbon deposits and their structural properties. TGA analysis gave information about the amount of coke formed on the catalysts (Table 9), as well as their nature. Formed coke was oxidized with air and the weight loss data of the used catalysts were presented in the following figures. Ni-Zr-SBA-15 catalyst used at different reaction temperatures; 550°C, 600°C, 650°C given in Figure 51 indicates lower coke deposition at higher reaction temperatures. Besides, increase of reaction temperature caused shift in oxidation temperature of carbon indicating the possibility of deposition of different forms of carbon or higher degree of graphitization on the catalyst surface at higher reaction temperatures during SRE. Weight loss data of Ni@Zr-SBA-15, Ni@Ce-Zr-SBA-15, Ni@Mg-Zr-SBA-15, Ni@Zr-MCM-41 and Ni@ZrO₂ catalysts used at a reaction temperature of 550°C and 600°C are given in Figure 52 and Figure 53, respectively. It can be clearly seen that while carbon accumulation on Ni@Zr-SBA-15 catalyst significantly decreased with an increase in 50°C of reaction temperature, other catalysts presented small changes in carbon deposition amounts. Difference in carbon deposition-gasification between these catalysts is related to the water adsorption-dissociation capability of the zirconia support. Mg²⁺ and Ce²⁺ incorporation did not cause any structural problems in Zr-SBA-15, on the contrary they improved the ordered mesoporous structure according to XRD patterns (Figure 22). Basic nature of these materials and their strong interaction with nickel clusters limited the carbon gasification capability of zirconia by reducing water to adsorb and dissociate on the surface on Zr-SBA-15. High coke formation on Ni@Zr-MCM-41 was caused by its higher Lewis acidity. The catalyst with the highest acidity was Ni@ZrO₂ which was found to be the one with the lowest carbon deposition. This situation was caused by its small surface area resulting in lowest activity towards both hydrogen production and carbon deposition. Weight loss data of Ni@Zr-SBA-15 and Ni@Mg-Zr-SBA-15 catalysts used at 600°C and with H₂O/EtOH of 3.2, 4 and 5 are given in Figure 54 and

Figure 55. While carbon deposition on Ni@Zr-SBA-15 did not change significantly, Ni@Mg-Zr-SBA-15 catalyst showed considerably high carbon deposition change between H₂O/EtOH of 4 and 5. It can be inferred that high steam ratios are necessary in order to activate the adsorption and dissociation capability of zirconia in Ni@Mg-Zr-SBA-15 type catalyst.

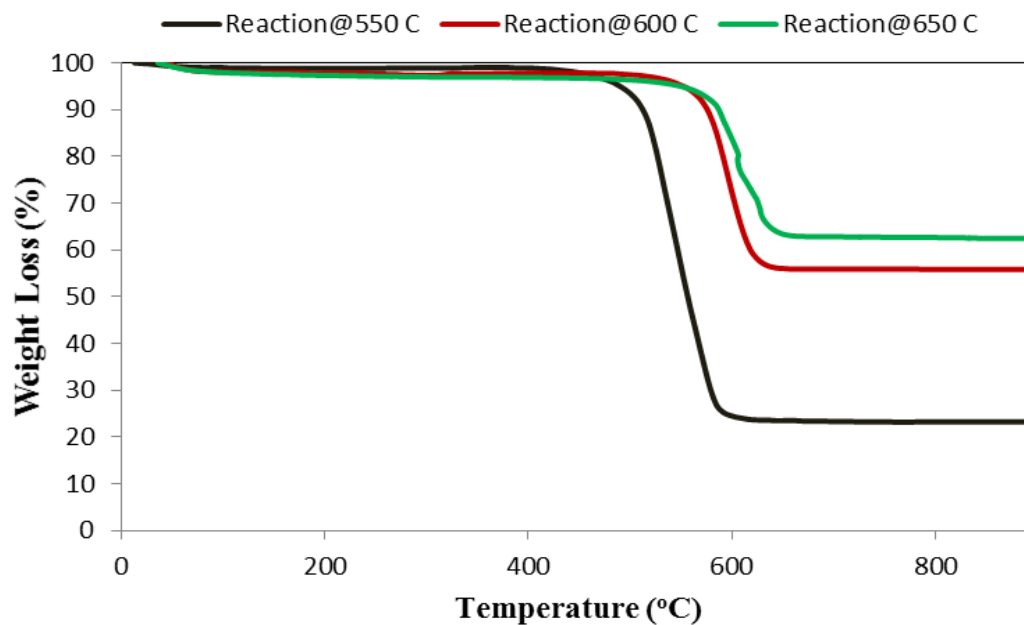


Figure 51: Weight loss (%) of Ni@Zr-SBA-15 used at reaction temperatures of 550°C, 600°C, 650°C.

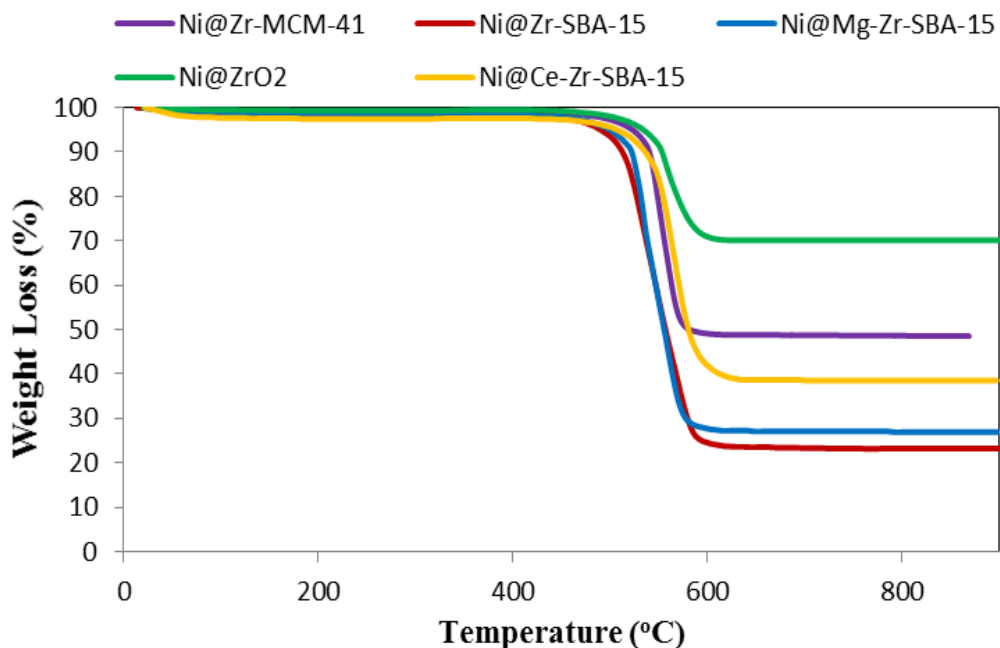


Figure 52: Weight loss (%) of Ni@Zr-SBA-15, Ni@Ce-Zr-SBA-15, Ni@Mg-Zr-SBA-15, Ni@Zr-MCM-41 and Ni@ZrO₂ catalysts used at a reaction temperature of 550°C.

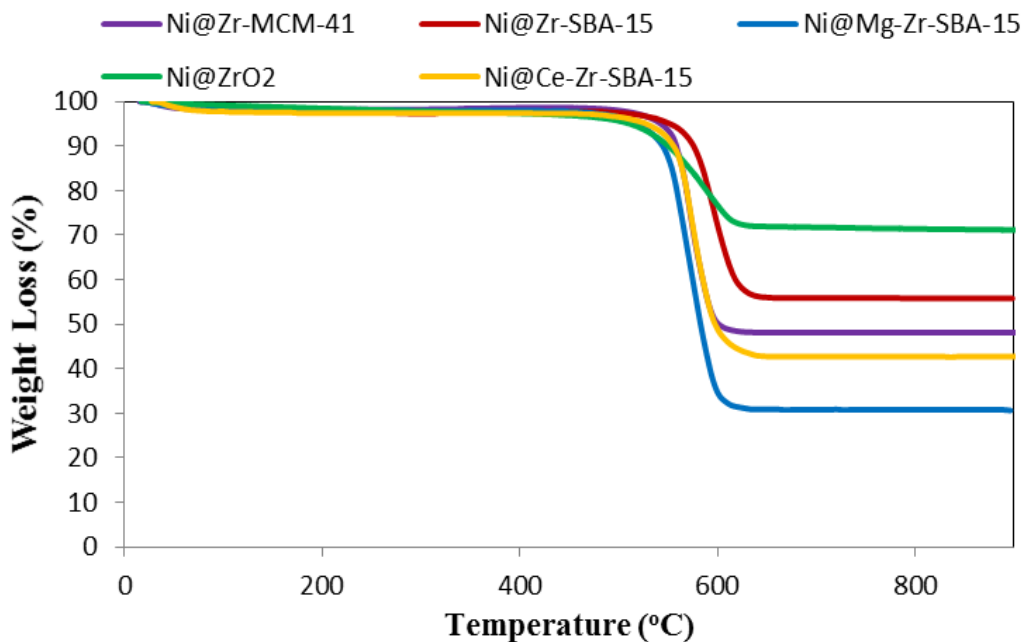


Figure 53: Weight loss (%) of Ni@Zr-SBA-15, Ni@Ce-Zr-SBA-15, Ni@Mg-Zr-SBA-15, Ni@Zr-MCM-41 and Ni@ZrO₂ catalysts used at a reaction temperature of 600°C.

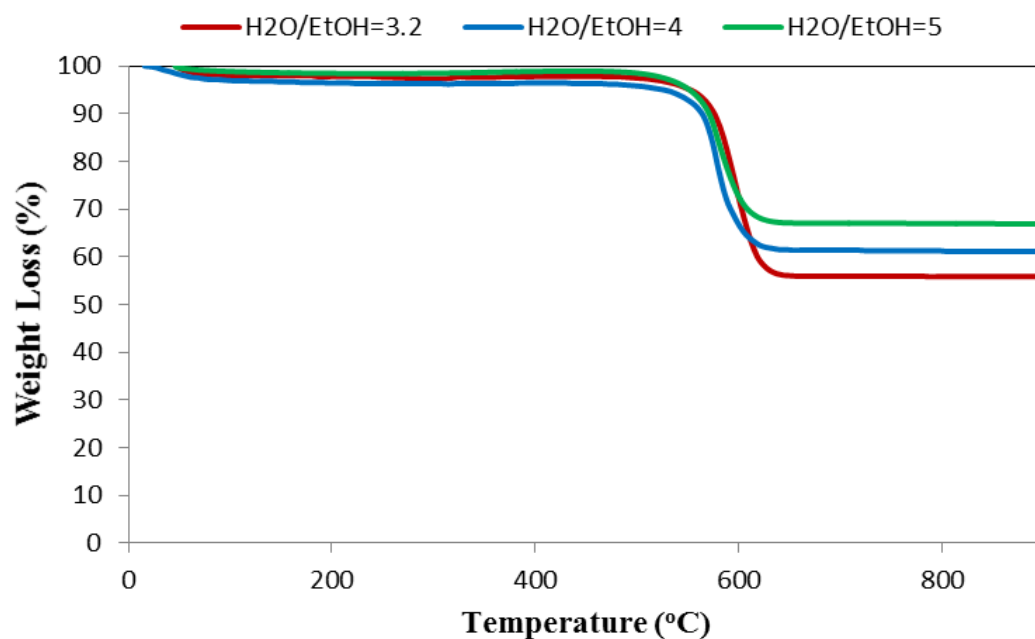


Figure 54: Weight loss (%) of Ni@Zr-SBA-15 used at 600°C with H₂O/EtOH of 3.2, 4 and 5

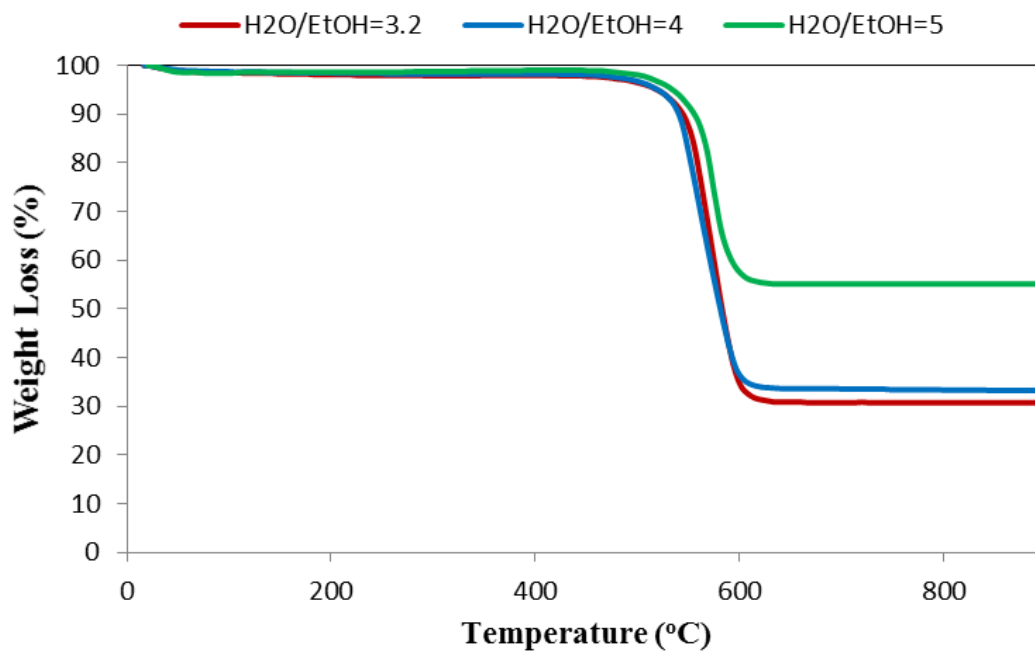


Figure 55: Weight loss (%) of Ni@Mg-Zr-SBA-15 used at 600°C with H₂O/EtOH of 3.2, 4 and 5

Filamentous carbon, which is originated from ethylene polymerization, is generally oxidized at temperatures below 530°C. More stable graphitized carbon is expected to be oxidized at higher temperatures during the TGA [34]. As shown in the analysis of differential of the weight loss data of Ni@Zr-SBA-15, Ni@Ce-Zr-SBA-15, Ni@Mg-Zr-SBA-15, Ni@Zr-MCM-41 and Ni@ZrO₂ catalysts used at a reaction temperature of 550°C and 600°C given in Figure 56 and Figure 57, both filamentous and graphitic carbons were deposited on the catalyst surfaces during ethanol steam reforming at 550°C. This was clearly seen especially over the SBA-15 type spent catalysts (Ni@Zr-SBA-15 and Ni@Mg-Zr-SBA-15). Two peaks in the DrTGA data indicated formation of filamentous carbon and graphite, which were oxidized at 530°C and 560°C, respectively. Presence of filamentous carbon on pure zirconia and Zr-MCM-41 type supported catalysts were also indicated by the start of weight loss before 530°C during the TGA test. With all catalysts, lower coke formation was observed at the reaction temperature of 600°C (Table 9). Increase of temperature enhanced gasification of filamentous carbon formed on the catalyst surface. DrTGA peaks at around 530°C corresponding to the filamentous carbon formed on the spent catalysts after SRE reaction were no longer observed at the reaction temperature of 600°C. Moreover, peaks are shifted to higher temperatures, due to higher degree of graphitization of coke deposits at 600°C reaction temperature.

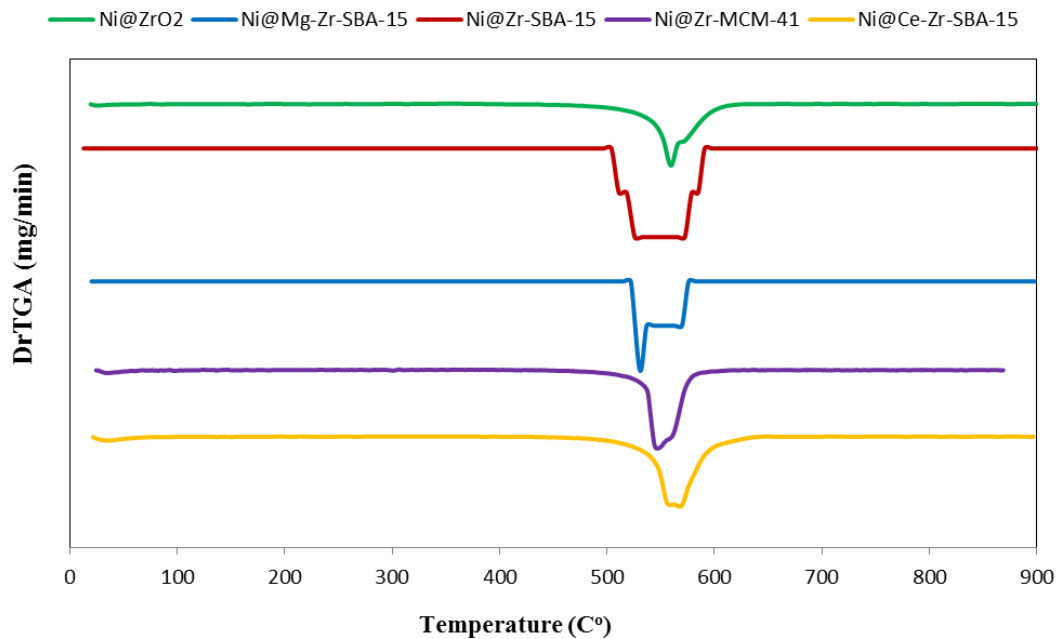


Figure 56: Derivative TGA of Ni@Zr-SBA-15, Ni@Ce-Zr-SBA-15, Ni@Mg-Zr-SBA-15, Ni@Zr-MCM-41 and Ni@ZrO₂ catalysts at 550°C.

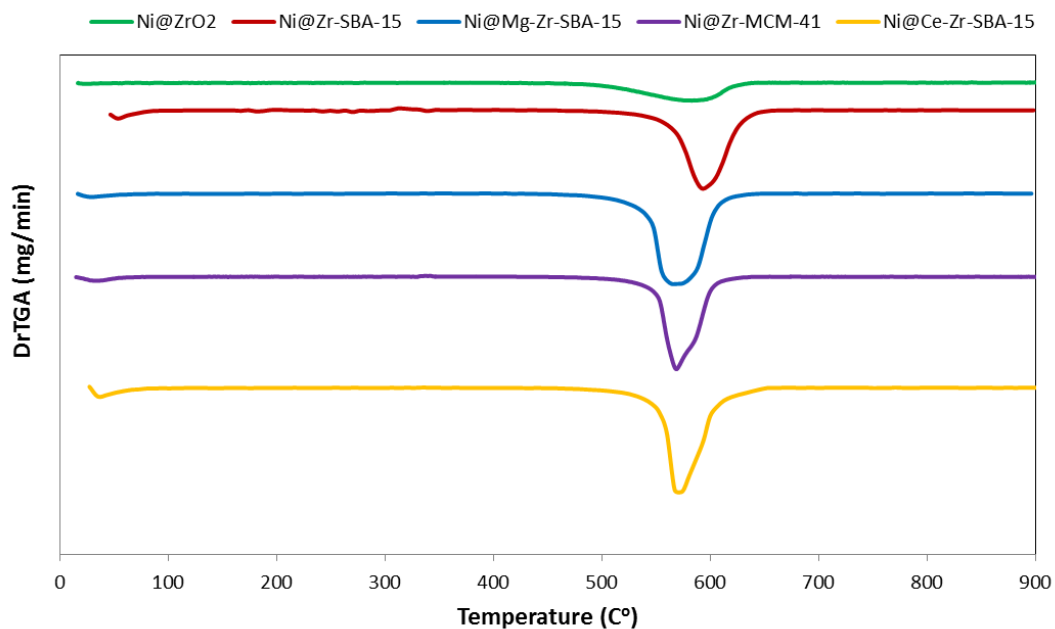


Figure 57: Derivative TGA of Ni@Zr-SBA-15, Ni@Ce-Zr-SBA-15, Ni@Mg-Zr-SBA-15, Ni@Zr-MCM-41 and Ni@ZrO₂ catalysts at 600°C.

TEM images of Ni@Zr-SBA-15 catalyst, which was exposed to SRE at 600°C for 5 h, indicated the preservation of the honeycomb shaped ordered mesoporous structure, despite the formation of 44% coke (Figure 58). Carbon filaments are observed on some parts of the material. Some of the dark spots seen in the images are nickel clusters, which can be clearly seen from EDX mapping results given in Figure 59, indicating that nickel crystals were still present and for this reason, coke accumulation was most likely occurred on Lewis acid sites present on the support.

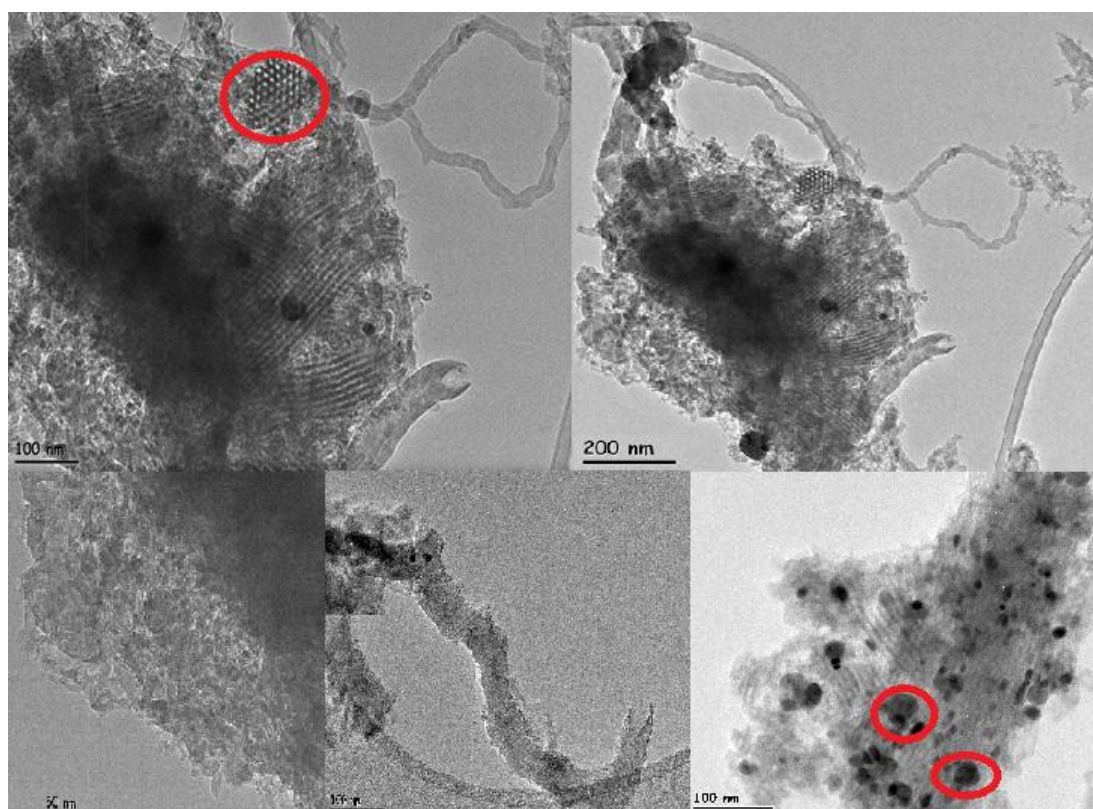


Figure 58: TEM images of Ni@Zr-SBA-15 catalyst after reaction at 600°C with H₂O/EtOH=3.2 for 5 h

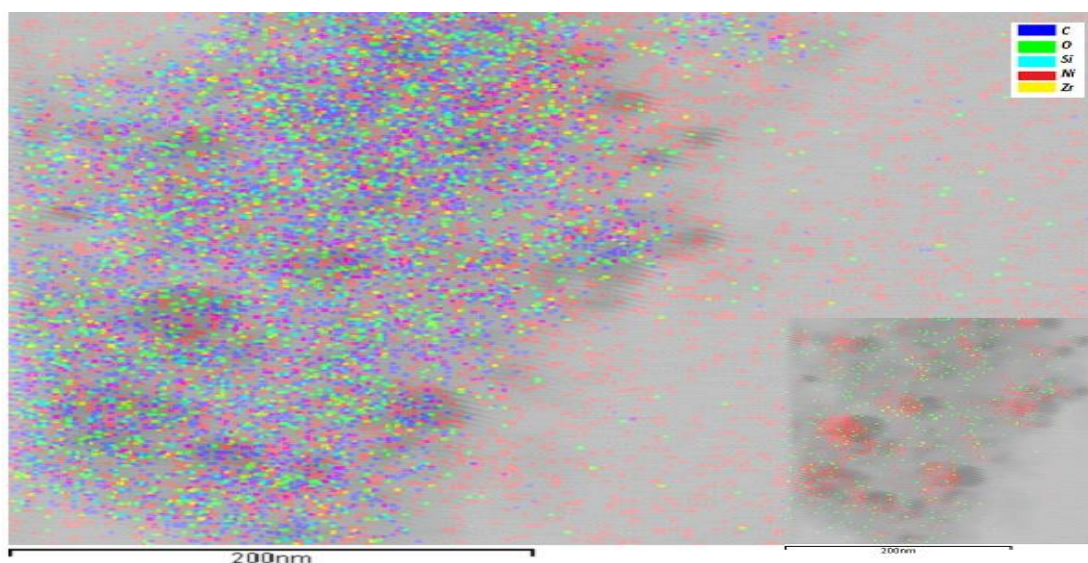


Figure 59: EDX metal mapping images of Ni@Zr-SBA-15 catalyst after reaction at 600°C with H₂O/EtOH=3.2 for 5 h

SEM images clearly showed the formation of carbon filaments on both Ni@Zr-SBA-15 (Figure 60) and Ni@Mg-Zr-SBA-15 (Figure 61) catalysts after reaction at 600°C with H₂O/EtOH=3.2 for 5 h. Catalyst surfaces were partially surrounded by carbon filaments. For both catalysts, two different zones were selected and analyzed with carbon mapping. While one of the surfaces showed very dense carbon deposition in both catalysts, the other image presented lower carbon formation. Results proved that coke was not deposited uniformly over the catalyst and high activity can still be maintained. Higher carbon deposition on Mg²⁺ containing catalyst can be clearly seen from the carbon mapping analysis. Carbon filaments are more distinct in the SEM images obtained from used Ni@Mg-Zr-SBA-15 catalyst.

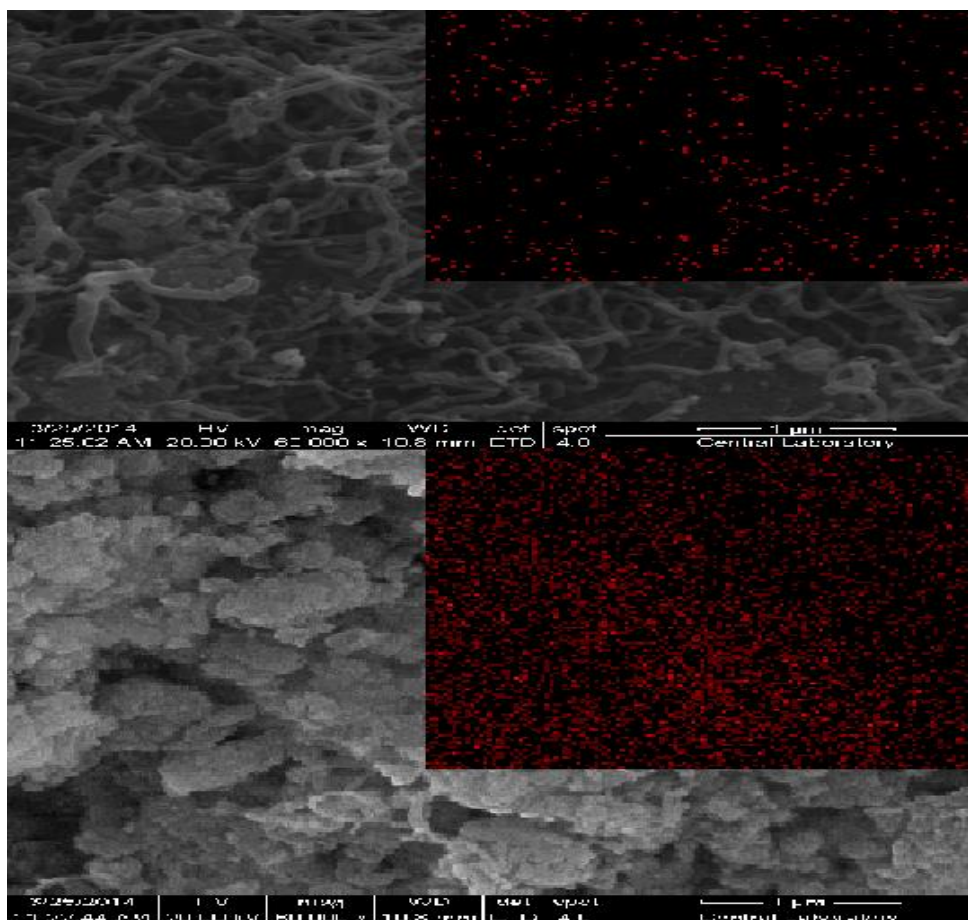


Figure 60: SEM images and carbon distributions of Ni@Zr-SBA-15 after reaction at 600°C with H₂O/EtOH=3.2 for 5 h (red points correspond to carbon on the surface)

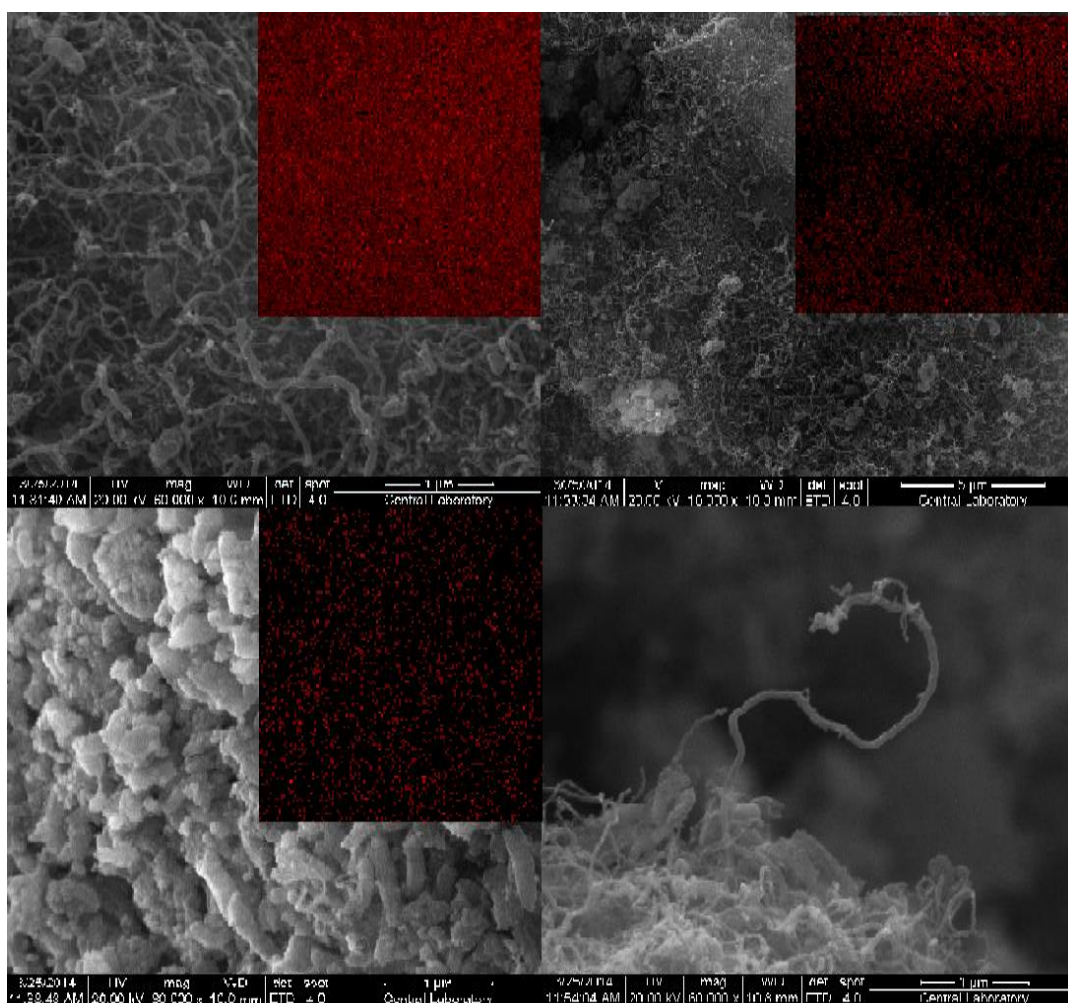


Figure 61: SEM images and carbon distributions of Ni@Mg-Zr-SBA-15 after reaction at 600°C with H₂O/EtOH=3.2 for 5 h (red points correspond to carbon on the surface)

6.6 CHARACTERIZATION RESULTS OF CeO₂-ZrO₂ SUPPORTED CATALYSTS USED IN ACTIVITY TESTS

Thermal analysis (TGA) of the catalysts used in ethanol steam reforming system for 5 h reaction period gave significant information about the amount of coke deposition on catalyst surface and their structural properties of CeO₂-ZrO₂ supported catalysts. Formed coke was oxidized with air and the weight loss data of Ni@CeO₂-ZrO₂ (6:1) catalyst calcined, reduced and exposed to reaction at 400°C, 450°C, 500°C, 550°C, 600°C and 650°C are given in Figure 62. It can be seen that maximum coke formation was occurred at 500°C and 550°C due to high activity of Boudouard reaction at these temperatures. Below 500°C, apparently coke formation was prohibited by catalysts with their low crystal size and high oxygen mobility. Above 550°C, deposited coke was gasified by CeO₂-ZrO₂ with its high water adsorption-dissociation capability and high oxygen mobility. Only 6% coke at 600°C and 3% coke at 650°C were formed. At 400°C and 450°C, only 3% weight loss was observed at around 295°C indicating amorphous carbon deposition. Oxidation temperature cannot be exactly observed from weight loss data, so derivative of weight loss data was analyzed in order to understand the nature of deposited carbon clearly. Oxidation temperature peaks of deposited coke further indicated the nature of carbon accumulated on the surface. As mentioned before, filamentous carbon, which is originated from ethylene polymerization, is generally oxidized at temperatures between 300°C and 530°C. Temperatures higher than 530°C are associated with coke deposits with different degree of graphitization formed through Boudouard reaction (R.16) [34]. Figure 62 and Figure 63 indicated the formation of coke deposits with different degree of graphitization above 500°C. Increase of temperature shifted the carbon oxidation to higher temperatures meaning higher degree of graphitization. Similarly, weight loss data and differential weight loss data of catalysts calcined and reduced at 650°C and used in reactions at 450°C, 550°C, 600°C and 650°C in the second set of experiments are given in Figure 64 and Figure 66, respectively. Carbon deposition at 650°C was very low due to enhanced gasification reaction. While higher carbon deposition was observed at 550°C and 600°C, activity tests at 450°C presented much higher coke deposition (34%). When it

was compared to the test results of the catalyst calcined and reduced at 450°C which only possessed 2% carbon deposition, it is clear that crystal growth of the metals in catalysts caused high rates of carbon accumulation. It can be inferred that the main reason of coke deposition on Ni@CeO₂/ZrO₂ catalyst is large crystal sizes occurred after high temperature treatment.

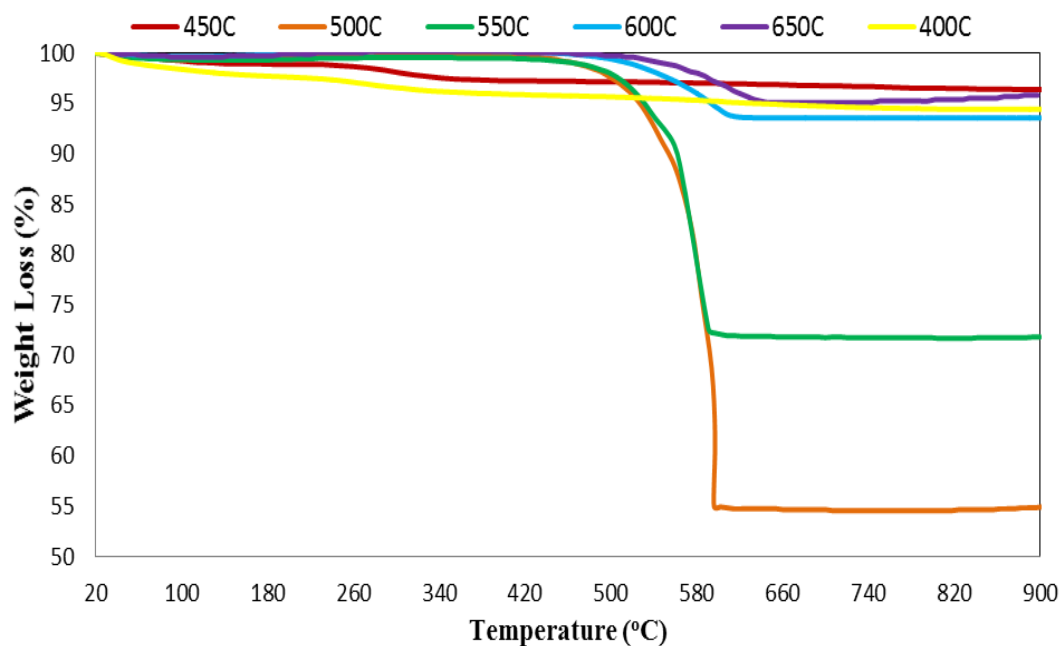


Figure 62: Weight loss (%) of Ni@CeO₂-ZrO₂ (6:1) catalyst calcined, reduced and exposed to reaction at 400°C, 450°C, 500°C, 550°C, 600°C and 650°C.

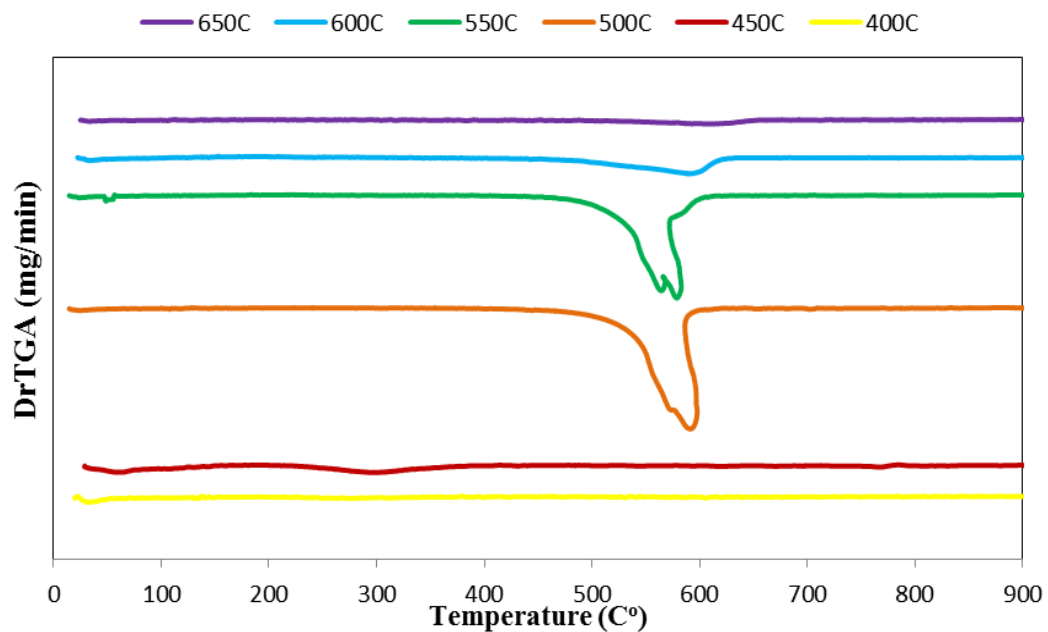


Figure 63: Differential weight loss of Ni@CeO₂-ZrO₂ (6:1) catalyst calcined, reduced and exposed to reaction at 400°C, 450°C, 500°C, 550°C, 600°C and 650°C.

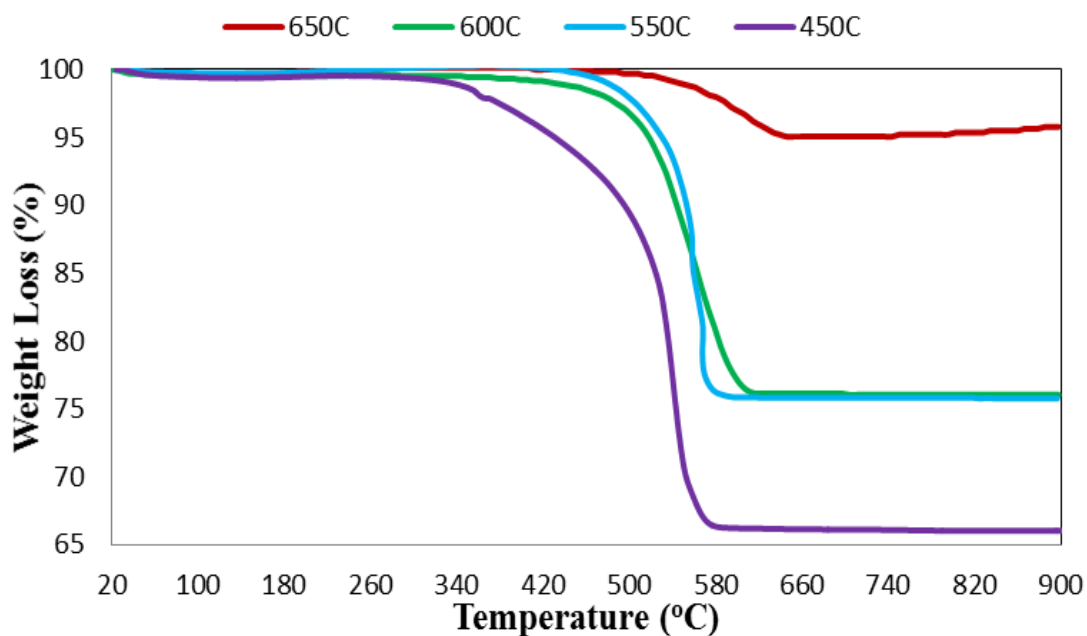


Figure 64: Weight loss (%) after SRE at 450°C, 550°C, 600°C and 650°C of Ni@CeO₂-ZrO₂ (6:1) catalyst calcined and reduced at 650°C

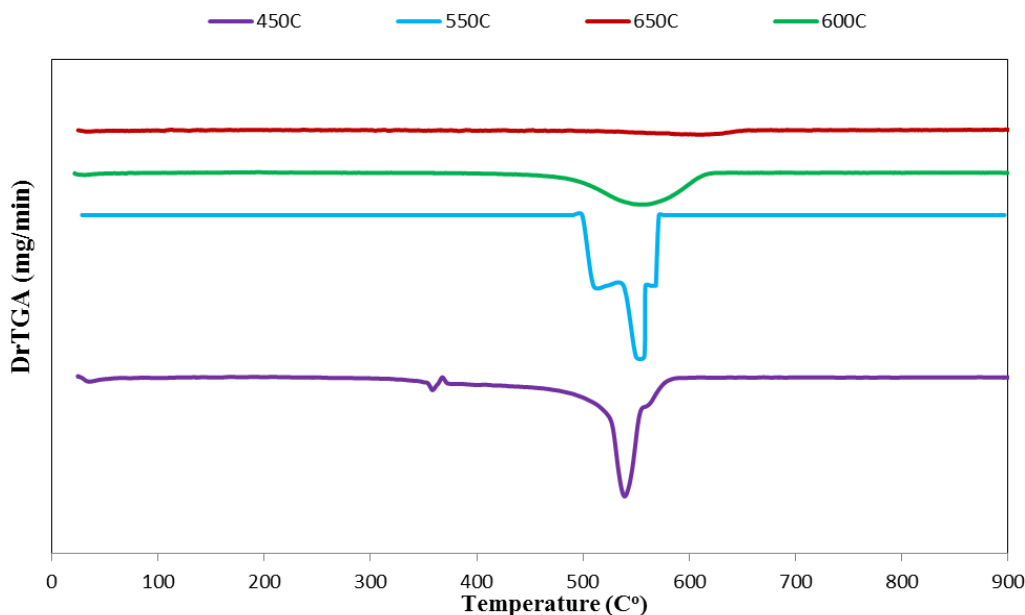


Figure 65: Differential weight loss after SRE at 450°C, 550°C, 600°C and 650°C of Ni@CeO₂-ZrO₂ (6:1) catalyst calcined and reduced at 650°C

Thermogravimetric analysis of Ni@CeO₂-ZrO₂ catalysts with different CeO₂/ZrO₂ ratios indicated small amount of coke formation except for Ni@CeO₂-ZrO₂ (4:1) and Ni@CeO₂-ZrO₂ (1:1) (Figure 66). Ni@CeO₂ catalyst exhibited no coke formation which was not surprising, considering its inactivity towards ethanol steam reforming due to strong interaction of CeO₂ with nickel, causing lower reducibility. Ni@CeO₂-ZrO₂ (6:1) catalyst showed very high activity towards ethanol steam reforming and only 3% coke deposition which was classified as amorphous carbon, oxidized at 295°C, as mentioned. Ni@CeO₂-ZrO₂ (2:1) presented lower reforming activity and slightly higher coke accumulation with 4% which was oxidized at 610°C meaning graphitized carbon accumulation. Ni@CeO₂-ZrO₂ (1:1) catalyst presented very unstable activity and very high carbon deposition which was caused by its higher zirconia content. Both filamentous and graphitized carbon accumulation were observed on this catalyst. The most successful catalyst towards ethanol steam reforming was found as Ni@CeO₂-ZrO₂ (4:1) catalyst, but coke deposition on this material after catalytic tests was found as about 30% graphitic carbon. The reason of

this high activity both towards reforming and coking is believed to be the higher reducibility of this catalyst as mentioned before.

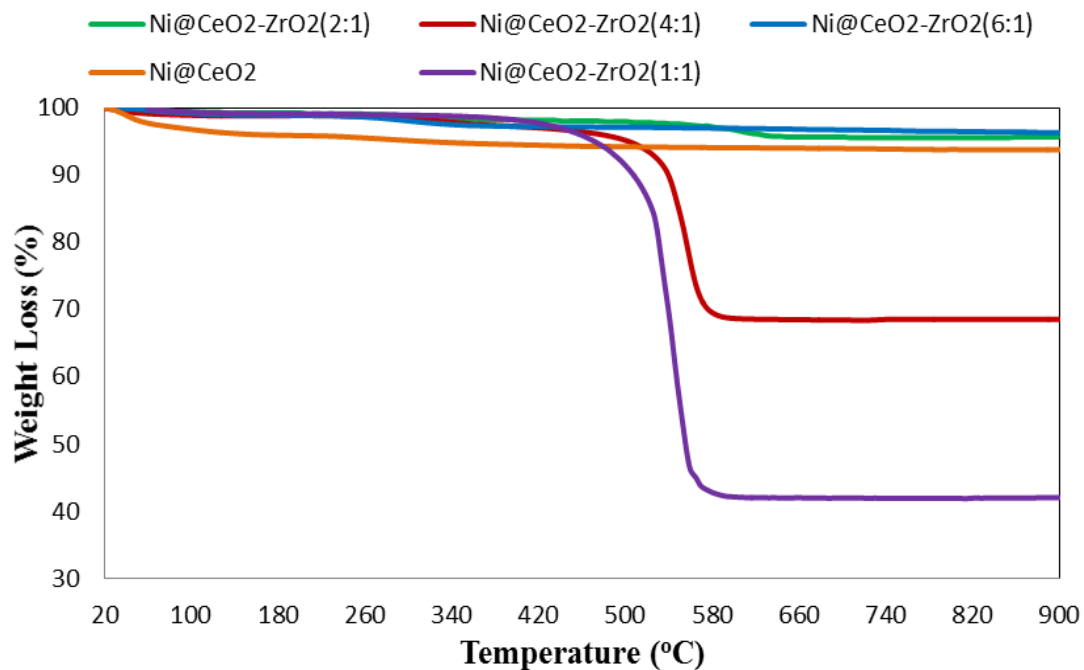


Figure 66. Weight loss (%) after SRE at 450°C of Ni@CeO₂-ZrO₂ catalyst with different CeO₂/ZrO₂ ratios.

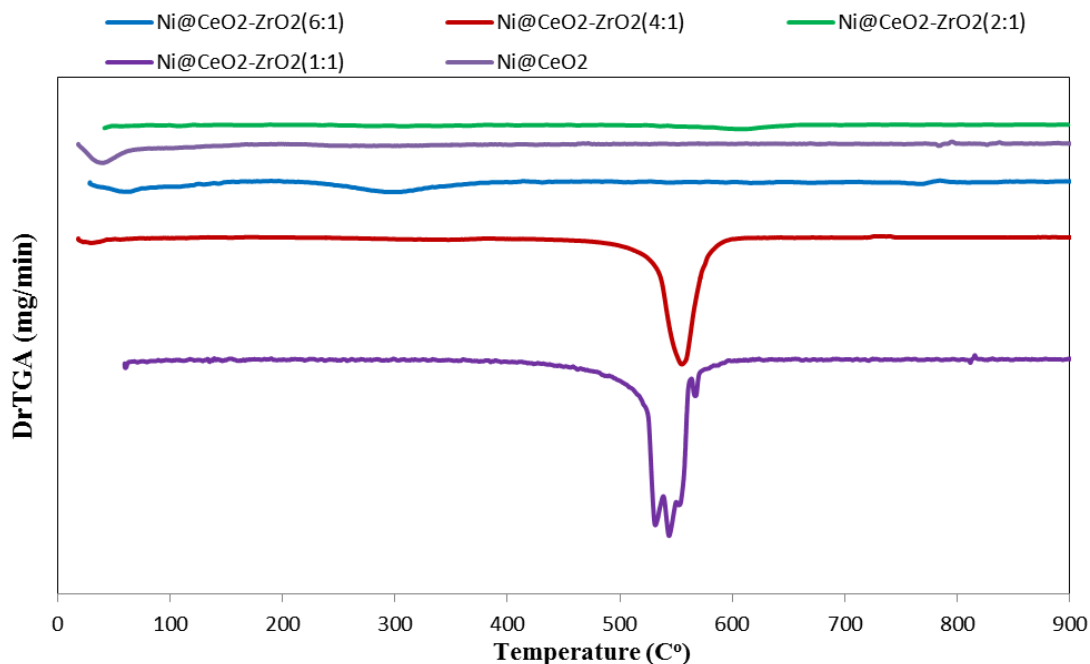


Figure 67. Differential weight loss after SRE at 450°C of Ni@CeO₂-ZrO₂ catalyst with different CeO₂/ZrO₂ ratios.

X-ray diffraction patterns of the catalysts, which presented very high activity (Ni@CeO₂-ZrO₂ (4:1) calcined, reduced and used at 450°C, Ni@CeO₂-ZrO₂ (6:1) calcined, reduced and used at 450°C, Ni@CeO₂-ZrO₂ (6:1) calcined, reduced and used at 650°C) are given in Figure 68 Catalysts did not show any peak indicating carbon deposition in the XRD structure. Absence of carbon peak was surprising for Ni@CeO₂-ZrO₂ (4:1) catalyst since carbon deposition on these materials after ethanol steam reforming reaction at 450°C was 30%. Slight shift (~0.5°) in the XRD peaks of Ni@CeO₂-ZrO₂ (4:1) was observed and crystal size of CeO₂-ZrO₂ solid solution decreased from 5.6 nm to 4.7 nm. For Ni@CeO₂-ZrO₂ (6:1) calcined, reduced and used at 450°C, absence of carbon peak is acceptable since only 3% coke was deposited on its surface. While peaks were protected their position, crystal size of CeO₂-ZrO₂ solid solution increased from 4.9 nm to 5.1 nm. Peaks in the XRD pattern Ni@CeO₂-ZrO₂ (6:1) calcined, reduced and used at 650°C also preserved their places, but crystal size of CeO₂-ZrO₂ solid solution decreased from 13 nm to 11.2 nm.

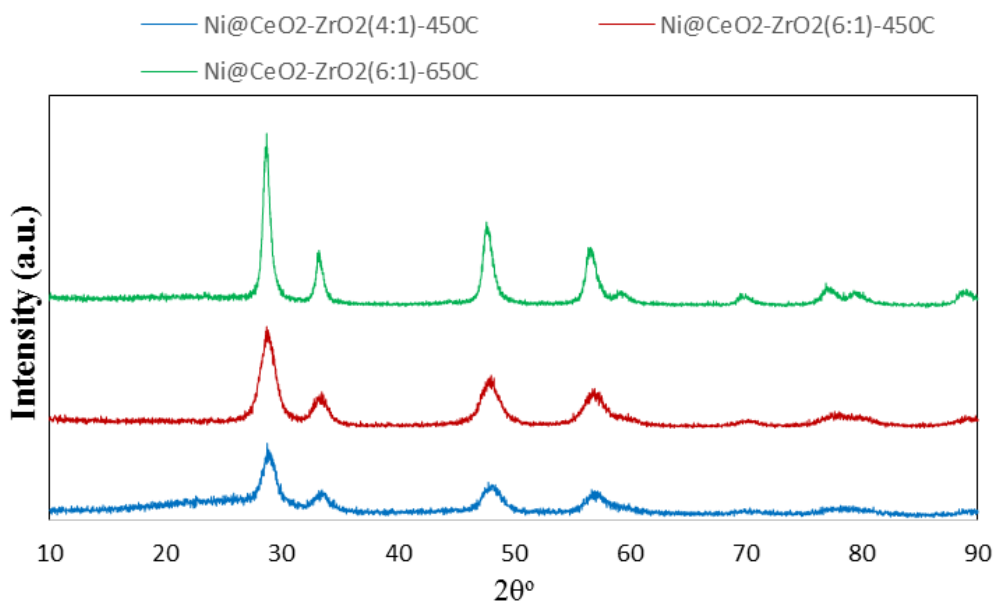


Figure 68. X-ray diffraction patterns of used Ni@CeO₂-ZrO₂ (4:1) calcined, reduced and used at 450°C, Ni@CeO₂-ZrO₂ (6:1) calcined, reduced and used at 450°C, Ni@CeO₂-ZrO₂ (6:1) calcined, reduced and used at 650°C.

6.7 SUMMARY OF ZIRCONIA INCORPORATED MESOPOROUS CATALYSTS

In order to see the effect of type of zirconia-silicate supported catalyst used, reaction temperature and H₂O/EtOH ratio on ethanol conversion, hydrogen formation and amount of carbon deposition, some of the catalyst properties that has a major impact on the activity were summarized in Table 11.

Table 11: Properties and activity results of zirconia incorporated mesoporous catalysts

Catalyst	S _{BET} (m ² /g)	D _P (nm)	Ni ^o Crystal Size (nm)	Rxn T (°C)	H ₂ O/EtOH (mol/mol)	H ₂ yield	Coke (wt. %)
Ni@ZrO ₂	23.8	2.7	15.2	550	3.2	4.19	30
				600	3.2	4.42	26
Ni@Zr-SBA-15	515	5.7	22.9	550	3.2	4.84	76
				600	3.2	4.90	44
					4.0	5.10	38
				650	5.0	5.00	33
					3.2	5.59	37
				Ni@Ce-Zr-SBA-15			10.4
600	3.2	4.25	57				
Ni@Mg-Zr-SBA-15	456	6.6	21.2	550	3.2	4.25	73
				600	3.2	5.54	69
					4.0	5.82	66
					5.0	5.59	45
Ni@Zr-MCM-41	338	3.4	17.0	550	3.2	3.88	51
				600	3.2	5.40	52

- Zirconia-silicate type mesoporous catalysts with ordered pore structures resulted in higher surface area and pore diameter than pure zirconia supported catalyst. Ni^o crystal size was smaller in Ni@ZrO₂ than in Ni@Zr-SBA-15, Ni@Mg-Zr-SBA-15 and Ni@Zr-MCM-41 catalysts. However, smallest Ni^o crystal size was found in Ni@Ce-Zr-SBA-15 catalysts due to strong interaction of ceria with nickel. Acidities of these catalysts were found to be changed in the following order; Ni@ZrO₂ > Ni@Zr-MCM-41 > Ni@Zr-SBA-15 > Ni@Mg-Zr-SBA-15~Ni@Ce-Zr-SBA-15.
- Zirconia based catalysts found to be very active towards ethanol steam reforming reaction, resulting complete conversion of ethanol at all temperatures and H₂O/EtOH ratios. Activity tests performed at 550°C with zirconia-silicate type mesoporous catalysts resulted in high amounts of coke formation (>50 wt.%). When the reaction temperature was raised to 600°C,

coke formation amount on Ni@Mg-Zr-SBA-15, Ni@Zr-MCM-41 and Ni@Ce-Zr-SBA-15 catalysts presented slight reduction, but carbon deposition dropped from 76 wt. % to 44 wt.% on Ni@Zr-SBA-15. Difference in carbon deposition-gasification between these catalysts is related to the water adsorption-dissociation capability of the zirconia support. Common properties of Mg²⁺ and Ce²⁺ such as their basic nature and strong interaction with nickel clusters limited the carbon gasification capability of zirconia by reducing water to adsorb and dissociate on the surface on Zr-SBA-15. High coke formation on Ni@Zr-MCM-41 was caused by its higher Lewis acidity.

- Increase of H₂O/EtOH ratio enhanced hydrogen productivity while decreasing carbon monoxide formation and carbon deposition on Ni@Zr-SBA-15 and Ni@Mg-Zr-SBA-15 catalysts. Significant carbon deposition change was observed between H₂O/EtOH ratio of 4 and 5 on Ni@Mg-Zr-SBA-15 catalyst. It indicates that a certain steam amount is necessary to gasify the deposited filamentous carbon on Ni@Mg-Zr-SBA-15 catalyst.
- Investigation of zirconia-silicate type mesoporous catalysts in ethanol steam reforming reaction showed that coke formation does not depend mainly on acidity of the catalyst. Both acidity and catalyst capability for adsorption and dissociation of water to gasify the accumulated carbon are main factors for coke minimization.

6.8 SUMMARY OF CeO₂-ZrO₂ SUPPORTED CATALYSTS

In order to see the effect of temperature and catalyst content on the activity results of CeO₂-ZrO₂ supported catalysts, ethanol conversion, hydrogen formation and some of the catalyst properties that has a major impact on the activity were summarized in Table 12.

Table 12: Summary of catalyst properties and activity test results of CeO₂-ZrO₂ supported catalysts

Catalyst	Calc&Red T (°C)	S _{BET} (m ² /g)	DP (nm)	CeO ₂ -ZrO _{2ss} crystal size	Rxn T (°C)	EtOH Conversion	H ₂ /mole of EtOH	Coke (wt. %)
Ni@CeO ₂ -ZrO ₂ (6:1)	650	12.8	1.6	13.0	650	100	4.75	4
					600	100	4.60	24
					550	96.3	3.74	24
					450	94.5	3.28	34
Ni@CeO ₂ -ZrO ₂ (6:1)	600	31.7	1.9	9.2	600	89.3	3.98	6
Ni@CeO ₂ -ZrO ₂ (6:1)	550	11.9	1.9	9.1	550	89.3	3.98	28
Ni@CeO ₂ -ZrO ₂ (6:1)	500	16.4	3.8	7.1	500	82.4	3.76	45
Ni@CeO ₂ -ZrO ₂ (6:1)	450	61.0	3.8	4.9	450	80.0	5.15	3
Ni@CeO ₂ -ZrO ₂ (6:1)	400	82.8	3.8	4.2	400	57.0	5.08	2
Ni@CeO ₂ -ZrO ₂ (4:1)	450	29.2	4.2	5.6	450	100	5.43	30
Ni@CeO ₂ -ZrO ₂ (2:1)	450	65.2	3.4	5.0	450	82.1	4.09	4
Ni@CeO ₂ -ZrO ₂ (1:1)	450	60.0	3.8	3.8	450	85.2	4.46	57
Ni@CeO ₂	450	119	3.8	6.9	450	100	2.2	6

- Change of reaction temperature from 650°C to 600°C, 550°C and 450°C with Ni@CeO₂-ZrO₂ (6:1) catalyst calcined and reduced at 650°C resulted in slight decrease in ethanol conversion and significant drop of hydrogen formation. Coke formation also increased from 4 wt. % to 34 wt. % with a decrease of reaction temperature about 200°C. At lower temperatures contribution of Boudouard reaction becomes significant for catalysts having large Ni and ceria crystal sizes.

- Keeping the calcination, reduction and reaction temperatures the same, at values of 650°C, 600°C, 550°C, 500°C, 450°C and 400°C, with Ni@CeO₂-ZrO₂ (6:1) catalyst, a set of results were obtained to optimize temperature. Results showed the possibility of high activity at low temperatures. It can be seen that increase of calcination and reduction temperature generally decreases surface area of the catalysts due to crystal growth of CeO₂-ZrO₂ solid solution. Other than surface area, pore structure changes and significantly destroys the mesoporous structure of the catalysts. Nickel oxide crystals with dimensions of 9 and 7 nm were observed at 650°C and 600°C, respectively. However, Ni cluster size was smaller than the detection limit of XRD, for the catalysts calcined/reduced at lower temperatures. This also had a positive effect on coke minimization. Calcination, reduction and operation of ethanol steam reforming reaction at high temperatures (600°C and 650°C) resulted in complete ethanol conversion, very high hydrogen formation and small amount of graphitic carbon deposition. Low temperatures (400°C and 450°C) also yielded very high hydrogen production per mole of reacted ethanol and very low coke formation. Lower ethanol conversion was observed at these temperatures which can be increased by an increase in space time in the reactor.
- When only calcination and reduction temperatures of 450°C and 650°C were compared in terms of product properties, ethanol steam reforming activities and coke formation, 450°C is clearly more advantageous than higher temperatures. In terms of catalyst properties, the one treated at low temperature possess much higher surface area, pore diameter and smaller crystal sizes. When catalytic activities are compared, calcination and reduction at 450°C resulted in superior stability (3 wt. % coke) and over 90% hydrogen formation per mole of ethanol reacted out of 6, whereas hydrogen yield on Ni@CeO₂-ZrO₂ (6:1) calcined and reduced at 650°C could not even reached 60% of the maximum possible value of 6.
- Temperature analysis showed that the optimum calcination, reduction and reaction temperature for Ni@CeO₂-ZrO₂ (6:1) catalyst is 450°C for ethanol

steam reforming reaction. This temperature provides better catalyst properties which leads to higher activity in ethanol steam reforming reaction.

- Optimization of $\text{CeO}_2/\text{ZrO}_2$ ratios of $\text{Ni}@\text{CeO}_2\text{-ZrO}_2$ catalysts showed the importance of ZrO_2 incorporation to the material. $\text{Ni}@\text{CeO}_2$ favored methane formation through cracking and reverse dry reforming reactions. Increase of ZrO_2 content enhanced hydrogen productivity and reduced methane formation. $\text{Ni}@\text{CeO}_2\text{-ZrO}_2$ (4:1) catalyst presented very high activity despite the fact that it possess the smallest surface area among the catalysts which were calcined and reduced at 450°C . However, high amount of graphitic carbon (30 wt. %) was deposited on this material.

CHAPTER 7

CONCLUSION

Hydrogen has been considered as an ideal energy carrier that will reduce the dependence on fossil fuels. Hydrogen powered fuel cell vehicles are expected to be efficient and harmless to the environment which is possible as long as hydrogen is produced cleanly. Hydrogen production from bio-ethanol has been considered as a promising route, since bio-ethanol is the most available bio-fuel in the world and high hydrogen production could be performed with ethanol steam reforming reaction. However, major disadvantage of this reaction is coke formation. The main objective of this study was to achieve high purity hydrogen production with minimum coke deposition by using zirconia-silicate and ceria-zirconia supported nickel catalyst. In this study, Ni@ZrO₂, Ni@Zr-SBA-15, Ni@Ce-Zr-SBA-15, Ni@Mg-Zr-SBA-15, Ni@Zr-MCM-41 and Ni@CeO₂-ZrO₂ catalysts with changing treatment temperatures and CeO₂/ZrO₂ ratios were used in ethanol steam reforming activity tests.

Both ZrO₂ and zirconia incorporated SBA-15 and MCM-41 type catalyst supports were successfully synthesized with high surface area and mesoporous structure. Nickel impregnation and high temperature calcination and reduction changed the structural properties of ZrO₂. However, silica-based materials preserved their ordered mesoporous structures. Acidities of these catalysts were found to be changed in the following order; Ni@ZrO₂ > Ni@Zr-MCM-41 > Ni@Zr-SBA-15 > Ni@Mg-Zr-SBA-15~Ni@Ce-Zr-SBA-15. Ni@Zr-SBA-15 catalyst resulted in very high catalytic activity, hydrogen yield values approaching to 90% of the maximum possible yield of 6 and stability at 600°C and 650°C. Mg²⁺ incorporated Zr-SBA-15 catalyst lost its high initial activity due to high rates of carbon deposition. Carbon accumulation difference between 550°C and 600°C in Ni@Zr-SBA-15 and Ni@Mg-

Zr-SBA-15 suggested that magnesia had a limiting effect of carbon gasification by reducing water adsorption-dissociation capability of zirconia support. Ce^{4+} incorporation into Zr-SBA-15 catalyst reduced the nickel crystal size significantly while increasing the instability of the catalyst in activity tests due to much higher carbon deposition. These catalysts showed that coking tendency in ethanol steam reforming reactions is not completely related to number of acid sites of the catalyst. Both acidity and ability of catalyst for dissociation of water to gasify the deposited carbon should be adjusted to obtain maximum hydrogen yield with minimum coking.

Investigation of the mesoporous $\text{CeO}_2\text{-ZrO}_2$ supported catalysts in steam reforming of ethanol process required optimization of catalyst properties such as calcination and reduction temperature and $\text{CeO}_2/\text{ZrO}_2$ ratio of the catalyst. While investigating the calcination and reduction temperature effect on catalytic properties and reaction temperature on catalytic activity of the nickel catalyst with $\text{CeO}_2/\text{ZrO}_2$ ratio of 6, 450°C was found to be the optimum for calcination, reduction and operating temperatures. Increase of calcination and reduction temperature above 450°C resulted in collapse of the mesoporous structure of $\text{Ni@CeO}_2\text{-ZrO}_2$ (6:1) due to crystal growth, limited SRE activity and higher coke deposition. Activity tests performed at 450°C with $\text{Ni@CeO}_2\text{-ZrO}_2$ (6:1) revealed the importance of calcination & reduction temperature which was changed from 450°C to 650°C , in terms of ethanol steam reforming activity. The material calcined and reduced at 650°C caused very poor hydrogen productivity at 450°C and 34% carbon deposition. Only 2% coke deposition was occurred with the material calcined and reduced at 450°C and hydrogen formation per mole of ethanol was found as 5.15 at 450°C corresponding to 86% of the maximum possible value of 6. Investigation of the optimum $\text{CeO}_2/\text{ZrO}_2$ ratio revealed that a ratio of 4 provides highest activity with over 90% hydrogen production per mole of ethanol due to possibly optimum acidity and more importantly higher nickel reducibility compared to pure CeO_2 , ZrO_2 and $\text{CeO}_2\text{-ZrO}_2$ with other $\text{CeO}_2/\text{ZrO}_2$ ratios. Outstanding SRE activity of this catalyst also resulted in very high coke formation, but did not affected the stability of the catalyst during the reaction period of 5 h.

REFERENCES

- [1] Schumacher, E. F., *Schumacher on energy: speeches and writings of E.F. Schumacher*. Jonathan Cape Ltd, London, 1982, p. 212.
- [2] Midilli A., Ay M., Dincer I. and Rosen M. A., “On hydrogen and hydrogen energy strategies I: current status and needs,” *Renew Sust Energ Rev*, 9: 255–271, 2005.
- [3] Giacomelli G., “The energy problem,” *Radiati Meas*, 44 (9–10): 707–716, 2009.
- [4] Goldthau A. and Sovacool B. K., “The uniqueness of the energy security, justice, and governance problem,” *Energ Policy*, 41: 232–240, 2012.
- [5] Ni M., Leung D. Y. C., and Leung M. K. H., “A review on reforming bio-ethanol for hydrogen production,” *Int J Hydrog. Energ*, 32 (15): 3238–3247, 2007.
- [6] 2015 Hyundai Tucson Fuel Cell, <https://www.hyundaiusa.com/tucsonfuelcell/> last visited on July 2014.
- [7] Cipriani G., Di Dio V., Genduso F., La Cascia D., Liga R., Miceli R., and Ricco Galluzzo G., “Perspective on hydrogen energy carrier and its automotive applications,” *Int J Hydrog. Energ*, 39: 8482–8494, 2014.
- [8] Díaz Alvarado F. and Gracia F., “Steam reforming of ethanol for hydrogen production: Thermodynamic analysis including different carbon deposits representation,” *Chem Eng J*, 165 (2): 649–657, 2010.
- [9] Rabenstein G. and Hacker V., “Hydrogen for fuel cells from ethanol by steam-reforming, partial-oxidation and combined auto-thermal reforming: A thermodynamic analysis,” *J Power Sources*, 185 (2): 1293–1304, 2008.
- [10] Vaidya P. D. and Rodrigues A. E., “Insight into steam reforming of ethanol to produce hydrogen for fuel cells,” *Chem Eng J*, 117 (1): 39–49, 2006.
- [11] Torres J. A., Llorca J., Casanovas A., Domínguez M., Salvadó J., and Montané D., “Steam reforming of ethanol at moderate temperature: Multifactorial design analysis of Ni/La₂O₃-Al₂O₃, and Fe- and Mn-promoted Co/ZnO catalysts,” *J Power Sources*, 169, (1): 158–166, 2007.

- [12] Fishtik I., Alexander A., Datta R., and Geana D., “A thermodynamic analysis of hydrogen production by steam reforming of ethanol via response reactions,” *Int J Hydrog. Energ*, 25: 31–45, 2000.
- [13] Diaz Alvarado F. and Gracia F., “Steam reforming of ethanol for hydrogen production: Thermodynamic analysis including different carbon deposits representation,” *Chem Eng J*, 165 (2): 649–657, 2010.
- [14] A Lima da Silva A., Malfatti C. D. F., and Müller I. L., “Thermodynamic analysis of ethanol steam reforming using Gibbs energy minimization method: A detailed study of the conditions of carbon deposition,” *Int J Hydrog. Energ*, 34 (10) :4321–4330, 2009.
- [15] Kayadelen H. K. and Ust Y., “Prediction of equilibrium products and thermodynamic properties in H₂O injected combustion for C_αH_βO_γN_δ type fuels,” *Fuel*, 113: 389–401, 2013.
- [16] Liguras D. K., Kondarides D. I., and Verykios X. E., “Production of hydrogen for fuel cells by steam reforming of ethanol over supported noble metal catalysts,” *Appl Catal B-Environ*, 43 (4): 345–354, 2003.
- [17] Erdöhelyi A., Raskó J., Kecskés T., Tóth M., Dömök M., and Baán K., “Hydrogen formation in ethanol reforming on supported noble metal catalysts,” *Catal Today*, 116 (3): 367–376, 2006.
- [18] Zhang B., Cai W., Li Y., Xu Y., and Shen W., “Hydrogen production by steam reforming of ethanol over an Ir/CeO₂ catalyst: Reaction mechanism and stability of the catalyst,” *Int J Hydrog. Energ*, 33 (16): 4377–4386, 2008.
- [19] Frusteri F., Freni S., Spadaro L., Chiodo V., Bonura G., Donato S., and Cavallaro S., “H₂ production for MC fuel cell by steam reforming of ethanol over MgO supported Pd, Rh, Ni and Co catalysts,” *Catal Comm*, 5 (10): 611–615, 2004.
- [20] Panagiotopoulou P. and Verykios X. E., “Mechanistic aspects of the low temperature steam reforming of ethanol over supported Pt catalysts,” *Int J Hydrog. Energ*, 37 (21): 16333–16345, 2012.
- [21] Gunduz S. and Dogu T., “Sorption-Enhanced Reforming of Ethanol over Ni- and Co-Incorporated MCM-41 Type Catalysts,” *Ind Eng Chem*, 51 (26): 8796–8805, 2012.
- [22] Soykal I. I., Bayram B., Sohn H., Gawade P., Miller J. T., and Ozkan U. S., “Ethanol steam reforming over Co/CeO₂ catalysts: Investigation of the effect of ceria morphology,” *Appl Catal A Gen*, 449: 47–58, 2012.

- [23] Haga F., Nakajima T., Miya H., and Mishima S., “Catalytic properties of supported cobalt catalysts for steam reforming of ethanol,” *Catal Lett*, 48 (3–4): 223–227, 1997.
- [24] Llorca J., de la Piscina P. R., Dalmon J.-A., Sales J., and Homs N., “CO-free hydrogen from steam-reforming of bioethanol over ZnO-supported cobalt catalysts,” *Appl Catal B Env.*, 43 (4): 355–369, 2003.
- [25] Rossetti I., Gallo A., Dal Santo V., Bianchi C. L., Nichele V., Signoretto M., Finocchio E., Ramis G., and Michele A. Di, “Nickel Catalysts Supported Over TiO₂, SiO₂ and ZrO₂ for the Steam Reforming of Glycerol,” *Chem Cat Chem*, 5 (1): 294–306, 2013.
- [26] Li S., Li M., Zhang C., Wang S., Ma X., and Gong J., “Steam reforming of ethanol over Ni/ZrO₂ catalysts: Effect of support on product distribution,” *Int J Hydrog. Energ.*, 37 (3): 2940–2949, 2012.
- [27] Fatsikostas A., “Reaction network of steam reforming of ethanol over Ni-based catalysts,” *J Catal*, 225 (2): 439–452, 2004.
- [28] Alberton A. L., Souza M. M. V. M., and Schmal M., “Carbon formation and its influence on ethanol steam reforming over Ni/Al₂O₃ catalysts,” *Catal Today*, 123 (1–4): 257–264, 2007.
- [29] Vizcaíno A. J., Lindo M., Carrero A., and Calles J. A., “Hydrogen production by steam reforming of ethanol using Ni catalysts based on ternary mixed oxides prepared by coprecipitation,” *Int J Hydrog. Energ.*, 37 (2): 1985–1992, 2012.
- [30] Shi Q., Liu C., and Chen W., “Hydrogen production from steam reforming of ethanol over Ni/MgO-CeO₂ catalyst at low temperature,” *J Rare Earths*, 27 (6): 948–954, 2009.
- [31] Nichele V., Signoretto M., Pinna F., Menegazzo F., Rossetti I., Cruciani G., Cerrato G., and Michele A. Di, “Ni/ZrO₂ catalysts in ethanol steam reforming: Inhibition of coke formation by CaO-doping,” *Appl Catal B-Environ*, 150–151: 12–20, 2014.
- [32] Nichele V., Signoretto M., Menegazzo F., Rossetti I., and Cruciani G., “Hydrogen production by ethanol steam reforming: Effect of the synthesis parameters on the activity of Ni/TiO₂ catalysts,” *Int J Hydrog. Energ.*, 39 (9): 4252–4258, 2014.
- [33] Kumar P., Sun Y., and Idem R. O., “Nickel-Based Ceria, Zirconia, and Ceria–Zirconia Catalytic Systems for Low-Temperature Carbon Dioxide Reforming of Methane,” *Energ Fuel*, 21 (6): 3113–3123, 2007.

- [34] Cerritos C., Ramírez R. F., Alvarado A. F. A., Rosales J. M. M., García V., and Esquivel I. R. G., "Steam Reforming of Ethanol over Ni/Al₂O₃ - La₂O₃ Catalysts Synthesized by Sol - Gel," *Ind Eng Chem*, 50: 2576–2584, 2011.
- [35] Christensen K. O., Chen D., Lødeng R., and Holmen A., "Effect of supports and Ni crystal size on carbon formation and sintering during steam methane reforming," *Appl Catal A-Gen*, 314 (1): 9–22, 2006.
- [36] Trimm D. L., "Coke formation and minimisation during steam reforming reactions," *Catal Today*, 37 (3): 233–238, 1997.
- [37] Rossetti I., Lasso J., Nichele V., Signoretto M., Finocchio E., Ramis G., and Michele A. Di, "Silica and zirconia supported catalysts for the low-temperature ethanol steam reforming," *Appl Catal B Env.*, 150–151: 257–267, 2014.
- [38] Borowiecki T., "Nickel catalysts for steam reforming of hydrocarbons; size of crystallites and resistance to coking," *Appl Catal*, 4: 223–231, 1982.
- [39] Jalowiecki-Duhamel L., Pirez C., Capron M., Dumeignil F., and Payen E., "Hydrogen production from ethanol steam reforming over cerium and nickel based oxyhydrides," *Int J Hydrog. Energ*, 35 (23): 12741–12750, 2010.
- [40] Nichele V., Signoretto M., Menegazzo F., Gallo A., Dal Santo V., Cruciani G., and Cerrato G., "Glycerol steam reforming for hydrogen production: Design of Ni supported catalysts," *Appl Catal B-Environ*, 111–112: 225–232, 2012.
- [41] Rossetti I., Biffi C., Bianchi C. L., Nichele V., Signoretto M., Menegazzo F., Finocchio E., Ramis G., and Michele A. Di, "Ni/SiO₂ and Ni/ZrO₂ catalysts for the steam reforming of ethanol," *Appl Catal B-Environ*, 117–118: 384–396, 2012.
- [42] Zhao D., "Triblock Copolymer Syntheses of Mesoporous Silica with Periodic 50 to 300 Angstrom Pores," *Science* 279: 548–552, 1998.
- [43] Fuxiang L., Feng Y., Yongli L., Ruifeng L., and Kechang X., "Direct synthesis of Zr-SBA-15 mesoporous molecular sieves with high zirconium loading: Characterization and catalytic performance after sulfated," *Micropor Mesopor Mat*, 101 (1–2): 250–255, 2007.
- [44] Sener C., "Novel Bimetallic Mesoporous Catalysts for Hydrogen Production Through Steam Reforming of Ethanol," Ph. D. Thesis Middle East Technical University, 2012.
- [45] Seo J. G., Youn M. H., and Song I. K., "Effect of SiO₂-ZrO₂ supports prepared by a grafting method on hydrogen production by steam reforming of liquefied

- natural gas over Ni/SiO₂-ZrO₂ catalysts,” *J Power Sources*, 168: 251–257, 2007.
- [46] Youn M. H., Seo J. G., Cho K. M., Jung J. C., Kim H., La K. W., Park D. R., Park S., Lee S. H., and Song I. K., “Effect of support on hydrogen production by auto-thermal reforming of ethanol over supported nickel catalysts,” *Korean J Chem Eeng*, 25 (2): 236–238, 2008.
- [47] Matsumura Y. and Nakamori T., “Steam reforming of methane over nickel catalysts at low reaction temperature,” *Appl Catal A Gen*, 258 (1): 107–114, 2004.
- [48] Benito M., Padilla R., Rodríguez L., Sanz J. L., and Daza L., “Zirconia supported catalysts for bioethanol steam reforming: Effect of active phase and zirconia structure,” *J Power Sources*, 169 (1): 167–176, 2007.
- [49] Takahashi R., Sato S., Sodesawa T., Yoshida M., and Tomiyama S., “Addition of zirconia in Ni/SiO₂ catalyst for improvement of steam resistance,” *Appl Catal A-Gen*, 273 (1–2): 211–215, 2004.
- [50] Wan H., Li X., Ji S., Huang B., Wang K., and Li C., “Effect of Ni Loading and Ce_xZr_{1-x}O₂ Promoter on Ni-Based SBA-15 Catalysts for Steam Reforming of Methane,” *J Nat Gas Chem*, 16: 139–147, 2007.
- [51] Nogami M., “Crystal growth of tetragonal ZrO₂ in the glass system ZrO₂-SiO₂ prepared by the sol-gel process from metal alkoxides,” *J Mater Sci*, 21: 3513, 1986.
- [52] Iglesias J., Melero J. A., Bautista L. F., Morales G., Sánchez-Vázquez R., Andreola M. T., and Lizarraga-Fernández A., “Zr-SBA-15 as an efficient acid catalyst for FAME production from crude palm oil,” *Catal Today*, 167 (1): 46–55, 2011.
- [53] Arbag H., Yasyerli S., Yasyerli N., Dogu T., and Dogu G., “Coke Minimization in Dry Reforming of Methane by Ni Based Mesoporous Alumina Catalysts Synthesized Following Different Routes: Effects of W and Mg,” *Top Catal*, 56 (18–20): 1695–1707, 2013.
- [54] García V., Fernández J. J., Ruíz W., Mondragón F., and Moreno A., “Effect of MgO addition on the basicity of Ni/ZrO₂ and on its catalytic activity in carbon dioxide reforming of methane,” *Catal Commun*, 11 (4): 240–246, 2009.
- [55] Damyanova S., Pawelec B., Arishtirova K., Huerta M. V. M., and Fierro J. L. G., “Study of the surface and redox properties of ceria–zirconia oxides,” *Appl Catal A-Gen*, 337: 86–96, 2008.

- [56] Natesakhawat S., Watson R., Wang X., and Ozkan U., “Deactivation characteristics of lanthanide-promoted sol-gel Ni/Al₂O₃ catalysts in propane steam reforming,” *J Catal*, 234: 496–508, 2005.
- [57] Terribile D., Trovarelli A., Llorca J., De Leitenburg C., and Dolcetti G., “The Synthesis and Characterization of Mesoporous High-Surface Area Ceria Prepared Using a Hybrid Organic/Inorganic Route,” *J Catal*, 178 (1): 299–308, 1998.
- [58] Liao M., Wang W., Ran R., and Shao Z., “Development of a Ni–Ce_{0.8}Zr_{0.2}O₂ catalyst for solid oxide fuel cells operating on ethanol through internal reforming,” *J Power Sources*, 196 (15): 6177–6185, 2011.
- [59] Vlaic G., Di Monte R., Fornasiero P., Fonda E., and Ka J., “Redox Property – Local Structure Relationships in the Rh-Loaded CeO₂–ZrO₂ Mixed Oxides,” *J Am Chem Soc*, 182: 378–389, 1999.
- [60] Biswas P. and Kunzru D., “Steam reforming of ethanol for production of hydrogen over Ni/CeO₂–ZrO₂ catalyst: Effect of support and metal loading,” *Int J Hydrog. Energ*, 32 (8): 969–980, 2007.
- [61] Srinivas D., Satyanarayana C. V. V., Potdar H. S., and Ratnasamy P., “Steam reforming of bio-ethanol for the production of hydrogen over ceria-supported Co, Ir and Ni catalysts,” *Appl Catal A-Gen*, 246 (2): 323–334, 2003.
- [62] Takeguchi T., “Hydrogen Spillover from NiO to the Large Surface Area CeO₂–ZrO₂ Solid Solutions and Activity of the NiO/CeO₂–ZrO₂ Catalysts for Partial Oxidation of Methane,” *J Catal*, 202 (1): 14–24, 2001.
- [63] Hu R., Yan C., Zheng X., Liu H., and Zhou Z., “Carbon deposition on Ni/ZrO₂-CeO₂ catalyst during steam reforming of acetic acid,” *Int J Hydrog. Energ*, 38: 6033–6038, 2013.
- [64] Djinović P., Osojnik Črnivec I. G., Erjavec B., and Pintar A., “Influence of active metal loading and oxygen mobility on coke-free dry reforming of Ni–Co bimetallic catalysts,” *Appl Catal B-Environ*, 125: 259–270, 2012.
- [65] Osojnik Črnivec I. G., Djinović P., Erjavec B., and Pintar A., “Effect of synthesis parameters on morphology and activity of bimetallic catalysts in CO₂–CH₄ reforming,” *Chem Eng J*, 207–208: 299–307, 2012.
- [66] Pérez-Hernández R., Gutiérrez-Martínez A., Palacios J., Vega-Hernández M., and Rodríguez-Lugo V., “Hydrogen production by oxidative steam reforming of methanol over Ni/CeO₂–ZrO₂ catalysts,” *Int J Hydrog. Energ*, 36 (11): 6601–6608, 2011.

- [67] Tsoncheva T., Ivanova L., Paneva D., Mitov I., Minchev C., and Fröba M., “Cobalt and iron oxide modified mesoporous zirconia: Preparation, characterization and catalytic behaviour in methanol conversion,” *Micropor Mesopor Mat*, 120 (3): 389–396, 2009.
- [68] Mbaraka I. K., Radu D. R., Lin V. S. Y., and Shanks B. H., “Organosulfonic acid-functionalized mesoporous silicas for the esterification of fatty acid,” *J Am Chem Soc*, 219: 329–336, 2003.
- [69] Wang X. X., Lefebvre F., Patarin J., and Basset J.-M., “Synthesis and characterization of zirconium containing mesoporous silicas I. Hydrothermal synthesis of Zr-MCM-41-type materials,” *Micropor Mesopor Mat*, 42: 269–276, 2001.
- [70] Sing K. S. W., Everett D. H., Haul R., Moscou L., Pierotti R., Rouquerol J., and Siemieniewska T., “Reporting physisorption data for gas/solid systems with special reference to the determination of surface area and porosity,” *Pure Appl Chem*, 54 (11): 2201–2218, 1985.
- [71] Klimova T., Luisa M., Castillo P., Cuevas R., and Ramirez J., “Characterization of Al₂O₃-ZrO₂ mixed oxide catalytic supports prepared by the sol-gel method,” *Micropor Mesopor Mat*, 20: 293-306, 1998.
- [72] Gutiérrez O. and Romero K., “New NiMo catalysts supported on ZrO₂-modified SBA-15 materials for 4, 6-dimethyldibenzothiophene hydrodesulfurization,” *Stud Surf Sci Catal*: 355–362, 2006.
- [73] Zhang Y.-Q., Wang S.-J., Wang J.-W., Lou L.-L., Zhang C., and Liu S., “Synthesis and characterization of Zr-SBA-15 supported tungsten oxide as a new mesoporous solid acid,” *Solid State Sci*, 11 (8): 1412–1418, 2009.
- [74] Trovarelli A., Zamar F., Llorca J., De Leitenburg C., Dolcetti G., and Kiss J. T., “Nanophase Fluorite-Structured CeO₂ – ZrO₂ Catalysts Prepared by High-Energy Mechanical Milling Analysis of Low-Temperature Redox Activity and Oxygen Storage Capacity,” *J Catal*, 169: 490–502, 1997.
- [75] Daturi M., Finocchio E., Binet C., Lavalley J., Fally F., Perrichon V., Vidal H., N. Hickey, and J. Kas, “Reduction of High Surface Area CeO₂ - ZrO₂ Mixed Oxides,” *J Phys Chem B*, vol. 104, pp. 9186–9194, 2000.
- [76] Fan J., Weng D., Wu X., and Ran R., “Modification of CeO₂-ZrO₂ mixed oxides by coprecipitated/impregnated Sr: Effect on the microstructure and oxygen storage capacity,” *J Catal*, 258 (1): 177–186, 2008.

- [77] Fan J., Wu X., Wu X., Liang Q., Ran R., and Weng D., “Thermal ageing of Pt on low-surface-area CeO₂–ZrO₂–La₂O₃ mixed oxides: Effect on the OSC performance,” *Appl Catal B Env.*, 81 (1–2): 38–48, 2008.
- [78] Biesinger M. C., Payne B. P., Lau L. W. M., Gerson A., and Smart R. S. C., “X-ray photoelectron spectroscopic chemical state quantification of mixed nickel metal, oxide and hydroxide systems,” *Surf. Interface Anal.*, 41 (4): 324–332, 2009.
- [79] NIST X-ray Photoelectron Spectroscopy (XPS) Database, Version 3.5, U.S. Secretary of Commerce on behalf of the United States of America, 2012, <http://srdata.nist.gov/xps/Default.aspx>. last visited on August 2014.

APPENDIX A

SAMPLE PARTICLE SIZE CALCULATION

Particle sizes of the crystals were calculated using Scherrer equation (Equation 1). Sample calculation of crystal size determination were presented with the XRD pattern results of Ni@ZrO₂ in which crystal size of both zirconia and nickel were calculated. XRD data of Ni@ZrO₂ is given in Table 13.

Table 13: XRD data of Ni@ZrO₂

2-theta(deg)	d (Å)	Height(cps)	Int. I(cps deg)	FWHM(deg)
17.37(2)	5.102(7)	48(6)	25.4(10)	0.41(2)
24.016(14)	3.702(2)	124(10)	32(3)	0.232(13)
24.35(2)	3.652(3)	118(10)	93(2)	0.71(2)
28.148(7)	3.1676(8)	1015(29)	500(5)	0.381(6)
31.384(9)	2.8480(8)	688(24)	340(4)	0.383(8)
34.062(16)	2.6299(12)	211(13)	153(3)	0.672(14)
35.13(2)	2.5526(16)	120(10)	71(2)	0.55(2)
38.570(16)	2.3323(9)	63(7)	27.1(12)	0.32(3)
40.66(2)	2.2170(11)	122(10)	117(2)	0.77(2)
44.82(3)	2.0203(14)	78(8)	52(4)	0.56(4)
45.47(4)	1.9932(15)	73(8)	34(3)	0.37(5)
49.262(12)	1.8482(4)	255(15)	120(5)	0.28(3)
50.13(2)	1.8182(7)	272(15)	132(35)	0.29(6)
50.48(3)	1.8063(9)	172(12)	142(37)	0.49(9)
54.04(4)	1.6956(10)	110(10)	55(2)	0.41(4)
55.38(3)	1.6577(8)	156(11)	73(10)	0.41(3)
56.05(2)	1.6394(5)	75(8)	41(10)	0.50(14)

The peak with the highest intensity which was observed at 28.148° was used for the calculation of zirconia crystal size.

$$B = \text{FWHM}_{\text{Zr}} \times \frac{3.14}{180} = 0.381 \times \frac{3.14}{180} = 0.00665 \text{ radians}$$

$$t_{\text{particle,Zr}} = \frac{0.89 \times 0.154}{0.00665 \times \cos\left(\frac{28.148}{2}\right)} = 21.3 \text{ nm}$$

The peak at 44.82° was used for the calculation of metallic nickel crystal size.

$$B = \text{FWHM}_{\text{Zr}} \times \frac{3.14}{180} = 0.56 \times \frac{3.14}{180} = 0.0098 \text{ radians}$$

$$t_{\text{particle,Ni}} = \frac{0.89 \times 0.154}{0.0098 \times \cos\left(\frac{44.82}{2}\right)} = 15.2 \text{ nm}$$

APPENDIX B

XRD DATA OF THE CATALYSTS

X-Ray diffraction analysis results used for the calculation of the particle sizes of the crystals are presented in this section. Data of Ni@ZrO₂ catalyst was given in the previous section. Data of other nickel impregnated catalysts can be found in the following tables.

Table 14: XRD data of Ni@Zr-SBA-15

2-theta(deg)	d (A)	Height(cps)	Int. I(cps deg)	FWHM(deg)
23.15(11)	3.840(18)	75(8)	910(9)	9.63(10)
44.44(3)	2.0369(12)	122(10)	80.7(18)	0.37(4)
51.65(3)	1.7683(9)	44(6)	32.7(17)	0.45(6)
76.28(10)	1.2472(14)	15(4)	12.4(16)	0.43(19)

Table 15: XRD data of Ni@Mg-Zr-SBA-15

2-theta(deg)	d (A)	Height(cps)	Int. I(cps deg)	FWHM(deg)
44.38(3)	2.0395(13)	77(8)	57.8(17)	0.40(5)
51.79(9)	1.764(3)	23(4)	32(2)	0.77(13)

Table 16: XRD data of Ni@Zr-MCM-41

2-theta(deg)	d (A)	Height(cps)	Int. I(cps deg)	FWHM(deg)
44.47(3)	2.0355(13)	125(10)	105(2)	0.50(3)
51.91(7)	1.760(2)	41(6)	52(2)	0.67(11)

Table 17: XRD data of Ni@Ce-Zr-SBA-15

2-theta(deg)	d (Å)	Height(cps)	Int. I(cps deg)	FWHM(deg)
44.55(5)	2.032(2)	21(4)	24(2)	0.82(8)

Table 18: XRD data of Ni@CeO₂-ZrO₂ (6:1) calcined and reduced at 400°C

2-theta(deg)	d (Å)	Height(cps)	Int. I(cps deg)	FWHM(deg)
28.72(2)	3.106(2)	170(12)	377(4)	1.926(18)
33.36(4)	2.684(3)	49(6)	120(2)	2.08(5)
48.02(4)	1.8929(14)	88(9)	246(3)	2.25(3)
56.67(6)	1.6230(15)	57(7)	193(3)	3.01(5)
77.71(16)	1.228(2)	18(4)	61(45)	2.7(2)
80.2(2)	1.196(3)	12(3)	41(3)	2.7(4)

Table 19: XRD data of Ni@CeO₂-ZrO₂ (6:1) calcined and reduced at 450°C

2-theta(deg)	d (Å)	Height(cps)	Int. I(cps deg)	FWHM(deg)
28.650(18)	3.1132(19)	243(14)	486(4)	1.655(16)
33.35(3)	2.685(2)	66(7)	141(2)	1.73(4)
48.08(3)	1.8908(13)	105(9)	262(3)	2.06(3)
56.284(18)	1.6331(5)	70(8)	233(3)	2.71(4)
77.74(12)	1.2275(17)	25(5)	99(3)	3.70(9)
79.93(14)	1.1992(17)	7(2)	17(34)	2.1(2)

Table 20: XRD data of Ni@CeO₂-ZrO₂ (6:1) calcined and reduced at 500°C

2-theta(deg)	d (Å)	Height(cps)	Int. I(cps deg)	FWHM(deg)
28.630(16)	3.1153(17)	287(15)	453(3)	1.140(15)
33.16(3)	2.700(2)	77(8)	105(2)	1.21(2)
47.52(3)	1.9119(10)	125(10)	236(2)	1.52(3)
56.63(4)	1.6240(10)	91(9)	214(3)	1.64(5)
76.84(8)	1.2396(11)	24(4)	104(2)	3.82(8)

Table 21: XRD data of Ni@CeO₂-ZrO₂ (6:1) calcined and reduced at 600°C

2-theta(deg)	d (Å)	Height(cps)	Int. I(cps deg)	FWHM(deg)
28.686(12)	3.1094(13)	305(16)	364(3)	0.886(11)
33.20(2)	2.6965(19)	87(8)	99.8(17)	0.93(2)
47.70(2)	1.9051(7)	145(11)	224(2)	1.230(17)
56.92(3)	1.6165(9)	107(9)	137(6)	1.01(3)
57.22(9)	1.609(2)	31(5)	69(6)	1.27(9)
77.33(4)	1.2330(5)	25(5)	98(3)	3.48(11)

Table 22: XRD data of Ni@CeO₂-ZrO₂ (6:1) calcined and reduced at 650°C

2-theta(deg)	d (Å)	Height(cps)	Int. I(cps deg)	FWHM(deg)
28.657(7)	3.1125(8)	685(24)	581(3)	0.626(7)
33.222(14)	2.6945(11)	168(12)	138.7(18)	0.684(11)
47.651(16)	1.9068(6)	281(15)	324(3)	0.849(14)
56.637(19)	1.6238(5)	183(12)	237(3)	1.034(18)
59.46(4)	1.5533(10)	32(5)	39.3(15)	0.99(5)
69.58(5)	1.3500(8)	28(5)	36.7(10)	1.15(4)
77.02(4)	1.2371(6)	54(7)	86(3)	1.38(5)
79.34(6)	1.2066(8)	36(6)	64(2)	1.50(6)

Table 23: XRD data of Ni@CeO₂ calcined and reduced at 450°C

2-theta(deg)	d (Å)	Height(cps)	Int. I(cps deg)	FWHM(deg)
28.493(17)	3.1300(19)	185(12)	293(2)	1.173(16)
32.95(4)	2.716(3)	50(6)	77.3(17)	1.22(4)
47.35(3)	1.9181(10)	99(9)	179(2)	1.43(2)
56.35(3)	1.6314(8)	73(8)	127(3)	1.56(3)
58.94(11)	1.566(3)	13(3)	25(2)	1.77(17)
69.63(7)	1.3492(12)	13(3)	21.5(8)	1.51(6)
76.75(5)	1.2408(6)	28(5)	92.3(19)	1.98(6)
88.51(8)	1.1037(8)	18(4)	27.8(11)	1.44(6)

Table 24: XRD data of Ni@CeO₂-ZrO₂ (4:1) calcined and reduced at 450°C

2-theta(deg)	d (Å)	Height(cps)	Int. I(cps deg)	FWHM(deg)
28.655(18)	3.1127(19)	231(14)	410(4)	1.458(17)
33.39(3)	2.681(3)	63(7)	129(2)	1.61(4)
48.00(3)	1.8938(12)	102(9)	249(3)	2.00(3)
56.48(5)	1.6279(13)	63(7)	208(2)	2.93(4)
69.78(13)	1.347(2)	9(3)	20.2(18)	2.03(15)
77.87(8)	1.2257(11)	24(4)	113.7(19)	4.18(7)

Table 25: XRD data of Ni@CeO₂-ZrO₂ (2:1) calcined and reduced at 450°C

2-theta(deg)	d (Å)	Height(cps)	Int. I(cps deg)	FWHM(deg)
28.86(5)	3.091(5)	207(13)	456(8)	1.62(5)
47.74(5)	1.9036(18)	95(9)	282(4)	2.22(5)
57.21(5)	1.6088(12)	63(7)	233(3)	2.86(5)
70.60(9)	1.3330(15)	8(3)	19.9(14)	2.2(2)
78.64(13)	1.2156(17)	20(4)	92(2)	4.15(11)

Table 26: XRD data of Ni@CeO₂-ZrO₂ (1:1) calcined and reduced at 450°C

2-theta(deg)	d (Å)	Height(cps)	Int. I(cps deg)	FWHM(deg)
29.67(2)	3.009(2)	206(13)	498(4)	2.139(18)
34.43(5)	2.603(4)	47(6)	155(3)	2.91(7)
49.65(4)	1.8345(15)	78(8)	275(3)	3.28(4)
58.76(7)	1.5700(17)	51(7)	233(3)	4.25(6)
81.10(16)	1.185(2)	15(4)	89(2)	5.19(16)
29.67(2)	3.009(2)	206(13)	498(4)	2.139(18)

Table 27: XRD data of used Ni@CeO₂-ZrO₂ (4:1) calcined and reduced and exposed to reaction at 450°C

2-theta(deg)	d (Å)	Height(cps)	Int. I(cps deg)	FWHM(deg)
29.22(2)	3.054(2)	111(10)	270(4)	1.74(3)
33.70(4)	2.657(3)	35(5)	69(3)	1.41(7)
47.89(5)	1.8979(18)	54(7)	124(2)	1.91(4)
56.61(7)	1.6244(18)	34(5)	104(2)	2.68(6)
78.54(17)	1.217(2)	12(3)	53(2)	3.56(17)

Table 28: XRD data of used Ni@CeO₂-ZrO₂ (6:1) calcined and reduced and exposed to reaction at 450°C

2-theta(deg)	d (Å)	Height(cps)	Int. I(cps deg)	FWHM(deg)
28.66(2)	3.112(2)	186(12)	363(3)	1.595(18)
33.36(3)	2.684(3)	53(7)	109(2)	1.62(4)
47.79(3)	1.9017(13)	91(9)	220(3)	1.95(3)
56.48(6)	1.6280(15)	57(7)	174(3)	2.75(5)
78.09(13)	1.2229(17)	23(4)	104(3)	4.06(11)

Table 29: XRD data of used Ni@CeO₂-ZrO₂ (6:1) calcined and reduced and exposed to reaction at 650°C

2-theta(deg)	d (Å)	Height(cps)	Int. I(cps deg)	FWHM(deg)
28.645(11)	3.1137(12)	338(17)	338(3)	0.725(10)
33.20(2)	2.6963(16)	96(9)	92.7(16)	0.775(17)
47.609(19)	1.9085(7)	167(12)	219(2)	0.992(17)
56.47(4)	1.6283(10)	122(10)	202(3)	1.05(4)
76.80(9)	1.2401(12)	24(5)	92(3)	3.47(10)

APPENDIX C

CALIBRATION OF GAS CHROMATOGRAPHY

Product gas stream exiting from the reactor was analyzed in online gas chromatography in each activity test. Calibration of the gas chromatography was conducted with respect to ethanol by taking its calibration factor as 1 using the Equation 5. Retention time and calibration factor of gases involved in the process were presented in Table 30.

$$\frac{X_A}{X_{EtOH}} = \frac{\text{Peak Area of A} \times \text{Calibration factor of A}}{\text{Peak Area of EtOH} \times \text{Calibration factor of EtOH}} \quad (\text{Equation 5})$$

Table 30: Calibration parameters of gases involved in the SRE process

Gas	Retention Time	Calibration Factor (β)
H ₂	0.98-1.0	0.35
CO	1.2-1.3	4.40
CH ₄	1.6-1.8	0.92
CO ₂	3.7-4.0	3.30
C ₂ H ₄	5.1-5.3	1.23
CH ₂ O	8.2-8.4	3.80
C ₂ H ₄ O	10.3-10.8	1.68
C ₂ H ₅ OH	12.2-12.8	1

APPENDIX D

SAMPLE CALCULATION FOR ETHANOL STEAM REFORMING ACTIVITY DATA

Sample calculations of hydrogen yield and product distribution at a reaction temperature of 450°C of Ni@CeO₂/ZrO₂ (6:1) which was calcined and reduced at 450°C are given below.

Mole of A = Area of A × β_A

Table 31: Data of 40th minute obtained with Ni@CeO₂/ZrO₂ at 450°C

Component	Area	β _i	Mole
H ₂	27145.6	0.35	9501.0
CO	209.5	4.40	921.8
CH ₄	463.5	0.92	426.4
CO ₂	681.9	3.30	2250.3
CH ₅ O	161.7	1.0	161.7

Initial mole number of ethanol is calculated by the carbon balance of the outlet stream;

$$n_{C_2H_5O,0} = n_{C_2H_5O} + 0.5 n_{CO} + 0.5 n_{CH_4} + 0.5 n_{CO_2} = 1960 \text{ moles}$$

$$\text{Ethanol Conversion} = X = \frac{n_{C_2H_5O,0} - n_{C_2H_5O}}{n_{C_2H_5O,0}} \times 100 = 91.7 \%$$

$$\text{H}_2 \text{ Yield} = \frac{n_{H_2}}{n_{C_2H_5O,0}} = 4.85$$

$$n_{\text{Total product}} = n_{H_2} + n_{CO} + n_{CH_4} + n_{CO_2} = 13100 \text{ moles}$$

$$\text{H}_2 \text{ \% in product stream} = \frac{n_{\text{H}_2}}{n_{\text{Total}}} \times 100 = 72.5 \%$$

$$\text{H}_2 \text{ formed/EtOH reacted} = \frac{n_{\text{H}_2}}{n_{\text{C}_2\text{H}_5\text{O},0} - n_{\text{C}_2\text{H}_5\text{O}}} = 5.28$$

APPENDIX E

ACTIVITY TEST RESULTS

Product distributions obtained from the activity tests which were not presented in results and discussion section are given here.

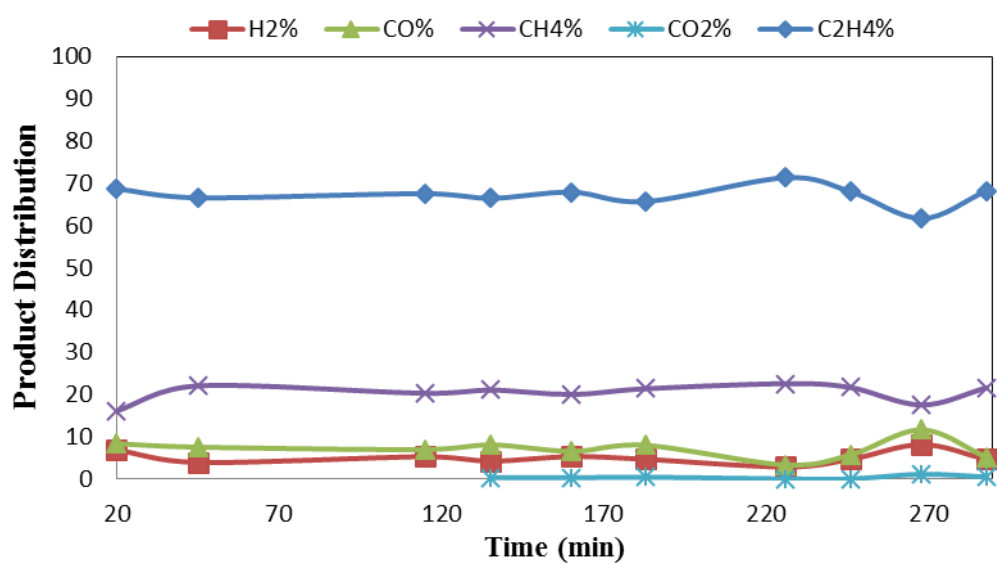


Figure 69: Product distribution of Ni@ZrO₂ catalyst at 550°C.

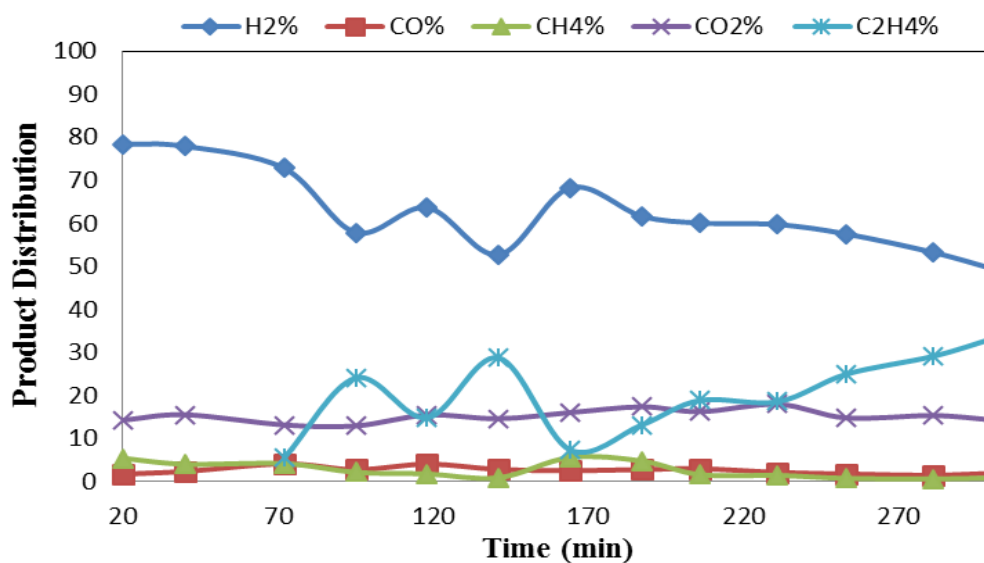


Figure 70: Product distribution of Ni@Ce-Zr-SBA-15 catalyst at 550°C.

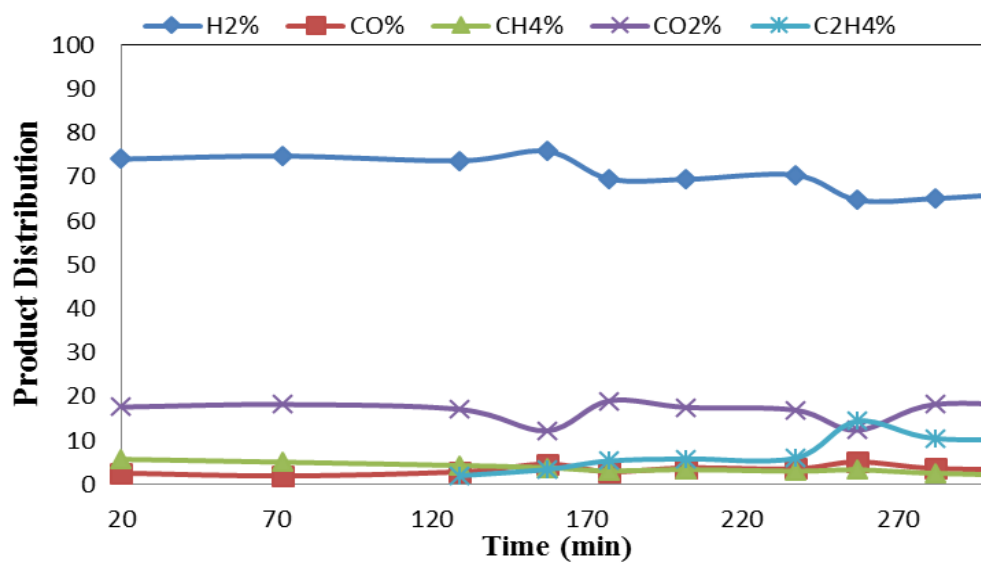


Figure 71: Product distribution of Ni@Mg-Zr-SBA-15 catalyst at 550°C with a H₂O/EtOH of 3.2.

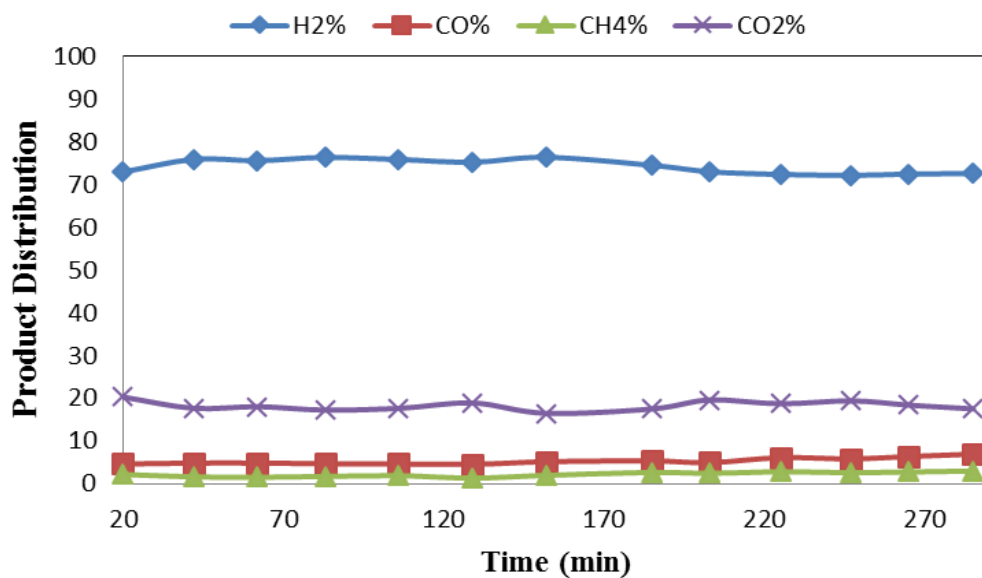


Figure 72: Product distribution of Ni@Mg-Zr-SBA-15 catalyst at 600°C with a H₂O/EtOH of 4.

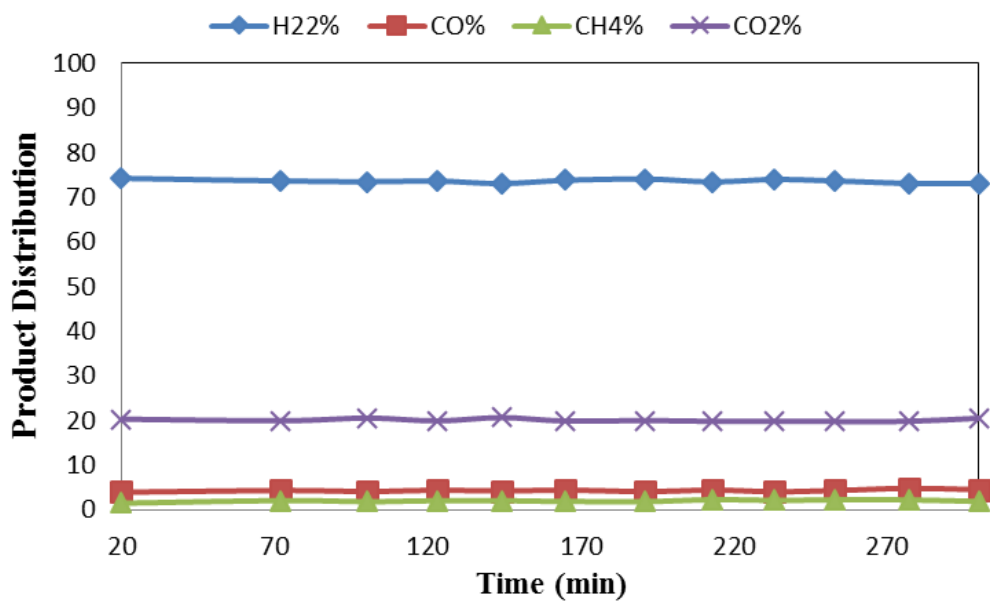


Figure 73: Product distribution of Ni@Mg-Zr-SBA-15 catalyst at 600°C with a H₂O/EtOH of 5.

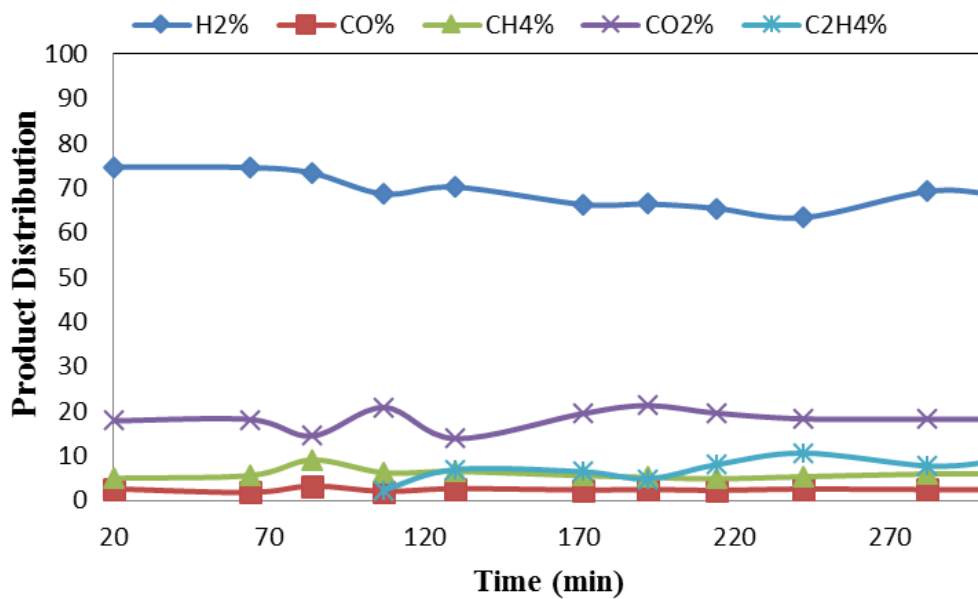


Figure 74: Product distribution of Ni@Zr-MCM-41 catalyst at 550°C.

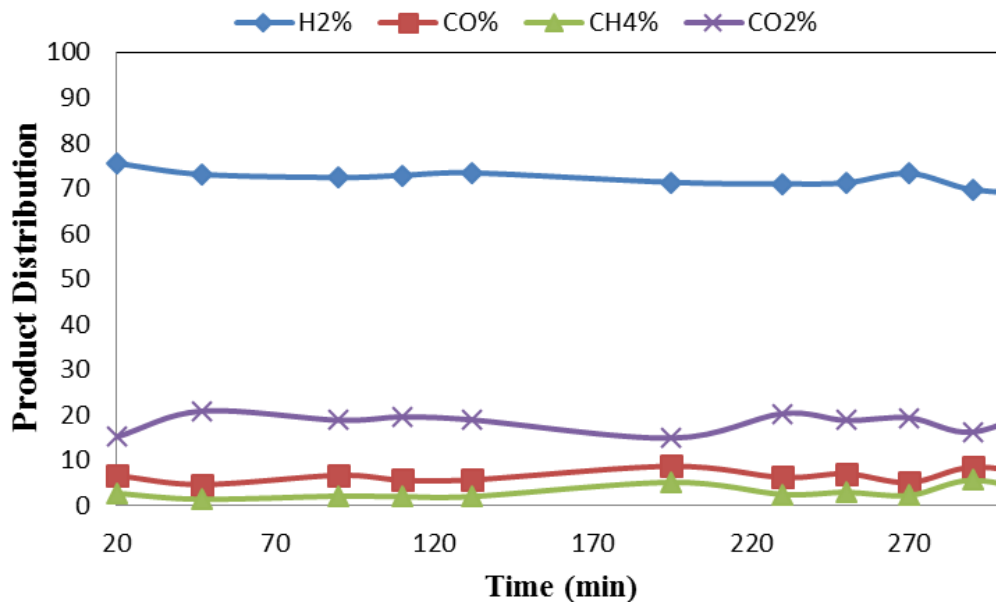


Figure 75: Product distribution of Ni@Zr-SBA-15 catalyst at 600°C with a H₂O/EtOH of 4.

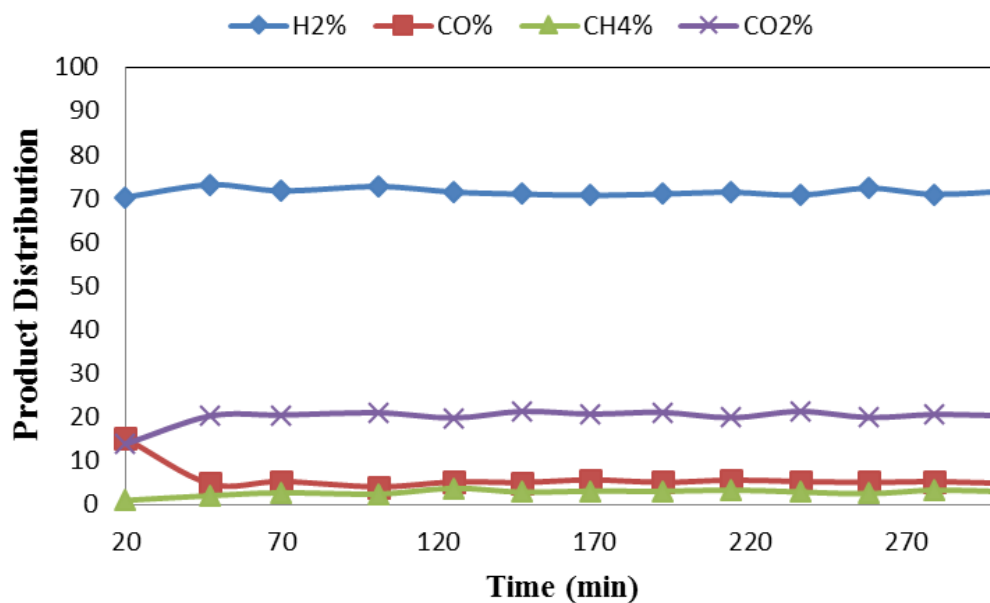


Figure 76: Product distribution of Ni@Zr-SBA-15 catalyst at 600°C with a H₂O/EtOH of 5.

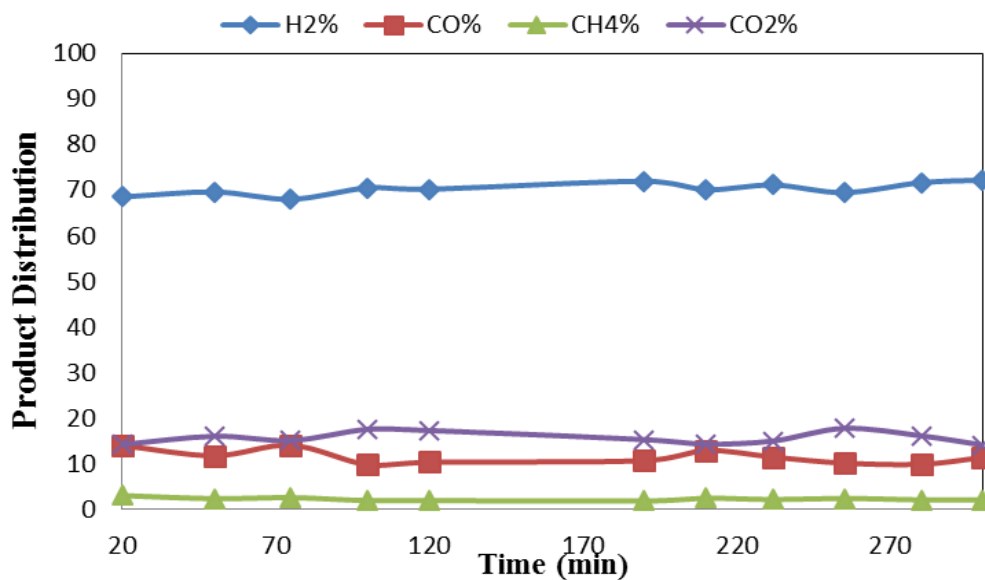


Figure 77: Product distribution at a reaction temperature of 650°C for SRE with Ni@CeO₂-ZrO₂ (6:1) calcined and reduced at 650°C

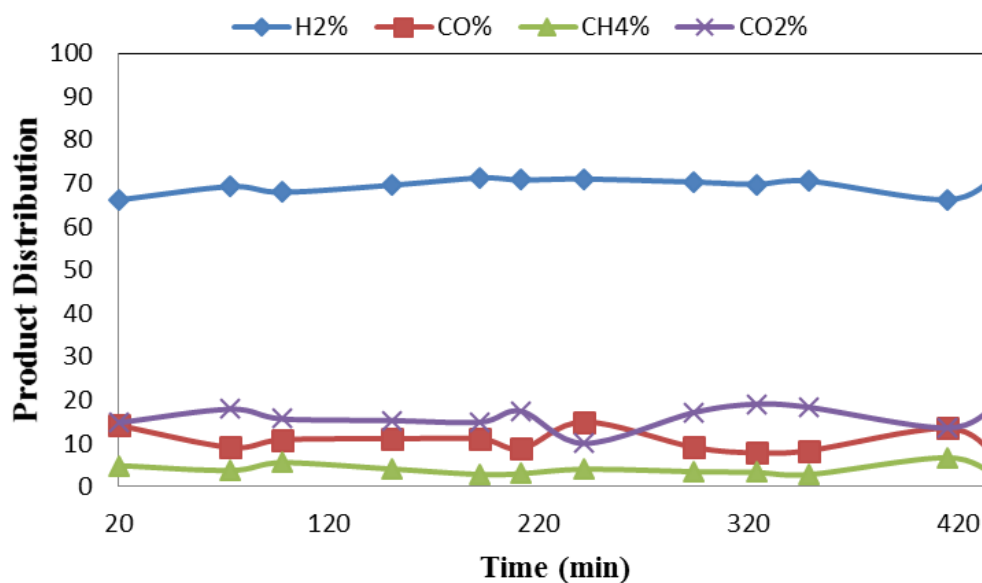


Figure 78: Product distribution at a reaction temperature of 650°C for SRE with Ni@CeO₂-ZrO₂ (6:1) calcined and reduced at 600°C

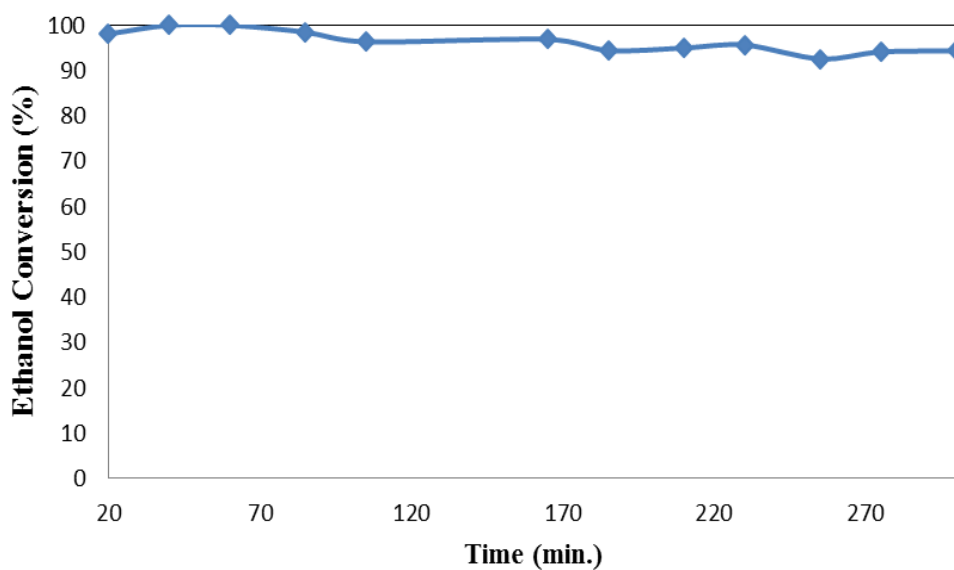


Figure 79: Ethanol conversion at a reaction temperature of 550°C for SRE with Ni@CeO₂-ZrO₂ (6:1) calcined and reduced at 650°C

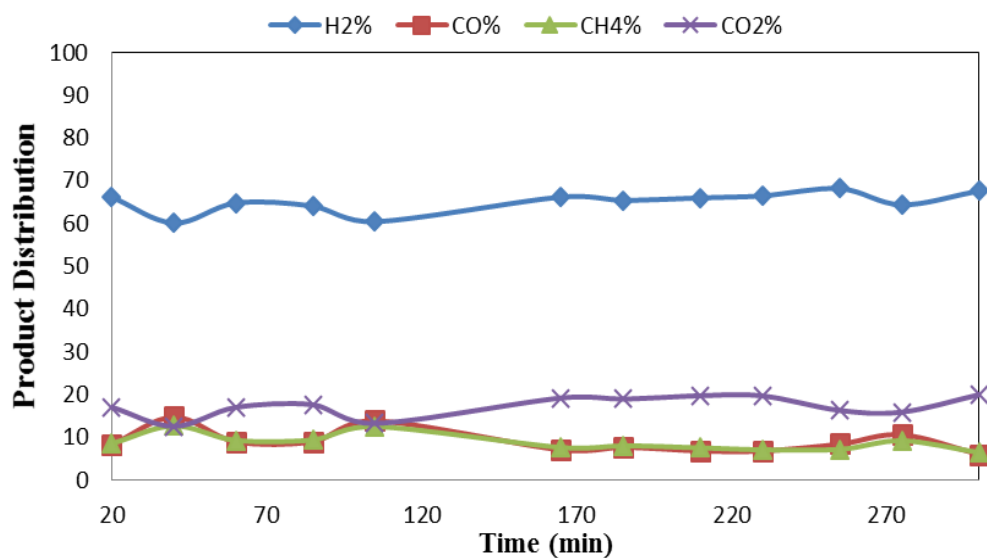


Figure 80: Product distribution at a reaction temperature of 550°C for SRE with Ni@CeO₂-ZrO₂ (6:1) calcined and reduced at 650°C

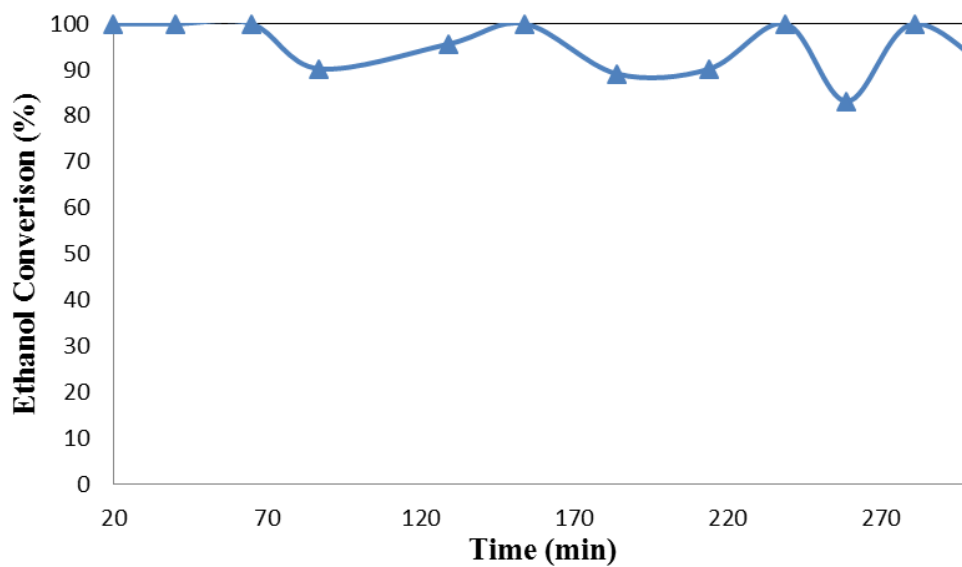


Figure 81: Ethanol conversion at a reaction temperature of 450°C for SRE with Ni@CeO₂-ZrO₂ (6:1) calcined and reduced at 650°C

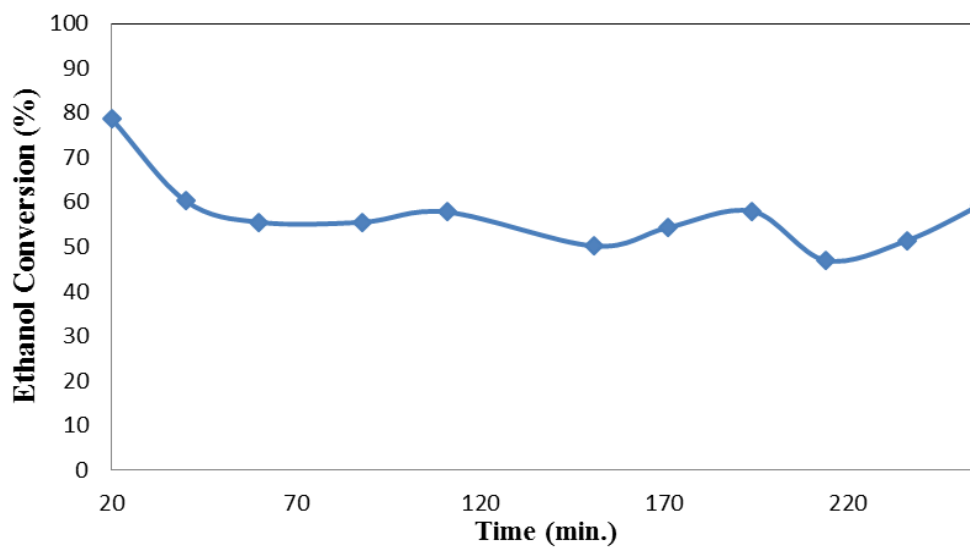


Figure 82: Ethanol conversion at a reaction temperature of 400°C for SRE with Ni@CeO₂-ZrO₂ (6:1) calcined and reduced at 400°C

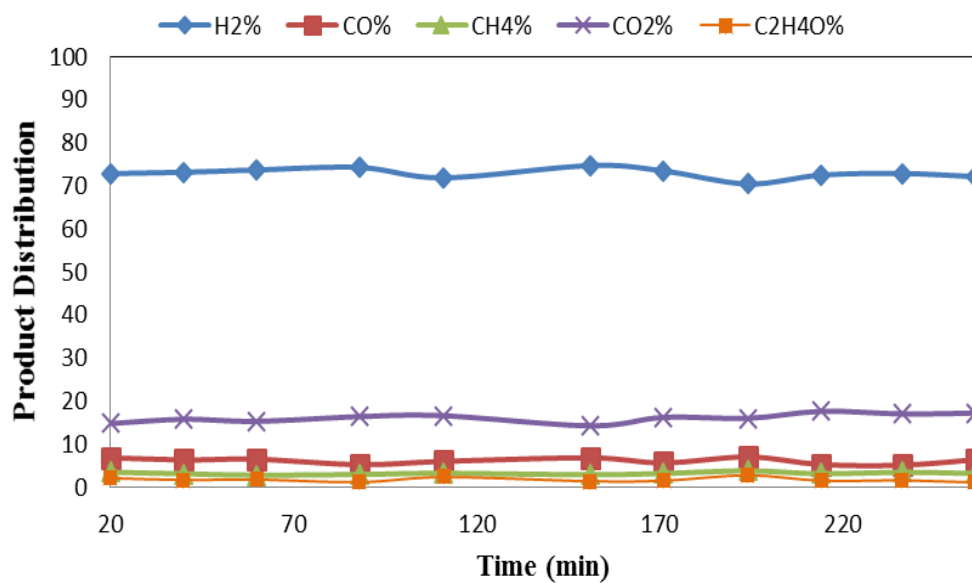


Figure 83: Product distribution at a reaction temperature of 400°C for SRE with Ni@CeO₂-ZrO₂ (6:1) calcined and reduced at 400°C

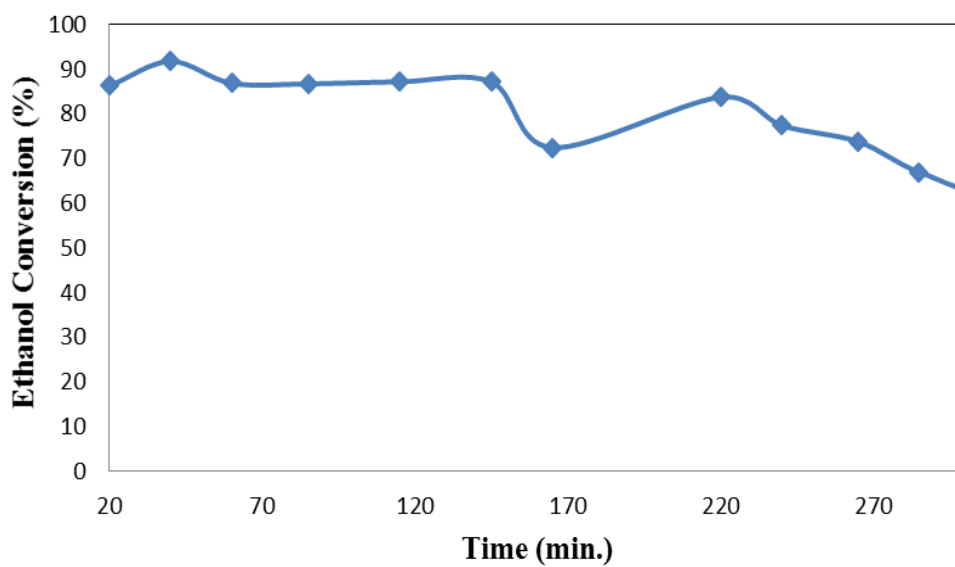


Figure 84: Ethanol conversion at a reaction temperature of 450°C for SRE with Ni@CeO₂-ZrO₂ (6:1) calcined and reduced at 450°C

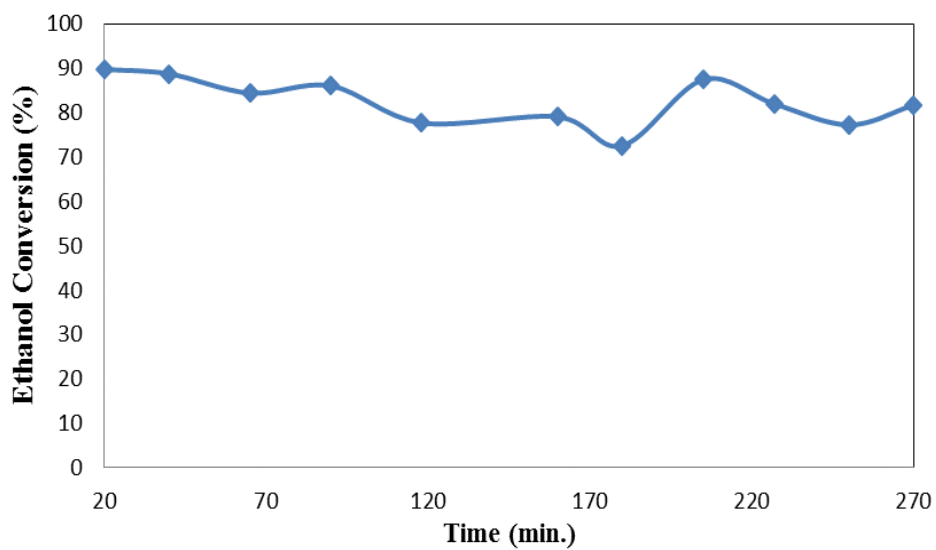


Figure 85: Ethanol conversion at a reaction temperature of 500°C for SRE with Ni@CeO₂-ZrO₂ (6:1) calcined and reduced at 500°C

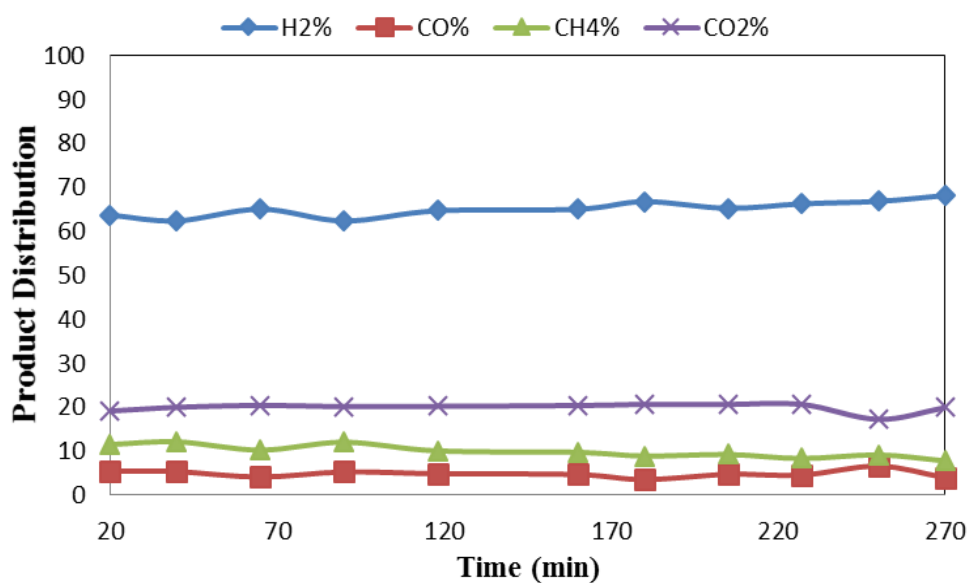


Figure 86: Product distribution at a reaction temperature of 500°C for SRE with Ni@CeO₂-ZrO₂ (6:1) calcined and reduced at 500°C

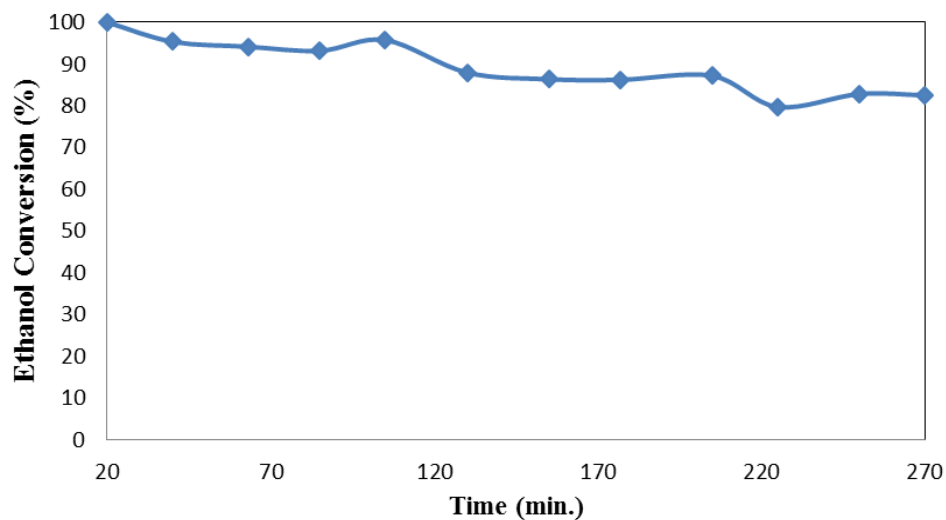


Figure 87: Product distribution at a reaction temperature of 550°C for SRE with Ni@CeO₂-ZrO₂ (6:1) calcined and reduced at 550°C

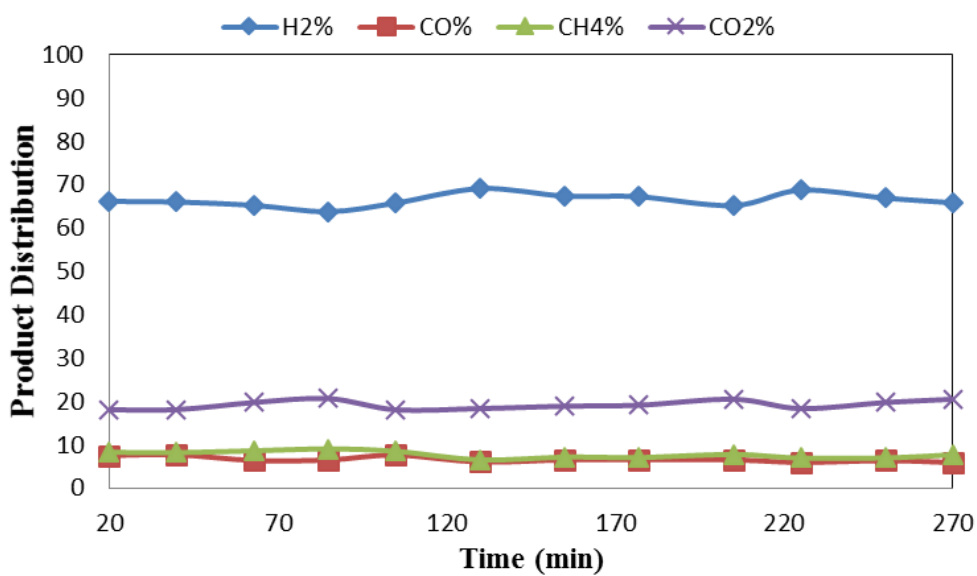


Figure 88: Product distribution at a reaction temperature of 550°C for SRE with Ni@CeO₂-ZrO₂ (6:1) calcined and reduced at 550°C

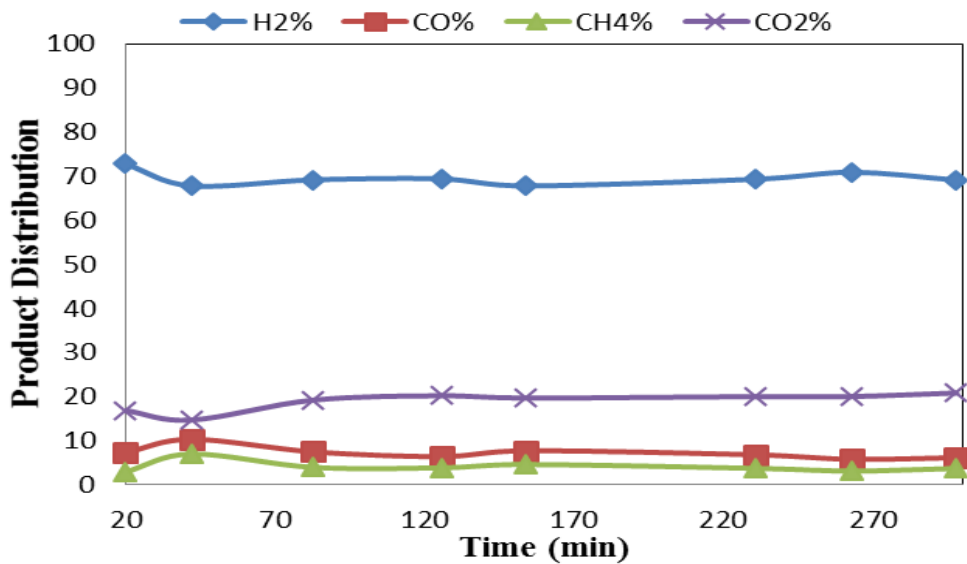


Figure 89: Product distribution at a reaction temperature of 600°C for SRE with Ni@CeO₂-ZrO₂ (6:1) calcined and reduced at 600°C.

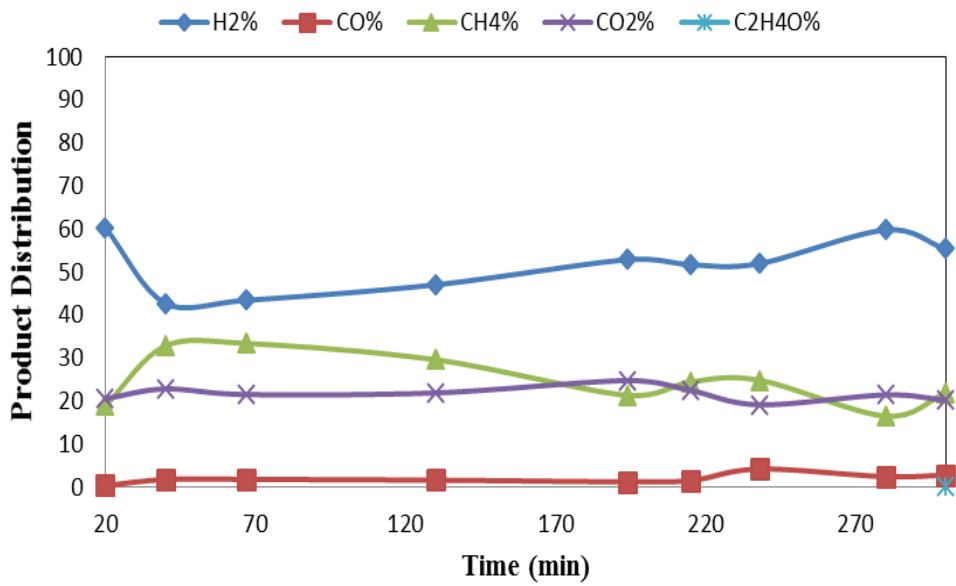


Figure 90: Product distribution at a reaction temperature of 450°C for SRE with Ni@CeO₂ calcined and reduced at 450°C.

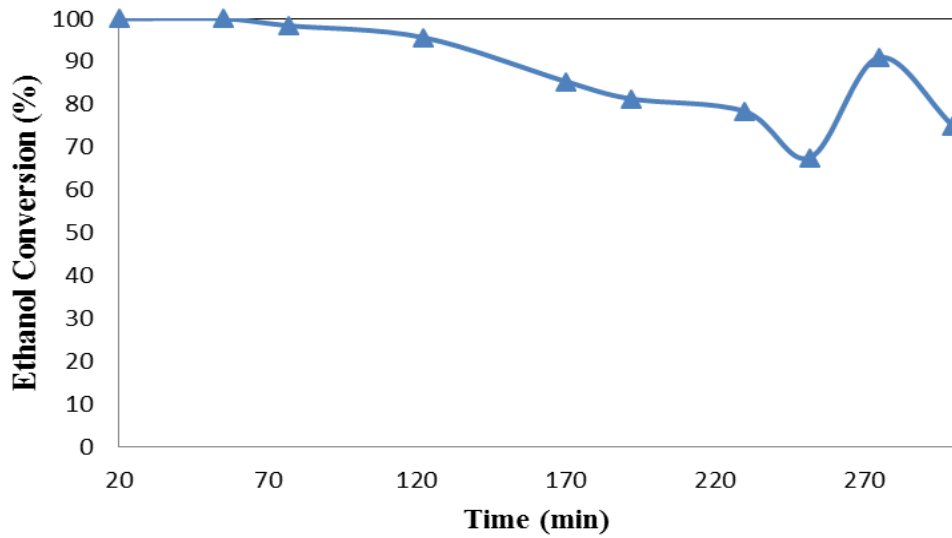


Figure 91: Ethanol conversion at a reaction temperature of 450°C for SRE with Ni@CeO₂-ZrO₂ (1:1) calcined and reduced at 450°C.

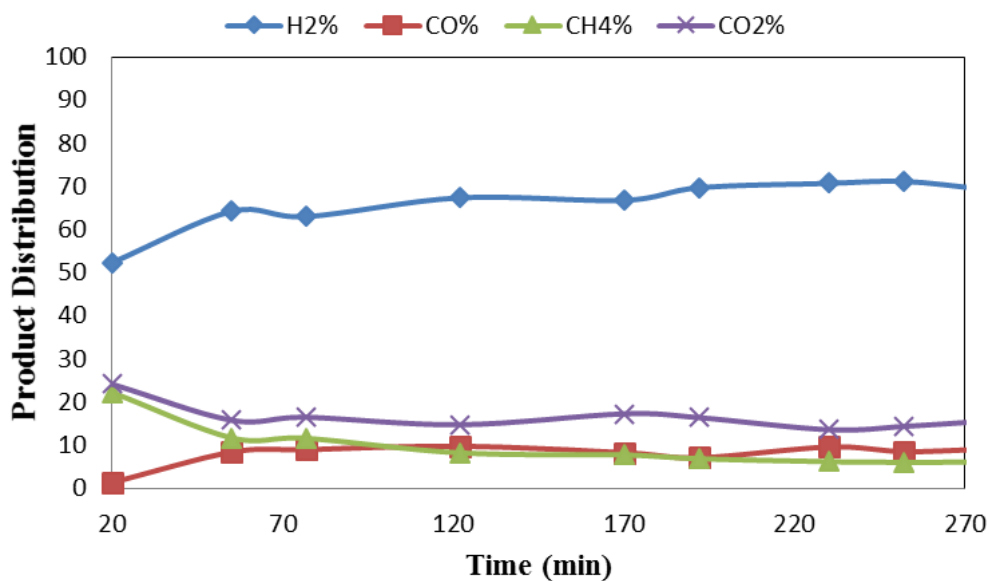


Figure 92: Product distribution at a reaction temperature of 450°C for SRE with Ni@CeO₂-ZrO₂ (1:1) calcined and reduced at 450°C.

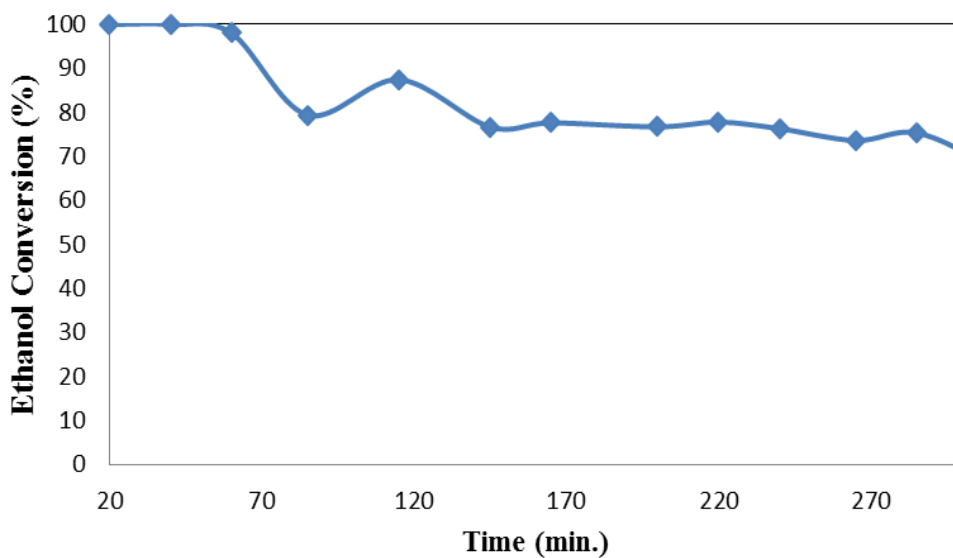


Figure 93: Ethanol conversion at a reaction temperature of 450°C for SRE with Ni@CeO₂-ZrO₂ (2:1) calcined and reduced at 450°C.

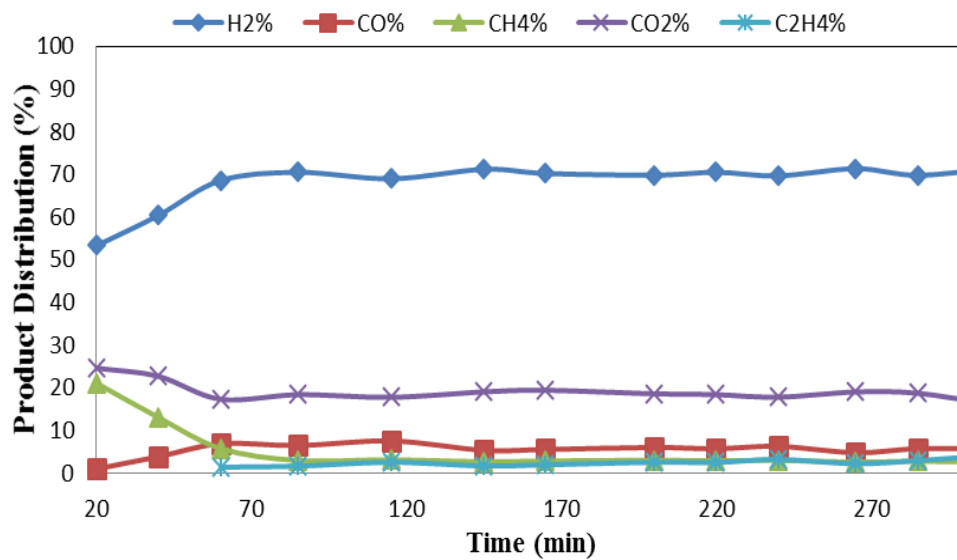


Figure 94: Product distribution at a reaction temperature of 450°C for SRE with Ni@CeO₂-ZrO₂ (2:1) calcined and reduced at 450°C.